# Condensation of water on rust surfaces, and possible implications for hydrate formation in pipelines


Master of Science thesis in process technology

by

Christian Anders Bøe

Department of Physics and Technology

University of Bergen, Norway

June 2011

# Abstract

The threat of climate change has put the spotlight on the increase in carbon emissions and possible methods to attenuate it. As a consequence of this, oil and gas companies have started to consider both how to reduce emissions and use long-term sequestration of produced $CO_2$. Statoil is working on a project which explores the possibilities of storing $CO_2$ in geological formations beneath the sea to mitigate the climate change, as well as to investigate the possibilities for using $CO_2$ gas in Enhanced Oil Recovery (EOR). This project will involve pipeline transport of $CO_2$ gas on the bottom of the North Sea. Because of non-zero water content of this $CO_2$, water can drop out as a liquid within the pipeline. The presence of liquid water and a strong hydrate former like $CO_2$ can lead to hydrate plugging the pipeline under certain conditions. Companies such as Statoil spend large amounts of money on preventing hydrate formation within the pipelines, for example by injecting glycols. Their "best practice" approach commonly uses dew-point temperature curves to determine water dropout conditions.

Recent work by Martin Haynes and Jan Thore Vassdal indicates that there is another driving force for water dropout in pipelines since water can adsorb on rusty pipe surfaces before it condenses within the gas phase. If this threat is valid, ignoring it could ultimately could cost the industry a lot of money.

The purpose of this study was to investigate how condensation of water on rust surfaces can affect kinetic and thermodynamic characteristics of hydrate formation in a pipeline. This was investigated by Molecular Dynamic simulations on a microscopic level. A system containing hematite, hydrate, $CO_2$ and water was built and simulated using different force field models, in order to properly model the molecular interactions in the system. These simulations managed to reproduce a number of the system properties successfully.

The water-wettening nature of hematite was observed early in the simulation, as water adsorbed on the hematite surface in two highly structured layers. If this finding holds true in the case of real carbon dioxide pipe transport, this would indicate that the use of dew point curves to determine water-drop out is an outdated method, as the water would condense on the hematite surface before it condenses within the $CO_2$ phase. Ascertaining the affinity of water would require estimating the chemical potential of water adsorbed on hematite.

The adsorbed water layer prevented the $CO_2$ molecules from approaching the hematite surface making it impossible to observe any correlations between hematite and $CO_2$ in the course of the simulation. This indicates that individual $CO_2$ molecules may not been able to approach a wet hematite surface and adsorb on it.

Another interesting effect of including the hematite crystal was the accelerated diffusion of $CO_2$ into water in the presence of hematite. On the other hand, it also appeared that including the hematite crystal in the aqueous phase also resulted in a lower solubility of $CO_2$.

The hematite crystal exhibited no clear-cut preference for orientation, as the crystal continued to translate and rotate throughout the simulation. Although observations showed that the crystal approached both of the phases in the simulations, no permanent orientation could be identified.

The results obtained for the hydrate crystal were promising. The surrounding water around the partially open hydrate cavities quickly acted to complete the cavity structure. Free $CO_2$ molecules entered the cavities as the simulation progressed and behaved as guest molecules for the rest of the simulation. $CO_2$ molecules approached hydrate from both sides, traversing aqueous layers and assuming positions even inside almost destroyed cavities. This expansion of the hydrate structure indicated a possibility of real-life hydrate growth in a pipeline and showed that the faraway presence of hematite would not substantially hinder hydrate growth.

The behavior of the system through the simulations has proven the suitability of the chosen force field models chosen. The three water models used all yielded the same system behavior, with minor differences and none of them appearing to be superior on a whole-system basis.

# Acknowledgements

I would like to use this opportunity to thank my both my supervisors, starting with Professor Tatyana Kuznetsova. Her aid has been invaluable for both the simulation work done and the writing of the thesis. I also want to thank her for the knowledge she has given me about Linux systems, MD simulation and programming during my Master studies. I want to thank my other supervisor, Professor Bjørn Kvamme, for the help he has provided for the planning and writing of this thesis, as well as for his insightful contributions regarding hydrates and thermodynamic processes during my Master studies.

Additionally, I want to thank Bjørnar Jensen for the many tips he has given me for writing the Master thesis, as well as the aid he has provided with the different tools used to create this thesis. I would also like to thank my fellow master students on room 398, Øyvind Berge Sunnarvik and Annbjørg Tonstad Thomassen. I would specifically like to thank Øyvind for the useful data scripts he has shared with me, while I want to thank both Annbjørg and Øyvind for the valuable feedback they have provided on my paper.

Finally, I would like to thank my family for the aid and support they have provided me with during this thesis. Without their aid and support, the time available to complete this thesis would have been shortened significantly.

_____

Christian Anders Bøe

Bergen, June 2011

# List of abbreviations

BF – Bernal-Fowler (water model)

COM – Center of Mass

DNV – Det Norske Veritas (Risk Management Company)

EOR – Enhanced Oil Recovery

EPM/EPM2 – Elementary Physical Model (2) ($CO_2$ models)

F3C – Flexible Three-Centered (water model)

MC – Monte Carlo

MD – Molecular Dynamics

MD43 – Molecular Dynamics 43 (Program)

RDF – Radial (Pair) Distribution Function

VMD – Visual Molecular Dynamics (Program)

SPC – Simple Point Charge (water model)

SPC/E – Extended Simple Point Charge (water model)

TIP – Transferable Intermolecular Potential (see TIP3P, TIP4P, TIP5P and TIPS2)

TIP3P – 3-Point Transferable Intermolecular Potential (water model)

TIP4P – 4-Point Transferable Intermolecular Potential (water model)

TIP5P – 5-Point Transferable Intermolecular Potential (water model)

TIPS2 – Transferable Intermolecular Potential functionS 2 (water model)

UiO – Universitetet i Oslo (University)

# Contents

# 1 Introduction

There has been an increasing focus on $CO_2$ gas the latest years. The threat of climate change has put the spotlight on the increasing amounts of carbon emissions, and possible methods to reduce these. As a consequence of this, oil and gas companies have started to consider how to reduce emissions from their production. Statoil has started a project exploring the possibilities of storing $CO_2$ in geological formations beneath the sea, as well as examining the possibilities for using the gas for Enhanced Oil Recovery (EOR). Other companies concerned with gas are Gassco and Det Norske Veritas (DNV) (Kårstad 2006). These companies are currently working on securing gas pipeline flow, specifically for the conditions in the North Sea (Gundersen 2005). Earlier pipeline standards were insufficient for safe pipeline transport of large quantities of $CO_2$, and DNV had therefore developed a new standard specifically for this purpose. This project resulted in the development of a new Recommended Practice DNV-RP-J202, which was made available to the public in May 2010 (DNV 2010). Another company which is working with $CO_2$ pipelines is the Research and Development (R&D) company Polytec. The company has amongst other things been working with $CO_2$ in relation to EOR, and has been involved in research concerning $CO_2$ offshore pipelines (Oosterkamp 2008).

From this, it is quite clear that the oil and gas industry is currently interested in transporting $CO_2$ in pipelines at the bottom of the North Sea. One of the problems with this is the risk of hydrate formation within the pipeline. The formation of a solid hydrate crystal within the pipelines can end up blocking the pipe. This is catastrophic for a pipeline that is as inaccessible as those found on the bottom of the North Sea. To shift the conditions leading to hydrate formation, the industry either adds chemicals to the gas flow, or heat the pipe. Both of these methods can prevent the forming of hydrates, but are quite costly. Because of the potentially catastrophic consequences, the industry usually makes sure they inhibit the formation of hydrate by adding extra chemicals/heat. The understanding of when hydrate is formed is therefore vital to the industry (Hellan 2007).

The best way to avoid hydrate formation is to keep the pipeline dry of liquid water. Unfortunately, natural gas contains a certain percentage of vaporized water that can condense as liquid water under the right conditions. The dew point curves, which will be discussed later, show the conditions for which water will condense (Moshfeghian 2011). Companies such as Statoil spend large amounts of money on preventing hydrate formation, for example by the aforementioned use of glycols. The use of glycols adds to the production costs and

reduces the gas production capacity of the pipeline, which again results in further loss of profit. Because of this, the industry cooperates with companies such as Polytec and SINTEF, in order to understand hydrate formation and better prevent it (Lervik and Kulbotten 2011).

There is another possibility for hydrate formation, which has been examined by both Haynes (2009) and Vassdal (2010). Their research indicates that before water condenses within a bulk phase, it adsorbs on the rust surfaces within the pipe. The reason for this is that adsorbed water will have a lower chemical potential, and thus this phase transition is more favorable than the condensation into the bulk phase, according to the first and second law of thermodynamics. This suggests an earlier hydrate structuring that starts from the pipe walls. This knowledge is of vital importance to the industry, as this indicates the use of dew-point curves to determine the possible onset of hydrate formation might underestimate the hydrate formation risk. This work is built upon the work of Haynes and Vassdal, and will use Molecular Dynamic simulation to continue their research. This next step will include $CO_2$ gas in the system, as well as a formed hydrate crystal. The system will also contain a hematite crystal, which represents the rust found on the inside surface of pipelines. The last element of this system is water. Together, these elements should provide valuable insight into the processes occurring in a $CO_2$ pipeline (Haynes 2009), (Vassdal 2010).

# 2 Main objectives

The main purpose of this work was to investigate how condensation of water on rust surfaces can affect the thermodynamics and kinetics of hydrate formation in a pipeline carrying hydrate formers in the form of water and carbon dioxide. In order to do so properly, the properties of hematite and hydrate must be investigated in the presence of water and $CO_2$.

In order to achieve this goal, a number of sub-goals had to be accomplished:

- A system containing hydrate, hematite, $CO_2$ and water must be built and used in MD simulations.
- Suitable force field models adequately reproducing the relevant properties of water, $CO_2$ and hematite must be chosen to ensure accurate modeling of the system's behavior.
- The MD simulation of the system must be long enough to provide reliable system configurations and results.
- The impact of hematite crystal presence on the equilibrium properties and kinetics of interfacial water-$CO_2$ -$CO_2$ hydrate should be investigated. In particular, it would be informative to determine possible preferences of water and $CO_2$ for adsorption on hematite.
- The position of the hematite crystal must be tracked to analyze the motion pattern to determine whether it will move away from its original location and achieve a steady orientation and position with respect to either the hydrate phase or the $CO_2$ phase.
- The interactions between the hydrate crystal and free water and $CO_2$ must be investigated to check whether the access to free water and $CO_2$ molecules is going to result in hydrate growth.

# 3 Scientific methods

The purpose of this study is as mentioned above to investigate how condensation of water on rust surfaces can affect the kinetic and thermodynamic behavior of hydrate formation in a pipeline. It was determined early in the process that these properties should be investigated using computer simulations on a microscopic level. The reason for this is that the properties that were to be investigated cannot be determined experimentally, as phenomena such as adsorption and hydrate growth occur on a microscopic level, which cannot be investigated on a macroscopic scale.

Due to the kinetic properties of the system being of vital importance for the investigation, Molecular Dynamics (MD) was the method of choice for the simulation. As opposed to Monte Carlo and other numerical techniques capable of probing atomistic-scale behavior, MD simulations make it possible to follow the development of a system in true time, both visually and numerically. As the system had numerous time-dependant processes, this method was deemed the best choice.

It was important to have force field models that could adequately reproduce the properties of the molecules in the system. Models for water, $CO_2$ and hematite therefore had to be chosen carefully. This was no easy task, as the models not only had to reproduce the properties of the molecules themselves, but also their behavior when interacting with other molecule types. The models chosen for $CO_2$ and hematite have been used in simulations with water before, and should therefore behave adequately. The choice of a suitable water model was harder, as a great number of water models exist. It was therefore decided to use three different water models to simulate the system. Doing so provides an opportunity to consider how different water models affect the system.

The system included both a hematite and a hydrate crystal. The hydrate crystal was chosen to be the defining cell of the system, as this crystal needed to be large to avoid instabilities in the structure. This meant that the hematite crystal included in the system had to be smaller to fit in. The interactions between these crystals and the free water and $CO_2$ molecules in the system were the focus of this work, and it was also important for us that the crystal would be small enough to move inside the free phases and not affect its own periodic images.

# 4 Description of crystal components

This chapter describes the two crystal structures that are included in this work. These crystal structures are hematite (rust) and hydrate. Their properties will be important and must be discussed, as their interactions with water and $CO_2$ and the possible consequences those interactions can have for water dropout and hydrate formation were central in this work.

## 4.1 Hematite

Iron oxides, commonly known as rust, play an important role in disciplines such as industrial chemistry, soil science and biology. Iron oxides are minerals that are introduced into the environment from the earth's crust, and can be found in soils, rocks, lakes, rivers and in the sea bed. One of the most common iron oxides is hematite ($\alpha$-$Fe_2O_3$). Hematite is formed by the dehydration of goethite ($\alpha$-$Fe_2O_3$), which again is formed by the oxidation of iron hydroxide ($Fe(OH)_2$). One of the most important properties of hydrate, is that it is strongly water-wettening, and therefore water will be attracted to its surface (de Leeuw and Cooper 2007).

Hematite has a hexagonal structure, which means that the oxygen atoms are approximately in a hexagonal close-packing arrangement, with Fe(III) ions located between the O-layers. These iron atoms are octahedrally coordinated to six oxygen atoms. From the chemical formula of hematite it is also possible to see that for every 2 iron atoms in the crystal, there are 3 oxygen atoms. These structural properties are shown below in Figure 4.1, which depicts a hematite crystal from two angles.

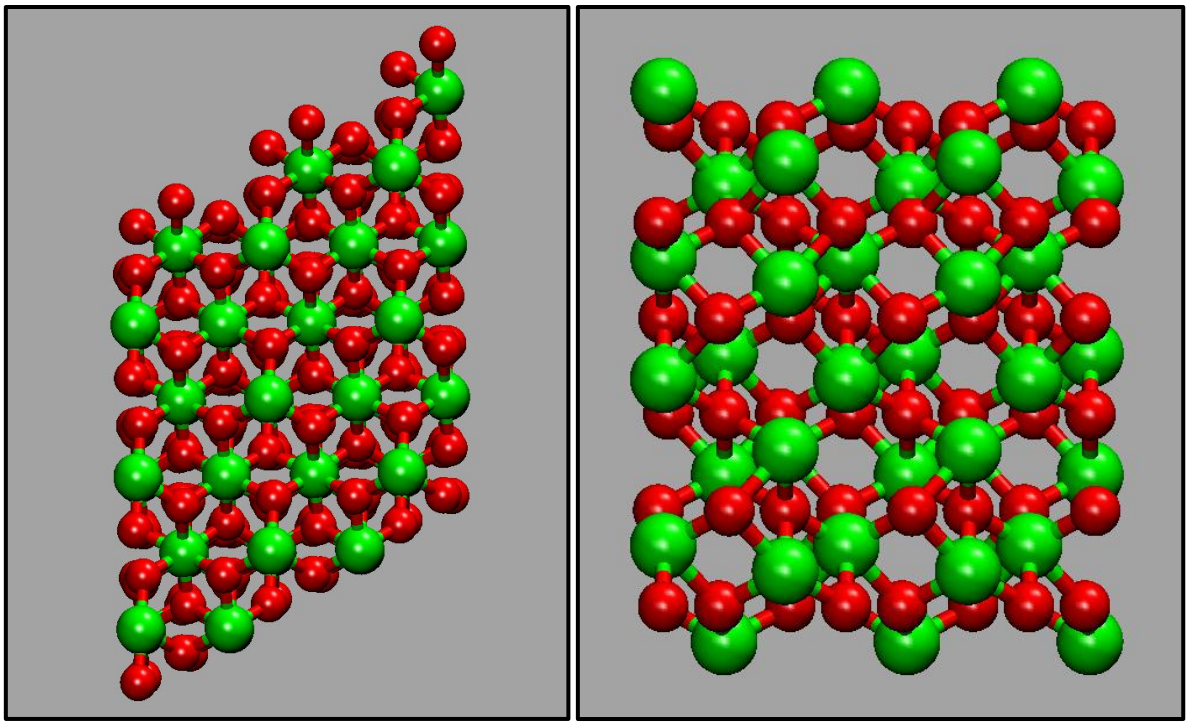

**Figure 4.1 – Hematite crystal. The iron atoms are colored green, while the oxygen atoms are red.**
**On the left: Crystal structure seen from above (Z-direction)**
**On the right: Crystal structure seen from above (Y-direction)**

de Leeuw and Cooper (2007) states that one of the most commonly occurring hematite surfaces is the top surface, which is also known as the $\{0001\}$ surface. When cutting the crystal to an appropriate size, it is possible to terminate this surface with a top layer of either Fe- or O-atoms. The iron-terminated surface is described as the most stable surface, while the oxygen-terminated surface on a stand-alone basis is considered very unstable. When this surface is hydrated however, the oxygen-terminated surface is more stable than the iron-terminated surface (de Leeuw and Cooper 2007). For this work, the iron-terminated surface was chosen (see Figure 4.1, the top and bottom of the picture on the right). The reason for this choice is discussed in section 9.2.4. Further details of the hematite structure will also be discussed in section 8.3.2.

There has been done much research on the simulation behavior of hematite, such as the works of Wasserman et al. (1999), Rustad et al. (1999), Jones et al. (2000), and Lado-Tourino and Tsobnang (2000). This research is especially relevant when considering hematite in the presence of water. This is because water is important for many chemical processes involving iron oxides. The process relevant for this work is the formation of rust, which can be found on

the inside of industrial gas pipes. The theoretical studies conducted by Haynes (2009) and Vassdal (2010) studied the properties of adsorption on hematite surfaces, and made comparisons with water condensation in a bulk water phase. Their research indicates that water droplets will adsorb upon hematite surfaces before they condensate in a bulk phase as calculated from dew point curves. This makes it theoretically possible for hydrate to be formed from adsorbed water on a rusty pipe wall before they condense within in the bulk gas flow itself. The behavior of a hematite crystal in a simulation system containing water will therefore be investigated for relevant model systems through this work (Haynes 2009), (Vassdal 2010), (Rustad et al. 1999; Wasserman et al. 1999; Jones et al. 2000; Lado-Tourino and Tsobnang 2000).

## 4.2 Hydrate

Gas hydrates (also known as clathrate hydrates) are ice-like crystalline molecular structures formed from a mixture of water molecules and suitably sized "guest" gas molecules. The water molecules, bound together by hydrogen bonding, form lattice structures with several cavities. The guest molecules can occupy these cavities, and when a minimum number of cavities are filled, the hydrate becomes a solid, stable gas hydrate. This may possibly occur at temperatures above the freezing point of water at 0˚C (Tohidi 2011). Hydrate formation usually occurs at low temperatures and high pressures, which causes unwanted hydrate plugs in oil and gas pipelines at the bottom of the sea (Hellan 2007).

### 4.2.1 Hydrate structures

Hydrates are formed by water molecules which are structured to form cages around guest molecules. A hydrate cavity does not necessarily need to contain a guest molecule, but if it does, it contains only a single guest per cavity. There exception to this rule is "mixed" hydrates, where two different types of guest molecules can share a hydrate cavity. The water molecules in the hydrate are kept together by hydrogen bonds, while the guest molecules are kept in place by van der Waal forces (Sloan 1990). There are three types of well known hydrate structures. These are called structure I, structure II and structure H. Each of these structure types are composed of different types of hydrate cavities, as illustrated in Figure 4.2.

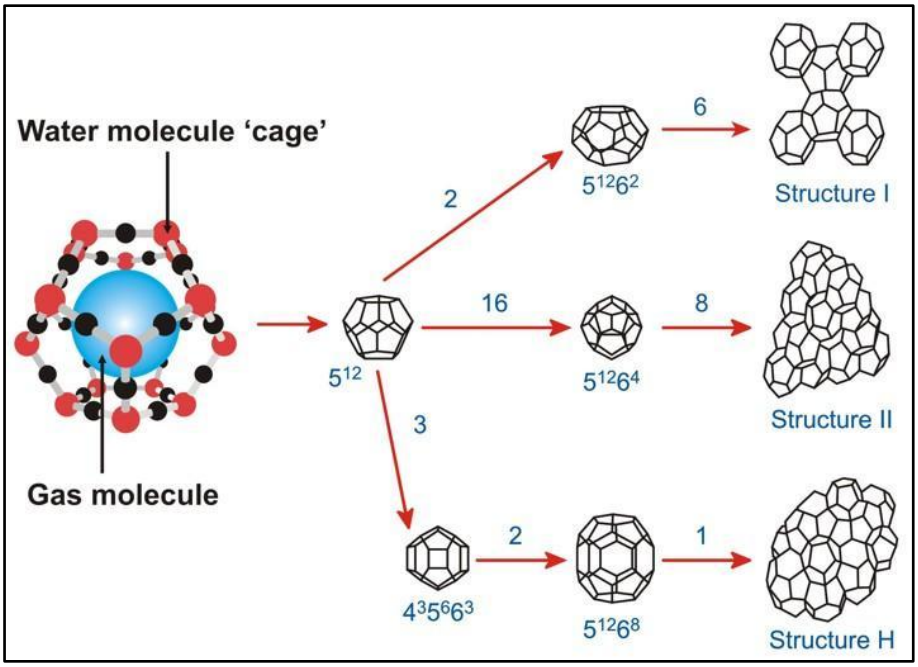


**Figure 4.2 – Hydrate cavity and structure types, taken from (Tohidi 2011)**

**(Figure slightly modified by Christian Bøe)**

The figure shows five different hydrate cavity types. These are the $5^{12}$, $5^{12}6^2$, $5^{12}6^4$, $4^35^46^3$ and $5^{12}6^8$ cavities. The cavity names come from how they are built. For example, the pentagonal dodecahedra ($5^{12}$) cavity is composed by 12 pentagons formed by the water molecules, while the tetradecanhedra ($5^{12}6^2$) is composed by 12 pentagons and 2 hexagons. Figure 4.2 demonstrates how the different cavity types are combined to form the different hydrate types. Structure I is for example formed by two $5^{12}$ and six $5^{12}6^2$ cavities. The hydrate structures are formed with different types of guest molecules. Structure I often have small guest such as methane, ethane and $CO_2$. Structure II has guest molecules such as propane and iso-butane, while structure H has a combination of different guest molecules. The combined guests in structure H can for example be methane and neohexane, or methane and cycloheptane (Tohidi 2011).

This work uses a structure I type hydrate crystal. The diameter of a structure I lattice has originally been defined as 12 Å (Sloan 1990). The work of Shpakov et al. (1998) show that this parameter is somewhat dependant on temperature (Shpakov et al. 1998). Kvamme et al. (2009) used a diameter of 12.03 Å for the hydrate cavities in structure I, and was able to successfully model the conversion of methane hydrate into mixed $CO_2$/methane hydrate. Because such lattice behavior is highly relevant for the simulations conducted this work, the diameter of 12.03 Å will be used (Kvamme et al. 2009).

# 5 Thermodynamics and chemical processes

The previous chapter discussed two crystal structures that are important for this work. This chapter will describe some of the relevant thermodynamics and chemical processes related to these structures.

## 5.1 Condensation and the dew-point temperature

Condensation is an important thermodynamic phenomenon. Condensation of water occurs when moisture in a gas is released as liquid water as the temperature is lowered or the pressure is increased on an initially uniform gas. Since a gas can contain more vaporized water when it is hot, excess water will condense from the gas as liquid water due to the reduced temperature. This is something the oil and gas industry is very interested in, as the industry wants to prevent hydrate formation in a pipeline. More specifically, the industry wishes to understand when liquid water condenses from a gas flow, since hydrate will be formed from the condensed water. To pinpoint this phase transition, they use dew-point temperature curves. The dew point temperature is defined by Çengel and Boles (2007) as the temperature at which condensation begins when the air is cooled at a constant pressure. In other words, this is the temperature at which a gas is fully saturated with water at a given pressure. By studying dew point curves, it is possible to observe how changes in temperature or pressure can lead to condensation of water from a gas phase (Çengel and Boles 2007). There are several diagrams that can be used for dew point calculations. For example, it is possible to use a humidity chart to determine water drop out from the dew point. A humidity chart from McCabe et al. (2005) is shown in Figure 5.1 below. The details for using a humidity chart are outlined in McCabe.

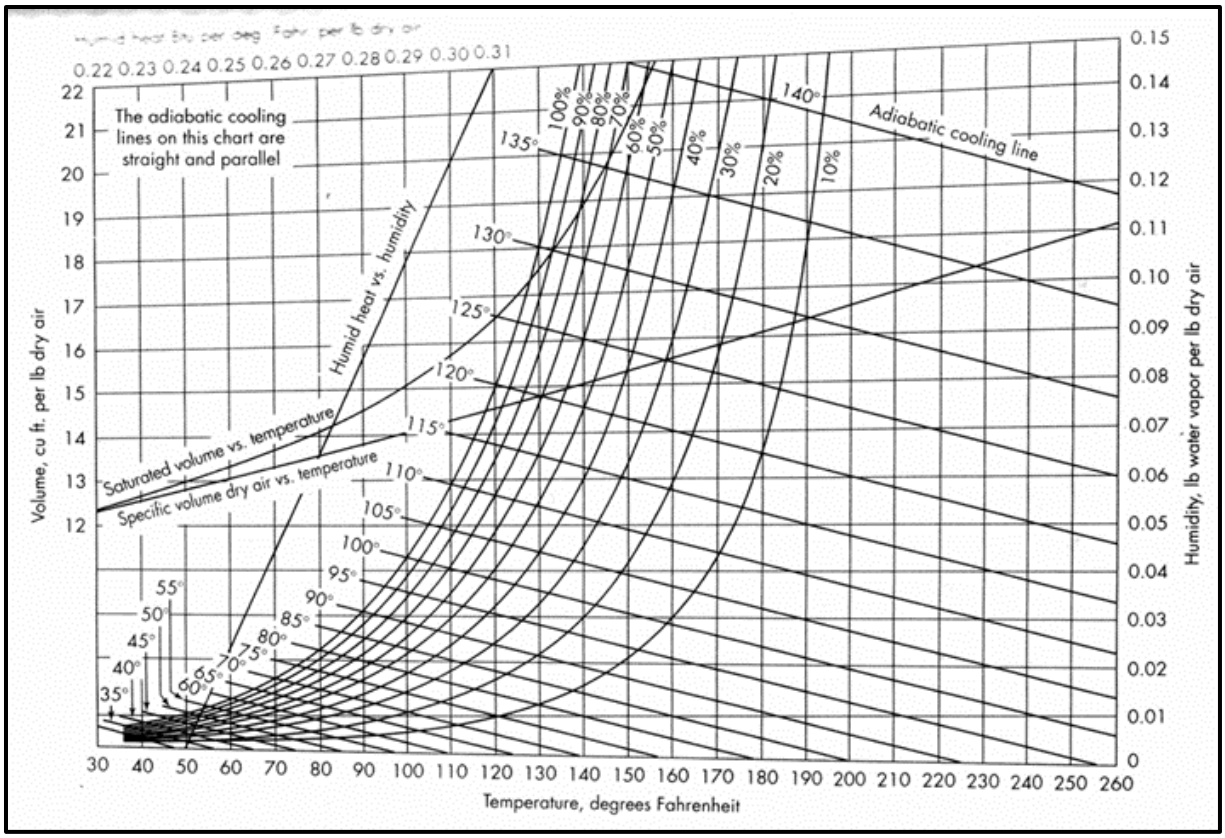


**Figure 5.1 – Humidity chart for air-water at 1 atm, taken from (McCabe et al. 2005)**

Although the "best practice" evaluation techniques might somewhat differ from company to company, the typical approach is to check the dew-point pressure for a given temperature at a point in the pipeline. If the local pressure is higher than this estimated dew-point pressure then water will drop out. This estimate can be done since water is normally the heaviest component in terms of *k*-value, unless some heavy alcohols or other chemicals are present. The *k*-value is defined as the ratio of mole fractions in the vapor and liquid phases at equilibrium. This can be written $k_i = y_{ie}/x_{ie}$, where $y_{ie}$ is the vapor fraction and $x_{ie}$ is the liquid fraction at equilibrium (McCabe et al. 2005). Water will therefore dominate the first droplet condensed, as long as the aforementioned alcohols or chemicals are not present. Similar calculations can also be done with glycols or other components present, but this is not relevant for the work done in this thesis. If water drops out, the next step is to run a flash-calculation (solution of mass balances and chemical equilibrium) at local pressure and temperature conditions to estimate how much water that drops out. This is then used as basis for a subsequent evaluation of strategies to prevent hydrate blocking problems.

## 5.2 Adsorption

A boundary between two phases is known as a surface or an interface. Surfaces show unique properties that are different from those of the phases themselves. One of these properties is called adsorption. Adsorption occurs because the surface of a solid often has an affinity for certain molecules that come into contact with it. As a result of this, these molecules become attached to the surface, or "adsorbed" on the surface (Laider et al. 2003).

There are two main types of adsorption. The first type is called physical adsorption, or physisorption. In this case, the surface forces are of a physical nature and the adsorption is therefore relatively weak. The electrostatic forces involved in this adsorption are known as either Van der Waal forces or Coulomb forces. These forces require no activation energy, and physisorption therefore occurs more rapidly than the next type of adsorption, chemisorption. In chemisorption the adsorbed molecules are held to the surface by covalent forces that can be compared to those occurring between atoms in molecules. Chemisorption needs a certain activation energy to occur, and is therefore a slower process than physisorption. In the case of water adsorbing on hematite, the forces are physical interactions between atoms in the hematite and water atoms and this is therefore a physisorption case.

An important point regarding adsorption is that no surface is entirely smooth. As a result of this, molecules are more easily adsorbed on some surfaces than others. This is interesting to consider when looking at mineral surfaces and their affinity for certain molecules, such as hematite surfaces and their affinity for water (Laider et al. 2003).

Adsorption is discussed in this work because of the work done by Haynes (2009) and Vassdal (2010). Their research indicates that it was more favorable for water vapor to adsorb on pipe surfaces, when compared to condensing within the gas phase. This was concluded because they compared a system containing a hematite crystal with layers of adsorbed water molecules on it, to a system containing water molecules only. The result was that the system with adsorbed water had a lower potential energy. If this is true, this would indicate that hydrate formation can start from adsorbed water on the pipe walls before water droplets are formed within the gas phase. Therefore, information regarding the adsorption properties in a gas pipeline is of great value to the industry, and will therefore be investigated further in this work (Haynes 2009), (Vassdal 2010).

## 5.3 Equilibrium and non-equilibrium processes

The formation of hydrate requires access to both water and guest molecules. Because of this, there exists a driving force for pulling these molecules into the hydrate phase (when hydrate formation is favorable). This process is a mass transfer of water and guest molecules from their bulk phases to the hydrate phases. It is therefore important to consider the limitations of this process (McCabe et al. 2005). At thermodynamic equilibrium, the transport of mass of each component across the interface is equal in both directions and the efficient range of this equal rate of back and forth transport is limited across the interface (Astarita 1989). Normally the range is 1 - 2 nm, but this corresponds to the thickness of the interface. The driving force of such a process depends on how much it deviates from its equilibrium condition. To evaluate the driving force, it is possible to use Gibbs phase rule from McCabe et al. (2005), shown as equation (5.1) below:

$$F = \mathcal{C} - P + 2 \tag{5.1}$$

In this equation, $\mathcal{C}$ is the number of components and $P$ is the number of phases, both for a given system. $F$ is the number of independent intensive variables (such as temperature, pressure and concentrations) that must be fixed to define the equilibrium state of the system. If fewer than $F$ variables are fixed, an infinite number of states fit the assumptions; if too many are chosen, the system will be overspecified (McCabe et al. 2005).

By using Gibbs phase rule, it is possible to determine the equilibrium state of a system, or in other words, the state where all driving forces are approximately zero. Unfortunately, not all systems are able to reach an equilibrium state. As a matter of fact, most hydrate systems do not reach an equilibrium state, either because the equilibrium state cannot be defined by the phase rule, or because of the limitations in the thermodynamic properties, such as a positive Gibbs free energy. The Gibbs free energy is another measurement of driving force, where a more negative Gibbs free energy implicates a stronger driving force, while a non-negative free energy implicates no driving force. This also means that the process most likely to occur is the process which results in the most negative free energy difference. The negative value comes from a negative chemical potential value (Kvamme 2011). The chemical potential is discussed in section 6.9 .

The system used in this work has too many phases present in the system to reach equilibrium, in accordance with Gibbs phase rule (eq. (5.1)). This is logical, as the many kinetic interactions between the different phases make an equilibrium condition for the whole system hard to achieve. The goal in this work with is therefore to simulate the system and evaluate the driving forces for phase transitions.

## 5.4 The thermodynamics of hydrate formation

There are three stages of hydrate formation. They are called nucleation, growth and induction. Only the two first are physically well defined (Natarajan et al. 1994), while induction time is the time for onset of massive growth. Induction time is thus related to the resolution of the method used to monitor the induction time (Kvamme 2011).

The nucleation phase is the formation of the first stable hydrate nuclei. Hydrate nuclei are generated from the supersaturated aqueous solution until they reach a critical size and become stable enough for further growth, which is the next stage (Natarajan et al. 1994).

Growth is the next step of the process. Growth is a process where the hydrate cluster grows slowly as solid hydrate crystals. Until a critical cluster size is reached, the crystal has a higher chance of being dissolved by the surroundings than it has for growing. When it reaches the critical cluster size, the chances for growing and dissolving are the same. The growth that occurs beyond this point is the third and final stage of the hydrate formation (Natarajan et al. 1994).

The final stage of the hydrate formation is called induction time. Induction is the time it takes for hydrate to reach the onset of massive growth. At a certain point, the hydrate crystal becomes so large that the forces from the surroundings become small compared to the favorable energy gained. The growth speed will therefore be greatly increased at this stage (Kvamme 2011).

# 6 Introduction to the basics of numeric modeling

This chapter will discuss the basics of statistical mechanics and computer simulations, as well as tools and techniques involved in obtaining simulation results.

## 6.1 Statistical Mechanics

Statistical mechanics is a type of mechanics that treats the detailed state of a system as unknown, and therefore subject to statistical uncertainties. Statistical mechanics describes the distribution of states in an equilibrium system at a given temperature, and can be used to obtain the thermodynamic properties of the system, using the microscopic properties of the system. This is done based on the probability of a certain state to occur, and can be calculated either by describing the distribution of probabilities of the quantum states, or by considering the probability density function of the system in phase space. The details regarding the probability density will be discussed soon, but in order to do this, it becomes necessary to consider the microscopic and macroscopic properties more thoroughly (Drexler 1992).

Computer simulation generates information at the microscopic level, such as atomic and molecular positions, velocities etc. Statistical mechanics provides a theoretical framework for conversion of microscopically sampled information into macroscopic properties, such as pressure, internal energies, etc. The thermodynamic state of a macroscopic system is usually defined by a small set of parameters, such as the number of particles $N$, the pressure $P$, and the temperature $T$. Other thermodynamic properties that define the system, such as density $\rho$, chemical potential $\mu$, and heat capacity $C_v$ can be derived with the knowledge of the equations of state (EOS) and their relations to thermodynamics. These properties as well as others are important for describing the system, but are all dictated by a few core variables, such as the aforementioned $NPT$, instead of the many atomic positions and momenta that define the instantaneous mechanical state. The main importance with the macroscopic properties is that they are measurable experimentally, while the microscopic properties are not. In order to be able to compare results from computer simulations with real-world experiments, the microscopic data must be converted to macroscopic properties, hence the need for statistical mechanics (Allen and Tildesley 1987).

The microscopic positions and momenta are considered as coordinates in a multidimensional space named phase space. For a system of $N$ atoms, the phase space will have $6N$ dimensions. The microscopic state of a system can be described using the positions and momenta of the atoms and molecules in the system. The Hamiltonian of a system of $N$ molecules can be written as a sum of the kinetic and potential energy functions of the set of coordinates $\mathbf{q_i}$ and momenta $\mathbf{p_i}$ of each molecule $i$. See equation (6.1) from Allen and Tildesley (1987) below.

$$\mathcal{H}(\boldsymbol{q},\boldsymbol{p}) = \mathcal{K}(\boldsymbol{p}) + \mathcal{U}(\boldsymbol{q}) \qquad \textbf{(6.1)}$$

By setting a particular point $\boldsymbol{\Gamma}$ in this space it is possible to determine the instantaneous value of some property $A$ (for example the potential energy) as a function $A$ ($\boldsymbol{\Gamma}$). The system evolves in time, and therefore both $\boldsymbol{\Gamma}$ and $A$ ($\boldsymbol{\Gamma}$) will change. From this it is reasonable to think that the macroscopic property $A_{\text{obs}}$ is really the time average of $A$ ($\boldsymbol{\Gamma}$) taken over a long time interval. This is shown mathematically by equation (6.2) found in Allen and Tildesley (1987):

$$A_{obs} = \langle A \rangle_{time} = \langle A(\boldsymbol{\Gamma}(t)) \rangle_{time} = \lim_{t_{obs}\to\infty} \frac{1}{t_{obs}} \int_0^{t_{obs}} A(\boldsymbol{\Gamma}(t))\mathrm{d}t \qquad \textbf{(6.2)}$$

It is impossible to obtain the results of this equation over an infinite amount of time. Instead the equation is solved using a long, finite time $t_{obs}$. This is the basis for molecular dynamic simulation, which will be discussed in section 6.3 (Allen and Tildesley 1987).

Time-averaging is not the approach used in conventional statistical mechanics, because of the complexity of the time evolution of $A$ ($\boldsymbol{\Gamma}(t)$), which becomes problematic for large numbers of molecules. For this reason Gibbs, the founder of statistical mechanics, suggested replacing the time average with an ensemble average. An ensemble is here considered to be a collection of points $\boldsymbol{\Gamma}$ in phase space. These points are distributed according to a probability density $\rho$ ($\boldsymbol{\Gamma}$), a function which is determined by the macroscopic parameters chosen to be fixed for the system. The possible ensemble types are the microcanonical *NVE* (constant number of molecules, volume and energy) ensemble, the canonical *NVT* (constant number of molecules, volume and temperature) ensemble, the isothermic-isobaric *NPT* (constant number of molecules, pressure and temperature) ensemble, and the grand canonical $\mu VT$ (constant chemical potential, volume and temperature) ensemble. For each of these ensemble types the

listed macroscopic parameters are fixed. The probability density uses the general notation $\rho_{ens}$, with the specific notation of $\rho_{NPT}$, $\rho_{NVT}$ etc. depending on the type of ensemble used. If $\rho_{ens}(\boldsymbol{\Gamma})$ represents an equilibrium ensemble, then its time-dependence completely vanishes. Instead, each point in the ensemble represents a system at any particular instant of time. Note that all these system still evolves in time in accordance with the usual mechanic equations of motion, independently of the other systems. The calculation of properties however, does not depend on time anymore, as the calculation of all the systems are done at the same instant in time (Allen and Tildesley 1987).

The canonical ensemble, i.e. a system where the number of molecules *N*, volume *V*, and temperature *T* are held constant, was the one simulated in this work. The probability density of a phase-space point in the canonical ensemble will be proportional to the Boltzmann's factor

$$\exp(-\mathcal{H}(\boldsymbol{\Gamma})/k_b T)$$

where $\mathcal{H}(\boldsymbol{\Gamma})$ is system's Hamiltonian, and $k_b$ is Boltzmann's constant (Eqs. (2.1.12) and (3.1.1) of Frenkel and Smit (2002)).

The partition function, which is a sum of probabilities for all possible configurations, can be rewritten in quasi-classical form for an atomic system. It takes the following form in case of *N* monoatomic spherical molecules (Allen and Tildesley 1987):

$$Q_{NVT} = \frac{1}{N!}\frac{1}{h^{3N}}\int d\boldsymbol{r}d\boldsymbol{p}\exp(-\mathcal{H}(\boldsymbol{r},\boldsymbol{p})/k_b T) \qquad \textbf{(6.3)}$$

This equation is still a sum of the probability density configurations, where *h* is Planck´s constant.

Unlike the microcanonical ensemble, all energy values are allowed in the canonical ensemble, and the energy fluctuations will be non-zero. However, as equation (6.3) indicates, the probability for each possible energy state, along with the corresponding distribution of configurational energy (interaction energies and other position dependant energies) and ideal-

gas (kinetic) energy, is what will determine whether the state has a large impact on the simulation result (Allen and Tildesley 1987).

## 6.2 Computer Simulations

Why is computer simulation needed? As discussed in section 6.1, some statistical mechanical problems can be solved for exact solutions, while in other cases the system is too complex to be solved analytically by the use of simple approximations schemes. The system complexity might even make it difficult to construct or use the correct theories for the case. In these cases, computer simulation can be a valuable tool. Computer simulations can provide good results where otherwise inaccurate approximations would be used (Allen and Tildesley 1987).

Computer simulations might offer valuable insights to the experimentalist, and thus aid in the interpretation of the results of an experiment. They also have other assets. Computer simulations function as a good link between microscopic and macroscopic systems, which were discussed in section 6.1. In addition to this, simulations can be used to evaluate systems that are difficult or impossible to evaluate experimentally, where the pressure and temperature values are extreme. Examples of such systems might be a nuclear reactor or a planetary core. Also, molecular events are hard to study experimentally due to the small timescale, and are therefore easier to evaluate with simulations (Allen and Tildesley 1987).

The computer simulations conducted in this work were executed using the Cray supercomputer at the University of Bergen (Hexagon). This computer is one of the 100 fastest computers in the world, and is therefore an ideal choice for simulating large simulation systems over a long time, as it provides rapid throughput of data. Hexagon is already being used for research such as medicine, chemistry and economy, and should be suitable for this work as well (Bolstad 2009).

## 6.3 Molecular Dynamic and Monte Carlo simulations

There are two primary methods for computer simulation, Molecular Dynamics and Monte Carlo. The basis of both methods will be explained in this section, starting with Molecular Dynamics.

"Molecular Dynamic simulation is a technique for computing the equilibrium and transport properties of a classical many-body system" (Frenkel and Smit 2002). The word "Classical" in this context means that the nuclear motion of the constituent particles obeys the laws of classical mechanics. This is an approximation that is both valid and useful to make for most materials. Molecular Dynamics (MD) can easily be compared to real world experiments. In both cases, a sample is prepared for the system that is being studied. Then the relevant properties are measured by using the proper equipment. This measurement is done over some time in order to remove noise and other unwanted deviations. The longer these measurements are made, the more accurate the results become. For Molecular Dynamics specifically, the sample here is a model system consisting of *N* particles. The next step is to solve the equations of motion until the system no longer changes with time, or in other words, until system equilibrium is achieved. After system equilibrium is achieved, the system can be measured. To measure an observable quantity in a MD simulation, the observable must be expressed as a function of the positions and momenta of the particles in the system. For instance, the temperature in a many-body system can be defined using the equipartition of energy over all degrees of freedom that enter quadratically in the Hamiltonian of the system. The equation specifically used for the average kinetic energy per degree of freedom can be found in Frenkel and Smit (2002), and is displayed as eq. (6.4) below:

$$\langle \frac{1}{2} m v_{\alpha}^{2} \rangle = \frac{1}{2} k_b T \qquad \textbf{(6.4)}$$

In this equation, $k_b$ is Boltzmann´s constant, and $v_\alpha$ is velocity component in the *x*, *y*, or *z*-direction. This equation makes it possible to link the kinetic energy to temperature during simulations. Because there will be fluctuations in the kinetic energy, the instantaneous "kinetic" value of temperature will fluctuate as well. This is illustrated by equation (6.5) from Frenkel and Smit (2002):

$$T(t) = \sum_{i=1}^{N} \frac{m_i v_i^2(t)}{k_b N_f} \quad \textbf{(6.5)}$$

In this equation, $N_f$ is the number of degrees of freedom and will typically be in the order of $10^3$-$10^4$ in modern simulations. By averaging over time, it is possible to obtain a mean temperature in accordance with equation (6.2) (Frenkel and Smit 2002).

The other method is called Monte Carlo, and is a method based on probability. The Monte Carlo method samples all the possible system states that can occur and takes an average from these to obtain the real system properties. These system states come from a possible configuration change in system, which result in a new molecular distribution, and a new system state, with has a certain probability for occurring. To avoid sampling large amounts of unrealistic states, importance sampling is often used to emphasize the most likely configurations, and ignore the unrealistic configurations. Importance sampling only samples the system states most likely to occur, and therefore the ones that will have the most impact on the average result (Frenkel and Smit 2002).

Since the sampling is centered on probability, it is possible to choose more freely among the options for calculating new possible system states. Where Molecular Dynamics are locked to the classical mechanical equations for the positions and momenta for the molecules, Monte Carlo can choose freely how to determine new states. One can choose to make random displacement of the molecules, or use some manner of equation to determine the displacement (Allen and Tildesley 1987).

This work uses Molecular Dynamics, because of the kinetic processes occurring in the system (Hydrate growth, water adsorption on hematite etc.). Because of these processes, Monte Carlo was considered unsuitable for this work, as these kinetic changes cannot be monitored well in a MC simulation. The use of MD simulation provides numerical values for system properties, as well as a visual representation of the system, where changes in system structure can be observed with programs such as Visual Molecular Dynamics (VMD). VMD is a program designed to visually display and analyze molecular assemblies, especially biopolymers such

as proteins and nucleic acids. The VMD program has been used frequently in this work to construct and inspect the simulations, and is a valuable tool for inspecting and manipulating molecular structures visually (Humphrey et al. 1996).

The MD simulations conducted in this work were executed by a program called MD43. Vassdal (2010) states that this program is a heavily modified version of the M.Dyna*Mix* simulation package, which was created by (Lyubartsev and Laaksonen 2000).

## 6.4 Ergodicity

An important aspect of a system is its ergodicity. The first criteria set for assuming ergodicity, comes from equation (6.6), taken from Frenkel and Smit (2002).

$$\overline{\rho_i(r)} = \lim_{t\to\infty} \frac{1}{t} \int dt' \, \rho_i(r; t') \tag{6.6}$$

Equation (6.6) is the expression of the time-averaged density. From this equation, it is possible to make the assumption that for values of *t* sufficiently long, the time average does not depend on the initial conditions. This leads to the idea that $\overline{\rho_i(r)}$ will not be changed by averaging over many different initial conditions. It is possible to replace the time-averaged density with an ensemble average. This leads to equation (6.7), taken from Frenkel and Smit (2002):

$$\overline{\rho_i(r)} = \lim_{t\to\infty} \frac{1}{t} \int dt' \langle \rho_i(r; \boldsymbol{r}^N(0), \boldsymbol{p}^N(0), t') \rangle \tag{6.7}$$

The ensemble average in this equation is indicated by the <…> brackets. This equation states that if the system is ergodic, then averaging over the initial phase space coordinates of the system equals averaging over the time-evolved phase space coordinates. However, since the ensemble average does not depend on time, it is possible to further simplify the equation. This

leads to the ergodic hypothesis equation, found in Frenkel and Smit (2002), and shown as eq. (6.8) below:

$$\overline{\rho_i(r)} = \langle \rho_i(r) \rangle_{ens} \tag{6.8}$$

This equation states that it is possible to compute the average of a function of coordinates either by time-averaging (MD) or by ensemble-averaging (MC). Note that eq. (6.8) is only plausible, and not necessarily true. However, for computer simulations, it is useful to consider them ergodic (Frenkel and Smit 2002).

If the sampling is taken from only a small amount of the available states, or if the sampling time is too small, the system properties obtained might not be correct. This is important to keep in mind when considering the ergodic properties of the system (Allen and Tildesley 1987).

## 6.5 Periodic Boundary Conditions

For smaller systems, such as a small liquid drop or a microcrystal, the simulation is straightforward. The cohesive forces between molecules may be sufficient to keep the system together unaided during the course of the simulation. If this is insufficient, it is possible to confine the system within a potential representing a container, which keeps them from drifting apart. Unfortunately, these arrangements are insufficient when it comes to a bulk liquid, because of the large number of molecules on the surface of any small sample. This is problematic because of the different forces these molecules experience. This problem can be fixed by implementing periodic boundary conditions. The cubic box containing the system is replicated throughout space, creating an infinite lattice. Since the box is replicated infinitely, the other boxes copy the changes of the central box. For example, when a molecule leaves at the top of the central box, it enters the bottom of the copied box on top. Simultaneously, the box below the central mimics the central box, resulting in a new molecule entering the central box from below. This is illustrated in Allen and Tildesley (1987), and a new figure has been created based on this. The process is shown by Figure 6.1 below.

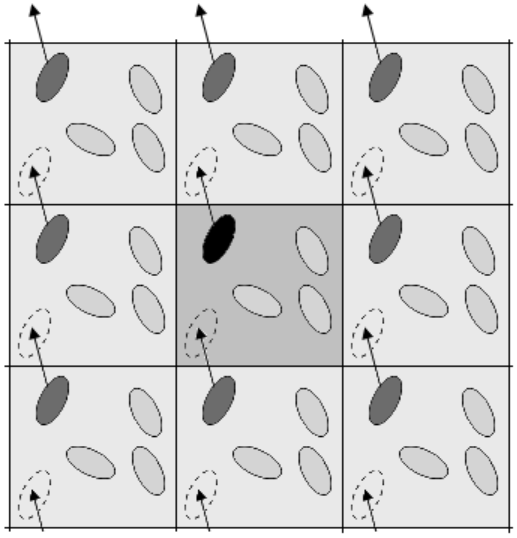

**Figure 6.1 - Two-dimensional periodic system.**

These conditions keep the number density conserved for the central box. It is not necessary to store the coordinates of all the images, just the molecules in the central box. When a molecule leaves the central box, the focus can be shifted to the molecule entering the central box.

When using Periodic Boundary Conditions, it is also important to consider the effects that this imposes on the calculation of system properties. Molecular Dynamic programs need to calculate the potential energy for the different configurations, as well as the forces acting on all the molecules. In order to do this, all the interactions between a specific molecule (such as molecule 1 in Figure 6.2) and every other molecule in the simulation box must be included. This calculation included $N$ - 1 terms. However, the interactions between the molecule and all the molecules in the other boxes must also be included, which is an infinite number of terms. Obviously, this cannot be done. For a short-range potential energy function, it is possible to restrict this summation by making an approximation. In order to properly demonstrate this, a figure from Allen and Tildesley (1987) has been reproduced. This figure can be seen as Figure 6.2 below.

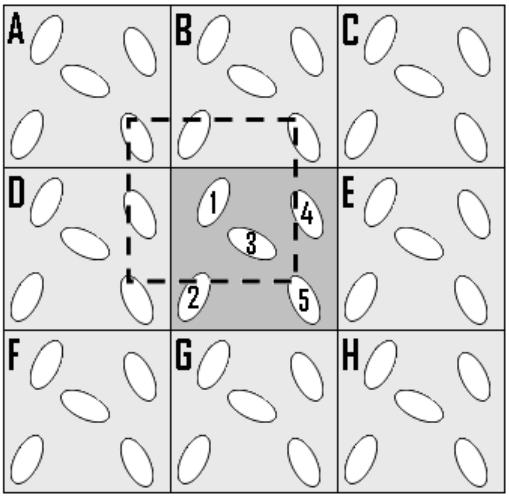


**Figure 6.2 – The minimum image conversion in a two-dimensional system.**

Consider molecule 1 at the center of the dashed region. This region has the same size and shape as the simulation box. Molecule 1 interacts with all molecules which have their centers within this region, in other words, the closest molecules of the other $N$ - 1 molecules. This is known as the "minimum image conversion". In Figure 6.2, molecule 1 interacts with molecule 3 from the center simulation box, as well as 5A, 2B and 4D from the duplicate boxes. In the minimum image conversion, the calculation of the potential energy from pairwise interaction involves $\frac{1}{2}N(N-1)$ terms. Still, this is a massive calculation for larger systems above 1000 particles. Another approximation is needed to make the calculation simpler. The largest contribution to the potential and forces comes from the neighbours closest to the molecule of interest, and therefore it is common for short-range forces to add a spherical cutoff. This is illustrated in Allen and Tildesley (1987), and has been remade as Figure 6.3 below.

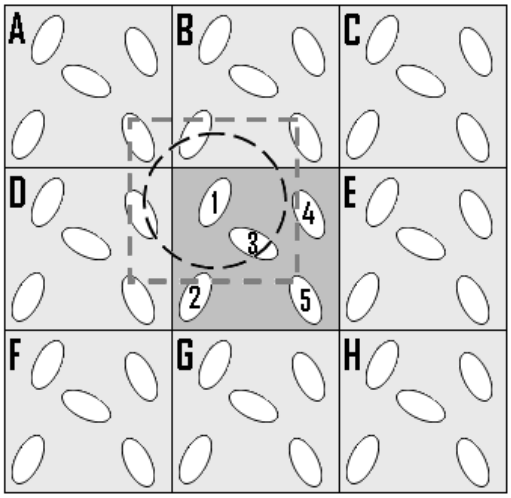


**Figure 6.3 – A potential cutoff radius in a two-dimensional system**

Using a spherical cutoff means setting the pair potential $v^{(r)}$ to zero for $r \geq r_c$, where $r_c$ is the radial cutoff distance. The dashed circle in Figure 6.3 represents a possible cutoff, and in this case only molecule 3 contributes to the force on 1, because the center of molecule 3 is within the cutoff. For a cubic simulation box of length $L$, the number of neighbours explicitly considered is reduced by a factor of approximately $4\pi r_c^3/3L^3$, which might be a substantial saving. Using a spherical cutoff should only be a small perturbation, and therefore the cutoff distance should be sufficiently large to ensure this. For example, in the simulation of Lennard-Jones atoms, the value of the pair potential at the boundary of typical radius $r_c = 2{,}5\sigma$ is just 1.6 percent of the well depth. As for Figure 6.3, an increase in cutoff distance would probably be needed to ensure a sufficient potential comparison. The penalty of applying such a spherical cutoff is that the system properties of the model fluid will no longer be exactly the same, which reflects the need for the most important pair interactions to be included in the cutoff distance. The cutoff distance must be no greater than $\frac{1}{2}L$ in order to be consistent with the minimum image conversion. It is possible to correct for the cutoff by including a correction for the missing long-range forces. This is usually done by integrating the area from $r_c$ to infinity (Allen and Tildesley 1987). This does however assume a uniform distribution of equal molecules outside the cutoff, which means that this approach will not be used in this work, as the simulation system is not uniformly distributed with regards to density and molecule types. Instead, other methods are used to correctly calculate the potential energy and pressure. The Ewald summation method is the method used for calculating the long-range forces, and it will be described in section 7.2.2.

## 6.6 Radial Distribution Function

The radial (pair) distribution function, also known as RDF, describes the probability of finding a particle within (r, r+*dr*) of another particle, thus it describes a *conditional* probability. This is a relative probability for an ideal gas, as all points within the volume *V* have equal probability. This function is used to create a graph that visualizes at what distances from particle *i* other particles of the chosen type were found. This can therefore be described as a density distribution. For a fluid, the average system density is $\rho = N/V$. The exact density at the location of particle *i* can be determined by including a correlation function $g^{(n)}$. The most useful correlation function is $g^{(2)}(\boldsymbol{r}_1, \boldsymbol{r}_2)$, as it relates the correlation between pairs of atoms, and can be determined experimentally as well as from simulations. In a liquid of spherically symmetrical molecules, it only depends upon the relative distance between particle 1 and 2, i.e. $r_{12}$. Since this is the most important correlation, $g^{(2)}(r_{12})$ is often renamed $g(r)$ (McQuarrie 2000). In the canonical ensemble, the pair correlation function can be written as equation (6.9) from Allen and Tildesley (1987):

$$g(r) = \frac{V}{N^2} \langle \sum_i \sum_{j \neq i} \delta(\boldsymbol{r} - \boldsymbol{r}_{ij}) \rangle \qquad \textbf{(6.9)}$$

The influence of the molecule at the origin diminishes as $\boldsymbol{r}$ becomes large. From this it is established that when $\boldsymbol{r} \to \infty$, $g(r) \to 1$. Thus $g(r)$ is the radial distribution function, showing the density distribution as a function of the distance between a pair of particles (McQuarrie 2000).

An example RDF is shown below in Figure 6.4. This particular RDF was obtained from simulations of a reference system containing TIP4P water and EPM2 $CO_2$ molecules, which was simulated in this work for comparative purposes.

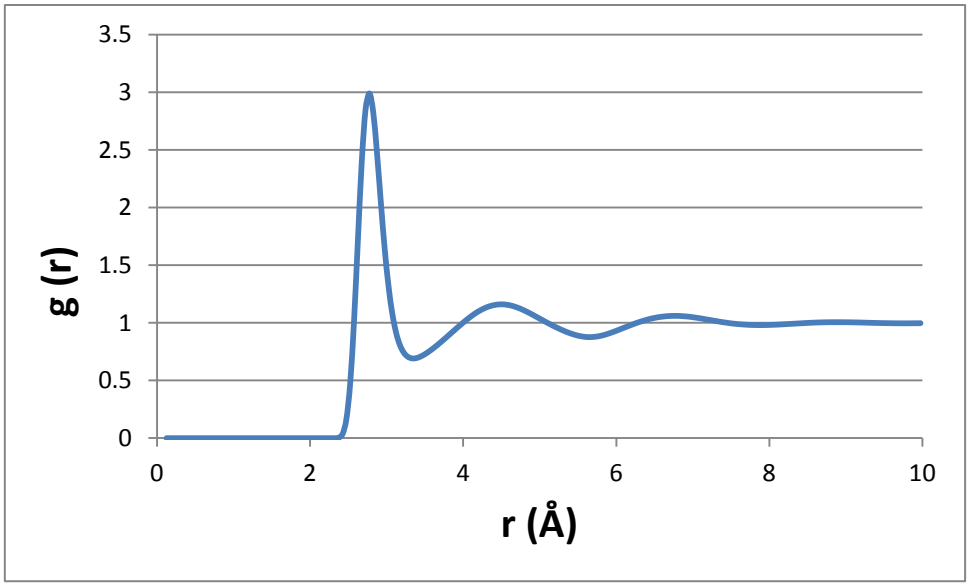


**Figure 6.4 - RDF curve for the oxygen - oxygen interactions in water.**

Note that each top indicates a distance where a large number of oxygen atoms can be found near oxygen. In this case, the largest concentration of oxygen molecules near other oxygen molecules in water was found at a distance of 2.75 Å. The next peaks are found at 4.3 Å and 6.6 Å, indicating other distances where concentrations of oxygen can be found. The fourth peak is barely visible, and is therefore not considered to be part of a structure. Note that in a liquid, the second and third peaks are visibly smaller. The RDF curves of solid crystals such as hydrate have larger peaks beyond the first one, as the molecules are arranged in a less chaotic fashion.

## 6.7 Quaternion

A method for treating the orientational equations of motion is the use of quaternions. The quaternion *Q* is a set of four scalar quantities, as demonstrated by equation (6.10) from Allen and Tildesley (1987).

$$Q = (q_0, q_1, q_2, q_3) \tag{6.10}$$

Note that the three last elements of the equation can be seen as a vector. As seen above in equation (6.10), the four quaternions are linked by one algebraic equation, where only one of the variables can be viewed as "redundant".

Quaternions are very useful for avoiding singularities in the equations, as they eliminate the need for three independent coordinate variables. Therefore, quaternions fulfill the requirements of having well-behaved equations of motion (Allen and Tildesley 1987).

In this work, the quaternions are used to fix the geometry of the molecules, keeping the bond angles and bond lengths rigid. Therefore the molecules are considered to be rigid. Previous simulations discussed in Levitt et al. (1997) debate whether the flexibility of a model actually improves the molecular structure and the diffusion constant. The flexibility properties will be discussed further with regards to the F3C water model in section 8.1.3, which is the only water model in this work which is normally treated as flexible (Levitt et al. 1997).

## 6.8 Statistical error in MD

For an infinitely long simulation, the data obtained for a given model can be considered to be accurate. Unfortunately, this is not possible to do in reality. The simulation will therefore always have some level of statistical error, which must be estimated. The relative variance in an average for an MD system is given as equation (6.11) from Frenkel and Smit (2002):

$$\frac{\sigma^2(A)}{\langle A\rangle^2} \approx \left(\frac{2t_A^c}{\tau}\right)\frac{\langle A^2\rangle - \langle A\rangle^2}{\langle A\rangle^2} \qquad \textbf{(6.11)}$$

In this equation, $A$ is a dynamic quantity, $\tau$ is a finite time for which the simulation average is taken, and $t_A^c$ is the characteristic decay time. The equation shows that the root-mean-square error in $A_\tau$ is proportional to $\sqrt{2t_A^c/\tau}$. This means that the variance in a measured quantity is inversely proportional to the number of uncorrelated measurements. This is very important, because it shows directly how the lifetime and amplitude of the fluctuations in $A$ affect the statistical accuracy. Because it takes more computational effort to calculate a time correlation function than it does to calculate a static average, it is useful to estimate statistical errors from the behavior of block averages. The block averages is simply a time average over a finite time

$t_B$, and is considered a static quantity. For a simulation, it is possible to accumulate block averages for a block length equal to $t_B$. After the simulation is completed, it is possible to compute the block averages for block lengths equal to $n \times t_B$. This is done easily by taking the average of $n$ blocks of length $t_B$. The variance in the block averages is shown as equation (6.12) from Frenkel and Smit (2002):

$$\sigma^2(\overline{A}_B) = \frac{1}{n_B}\sum_{b=1}^{n_B}\left(\overline{A}_B - \langle A\rangle\right)^2 \qquad \textbf{(6.12)}$$

The analysis of block averages is a powerful tool to determine whether a simulation is long enough to yield a reliable estimate of a specific quantity. If for example $P_B$ is dependent on $t_B$ after a time $\tau$, the simulation is too short (Frenkel and Smit 2002). The simulations conducted in this work used block averages from each 5000 time steps.

## 6.9 Methods for calculating the chemical potential

The following sections describe two methods that can be used to calculate the chemical potential in a computer simulation. These methods are called thermodynamic integration and the particle insertion method. Before these methods are explained further, it is useful to explain what the chemical potential is, and why it is useful to calculate it.

The chemical potential $\mu$ is the amount of free energy in a substance that is available for work. The reduction of free energy in the substance equals the maximum amount of energy available for work. The free energy is reduced by spontaneous processes where the pressure and temperature remains constant. The difference of the chemical potential compared to another state, is the driving force for the movement within a substance (such as diffusion). The larger the difference in chemical potential, the more rapid the change becomes. It is also therefore no surprise that chemical potential is an important value for considering thermodynamic equilibrium and phase transitions. The chemical potential depends on the entropy of the system. Therefore, the chemical potential depends on the concentration, pressure and electronic charges in the system. The chemical potential is defined as the amount of free energy per mole substance (J/mol) (Prausnitz et al. 1999).

The chemical potential $\mu$ of species $a$ in a mixture is defined by thermodynamics as equation (6.13) from Frenkel and Smit (2002):

$$\begin{aligned}\mu_a &= \left(\frac{\partial G}{\partial N_a}\right)_{PTN_{b\neq a}} \\ &= \left(\frac{\partial F}{\partial N_a}\right)_{VTN_{b\neq a}} \\ &= -T\left(\frac{\partial S}{\partial N_a}\right)_{VEN_{b\neq a}}\end{aligned} \qquad \textbf{(6.13)}$$

In this equation $G$ stands for Gibbs free energy, $F$ stands for Helmholtz free energy, and $S$ is the entropy.

The chemical potential is measured relatively, meaning that its value must be expressed as a difference from a reference state. This is usually not problematic, as it is the difference in chemical potential that is most interesting to consider in a simulation. As a substance moves, it generates work. The energy level of the substance can be described by the chemical potential (Prausnitz et al. 1999).

In this work, the chemical potential will not be calculated. It will however, be very relevant for further investigations within this field, and thus two methods for calculating the chemical potential have been described here.

### 6.9.1 Thermodynamic integration

Thermodynamic integration is a method that can be used to find the free energy. Just as for real world experiments, it is impossible to directly measure the free energy in computer simulation. This is because quantities such as entropy and free energy are not simply averages of functions of the phase space coordinates of the system. These quantities are directly related to the volume in phase space that is accessible to a system. In experiments, the solution to this problem comes from determining a derivative of Helmholtz free energy, here labeled $F$. This is illustrated by equation (6.14) and (6.15), both found in Frenkel and Smit (2002):

$$\left(\frac{\partial F}{\partial V}\right)_{NT} = -P \tag{6.14}$$

$$\left(\frac{\partial F/T}{\partial 1/T}\right)_{VN} = E \tag{6.15}$$

Both pressure *P* and energy *E* are mechanical quantities, and can be measured in simulation. In order to obtain Helmholtz free energy *F*, it is necessary to reverse these derivations by integrating equation (6.14) and (6.15). This is however easier said than done. Doing so requires an appropriate reference state to compare with. For example, to compute the free energy in a dense liquid, it becomes necessary to construct a reversible path to the very dilute gas phase. This is because a sufficiently diluted gas phase is required to accurately compute the free energy of the reference state. This can be done by using the first terms of the virial expansion of the compressibility factor $PV/(Nk_bT)$. Note that equation (6.14) and (6.15) come from experimental solutions, where macroscopic thermodynamic variables must be used to derive *F*. In simulations, it is possible to choose from a wider range of parameters for deriving *F*, such as all the parameters in the potential energy function. An example of this can be demonstrated by determining the free energy of the Stockmayer fluid, as demonstrated in Frenkel and Smit (2002). This is done by calculating the reversible work needed to switch from a known reference state, which in this case is a Lennard-Jones fluid. The method used for this is called Kirkwood's coupling parameter method. Consider an *N*-particle system with a potential energy function *U*. It is assumed *U* depends linearly on a coupling parameter $\lambda$, which functions in such a way that for $\lambda = 0$, *U* corresponds to the potential energy function of the reference system (L-J), while for $\lambda = 1$, *U* gives the potential energy for the system of interest (Stockmayer). Denoting the reference system as I and the system of interest as II, it is possible to write equation (6.16) from Frenkel and Smit (2002):

$$\begin{aligned} U(\lambda) &= (1-\lambda)U_I + \lambda U_2 \\ &= U_I + \lambda(U_2 - U_I) \end{aligned} \tag{6.16}$$

The free energy difference between system II and I can be obtained by integrating the ensemble average of $\partial U(\lambda)/\partial\lambda$. This is shown as equation (6.17), found in Frenkel and Smit (2002) and written below:

$$F(\lambda = 1) - F(\lambda = 0) = \int_{\lambda=0}^{\lambda=1} d\lambda \left\langle \frac{\partial U(\lambda)}{\partial \lambda} \right\rangle_{\lambda} \qquad \textbf{(6.17)}$$

This is an important result, because it expresses the free energy difference in the terms of an ensemble average (shown as <…> here), which, unlike a free energy, can be calculated directly from a free energy. As the previous section describes, it is now possible to calculate the chemical potential from the free energy (Frenkel and Smit 2002).

### 6.9.2 Particle insertion method

In the previous section, it was stated that one cannot measure thermal properties. This is true, but there are some exceptions to this. No methods can measure the chemical potential, but there are some methods that can measure the excess chemical potential, which is the difference between the chemical potential of a given species and that of an ideal gas under the same conditions. One of these methods is called particle insertion method.

The particle insertion method is also known as the Widom method, and is a simple and effective method for measuring the chemical potential of a species in a pure fluid or in a mixture. The method that was originally introduced by Widom was based upon the random insertion of a particle into an *N*-particle system. This was called the "brute-force" approach, as it did not consider where this particle was inserted. A new variant was therefore introduced, and this method was dubbed the "cavity insertion Widom" (Frenkel and Smit 2002). This variant only inserted the particle into cavities with a suitably large radius. This improved the speed and accuracy of the original Widom method (Jedlovszky and Mezei 2000).

As the system of this work uses the canonical ensemble, the Helmholtz free energy for a canonical system is given below. This equation is from Frenkel and Smit (2002) and is labeled equation (6.18).

$$
\begin{aligned}
&F(N,V,T)\\
&= -k_b T ln Q\\
&\qquad = -k_b T ln\left(\frac{V^N}{\Lambda^{dN}\, N!}\right)\\
&\qquad\qquad - k_b T ln\left\{\int d\boldsymbol{s}^N exp[-\beta U(\boldsymbol{s}^N; L)]\right\}\\
&= F_{ideal}(N,V,T) + F_{excess}(N,V,T)
\end{aligned}
\tag{6.18}
$$

In this equation, $\mathbf{s}^{\mathrm{N}} = \mathbf{r}^{\mathrm{N}}/\mathrm{L}$ represent the scaled coordinates. In equation (6.18), $U(\boldsymbol{s}^N; L)$ is included to indicate that *U* depends on real coordinates, not the scaled ones.

In the last line of equation (6.18), one can see that the Helmholtz free energy has been separated into two different contributions; the ideal gas contribution, and the excess part. For a large value of *N*, the ideal gas contribution disappears, and the following expression for the chemical potential can be written as equation (6.19).

$$
\mu = -k_b T ln(Q_{N-1}/Q_N) \tag{6.19}
$$

This equation can be investigated further by writing it in the explicit form from equation (6.18) for $Q_N$, as shown in eq. (6.20).

$$
\begin{aligned}
&\mu = -k_b T ln(Q_{N-1}/Q_N)\\
&= -k_b T ln\left(\frac{V^N/\Lambda^d}{N+1}\right) - k_b T ln\left\{\frac{\int ds^{N+1} exp[-\beta U(\boldsymbol{s}^{N+1})]}{\int d\boldsymbol{s}^N exp[-\beta U(\boldsymbol{s}^N)]}\right\}\\
&\equiv \mu_{ideal}(\rho) + \mu_{excess}
\end{aligned}
\tag{6.20}
$$

Both equation (6.19) and (6.20) was found in Frenkel and Smit (2002). In the last line of eq. (6.20), the chemical potential has been separated into an ideal gas contribution $\mu_{ideal}$ and an excess contribution $\mu_{excess}$. Because $\mu_{ideal}$ can be evaluated analytically, the focus is on determining $\mu_{excess}$.

In order to do this, the potential energy of the $N+1$-particle system is separated into the potential energy function of the *N*-particle system $U(\boldsymbol{s}^N)$, while the interaction energy of the $(N+1)$ th particle is included with the rest: $\Delta U \equiv U(\boldsymbol{s}^{N+1}) - U(\boldsymbol{s}^N)$. By using this separation, it is possible to rewrite $\mu_{excess}$ into another equation from Frenkel and Smit (2002), here labeled equation (6.21):

$$\mu_{excess} = -k_b T ln \int d\boldsymbol{s}_{N+1} \langle \exp(-\beta \Delta U) \rangle_N \qquad \textbf{(6.21)}$$

Here, $<\ldots>_N$ denotes canonical ensemble averaging over the configuration space of the N-particle system. The point here is that eq. (6.21) expresses $\mu_{excess}$ as an ensemble average that can be sampled by the conventional Metropolis scheme (Metropolis et al. 1953). There is one difference in the equation from conventional computer simulation; it is necessary to compute the average over the position of particle $N+1$. This last integral can be sampled using "brute-force" Monte Carlo. The procedure is like this: one carries out a conventional constant-NVT Monte Carlo simulation on the system of *N* particles. At frequent intervals during the simulation, a coordinate $\boldsymbol{s}_{N+1}$ is generated randomly and uniformly over the unit cube. For this value of $\boldsymbol{s}_{N+1}$, $\exp(-\beta \Delta U)$ is calculated. By averaging the latter quantity over all trial generated positions, the average from equation (6.21) is obtained. So effectively, the average of the Boltzmann factor is computed by the random insertion of an additional particle in an *N*-particle system, which is never accepted as a trial insertion, because the sampling would no longer be of the needed average in eq. (6.21) (Frenkel and Smit 2002).

## 6.10 Nosé-Hoover Thermostat

The simplest form of molecular dynamics reproduces the microcanonical ensemble (NVE), in which the total energy is conserved. It can in theory be used to simulate any system of interest under *NVE* conditions, as long as the number of molecules is large enough. Unfortunately, there is a problem with this. Once the initial conditions and velocities have been assigned to the atoms, the forces and equations of motion control any further development. That is problematic because the user no longer has any control over the resulting temperature or pressure in the system. The solution to this problem is to modify the MD-algorithm to use the canonical, statistical ensemble (NVT), where the temperature *T* is held constant through coupling to an external system that acts as a heat bath. The Nosé-Hoover thermostat is used for this purpose (Kuznetsova 2001).

The Hoover formulation of the Nosé-Hoover thermostat starts from a set of coupled equations of motion, instead of a Hamiltonian. It is based on the following set of coupled equations, found in Kuznetsova (2001):

$$m_i \frac{dv_i}{dt} = \boldsymbol{F}_i - \eta_{tr} m_i v_i \tag{6.22}$$

$$\boldsymbol{F}_i = -\sum_{i \neq j} \frac{\partial U_{ij}}{\partial \boldsymbol{x}_j} \tag{6.23}$$

$$\frac{\partial \eta_{tr}}{\partial t} = \left[\sum m \boldsymbol{v}_i^2 - X_{tr} k T_{tr}\right] \Big/ Q_{tr} \tag{6.24}$$

$$\frac{\partial \eta_{rot}}{\partial t} = \left[\sum \boldsymbol{j}_i \boldsymbol{w}_i - X_{rot} k T_{rot}\right] \Big/ Q_{rot} \tag{6.25}$$

$$\frac{\partial \boldsymbol{j}_i}{\partial t} = \boldsymbol{t}_i - \eta_{rot} \boldsymbol{j}_i \tag{6.26}$$

$$\boldsymbol{t}_i = -\sum_{i \neq j} \frac{\partial U_{ij}}{\partial \boldsymbol{x}_j} \times \boldsymbol{x}_j \qquad \textbf{(6.27)}$$

$$\frac{\partial \boldsymbol{q}}{\partial t} = \boldsymbol{Q}\widehat{\boldsymbol{w}} \qquad \textbf{(6.28)}$$

Note that in equations (6.22) - (6.28), $\boldsymbol{x}$ represents the center of mass (COM) coordinates, $U$ - potential, $m_i\boldsymbol{v}$ - translational momenta, $\boldsymbol{j}$ - angular momenta, $\boldsymbol{F}$ – forces, $\boldsymbol{t}$ – torques, $\boldsymbol{I}$ – moment of inertia tensor, $\boldsymbol{w}$ – angular velocity related to angular momentum by $\boldsymbol{w} = \boldsymbol{I}^{-1}\boldsymbol{j}$, $\widehat{\boldsymbol{w}}$ – transposed body-centered angular velocity augmented by a zero to form a four-component vector, $\boldsymbol{q} = [q_0, \ q_1, q_2, q_3]^T$ – four-component quaternion representing the orientation of the molecule, $\boldsymbol{Q}$ – matrix built up of the quaternions, which can be found in Allen and Tildesley (1987), and is labeled equation (3.37) in Allen and Tildesley (1987), $T_{tr}$ and $T_{rot}$ – desired translational and rotational temperatures, $\eta_{tr}$ and $\eta_{rot}$ – translational and rotational friction parameters of Hoover formulation from (Hoover 1985), $X_{tr}$ and $X_{rot}$ – number of respective degrees of freedom, $Q_{tr}$ and $Q_{rot}$ – thermostat masses determining response times.

These equations are valid for a rigid system of molecules, where the molecular movement can be separated into translational motion of the COMs and rotational motion around the COMs. If all the motion in the system had been restricted to simple translations under the influence of forces dependant on positions only, or more specifically, the negative gradients of potential interactions, then the equations set above could have easily been solved with the "velocity" formulation of the Verlet algorithm. This "velocity Verlet" starts from positions, momenta, and forces at the same time *t*. The positions are first advanced by the "old" forces, as demonstrated in eq. (6.29) from Kuznetsova (2001):

$$x_i(t + \delta t) = x_i(t) + \delta t v_i(t) + {}^1\!/_2\, \delta t^2 \, f_i(t)/m_i + O(\delta t^3) \qquad \textbf{(6.29)}$$

The momenta on the other hand, are first propagated half a time step by the "old" forces, and are then again a half step by the "new" forces calculated from advanced positions, as shown in eq. (6.30) from Kuznetsova (2001):

$$m_i v_i(t+\delta t) = m_i v_i(t) + {}^1\!/_2\,\delta t[f_i(t+\delta t) + f_i(t+\delta t)] + O(\delta t^2) \tag{6.30}$$

The equation set (6.22) - (6.28) differs from the simple scheme of eq. (6.29) and (6.30) with respect to two important reasons:

1. Introducing the momentum-dependant friction coefficient $\eta(t)$ in equation (6.22) and (6.26) results in both the loss of time-reversibility, as well as it makes it impossible to apply the rotational counterpart of eq. (6.30) directly. An alternative approach by Toxvaerd is described in Kuznetsova (2001). This MD algorithm for the Nosé-Hoover thermostat is able to generate a canonical distribution of kinetic energy even for simple systems where Nosé-Hoover would normally be insufficiently chaotic.
   From $r_i(t)$, $v_i(t)$ and $\eta(t)$, the velocities can be updated as

$$m_i v_i\left(t + {}^1\!/_2\,\delta t\right) = m_i v_i(t) + {}^1\!/_2\,\delta t[f_i(t) - \eta(t) v_i(t)] + O(\delta t^2) \tag{6.31}$$

$$\begin{aligned} x_i(t+\delta t) &= x_i(t) + \delta t v_i(t) + {}^1\!/_2\,\delta t^2\,[f_i(t) - \eta(t) v_i(t)]/m_i + O(\delta t^3) \\ &= x_i(t) + \delta t v_i\left(t + {}^1\!/_2\,\delta t\right) + O(\delta t^3) \end{aligned} \tag{6.32}$$

   From these equations, it is possible to update the friction parameter $\eta$ as

$$\eta(t+\delta t) = \eta(t) + \delta t \frac{\sum_i [v_i(t + 1/2\,\delta t)]^2 - gT}{Q} + O(\delta t^3) \tag{6.33}$$

The forces at $t + \delta t$ are now calculated from advanced positions.

Based on this derivation from Kuznetsova (2001), it is now possible to derive an equation for bringing the velocities another half step forward to $t + \delta t$. This results in eq. (6.34):

$$\begin{aligned} v_i(t + \delta t) = v_i\big(t \\ + {}^1\!/_2\, \delta t\big) \\ + {}^1\!/_2\, \delta t[f_i(t + \delta t) - \eta(t + \delta t) v_i(t + \delta t)] \\ + O(\delta t^2) \end{aligned} \qquad \textbf{(6.34)}$$

Finally, by solving eq. (6.34) for the velocities, equation (6.35) is obtained:

$$m_i v_i(t + \delta t) = \frac{m_i v_i(t + \delta t) + 1/2\, f_i(t + \delta t)}{1 + 1/2\, \eta(t + \delta t)} + O(\delta t^2) \qquad \textbf{(6.35)}$$

2. The angular velocity $\boldsymbol{w}$ depends on the orientation (quaternions $\boldsymbol{q}$ of eq. (6.28)) through the inertia tensor, and is used to propagate the angular momenta the first half step. The problem is that in this process, no orientation knowledge is generated, making it impossible to calculate the rotational kinetic energy at the half-step, which is needed in the Toxvaerd handling of the Nosé-Hoover thermostat discussed above. This problem is solvable by deriving an implicit equation for the orientation at half-step. This can be done by using an algorithm found in Kuznetsova (2001). The full details of the algorithm will not be listed here, but it can be explained as a 9-step procedure:

   Step 1: Translational momenta are propagated through the first halfstep

   Step 2: Fullstep propagation of COM positions

   Step 3: Angular momenta are propagated through the first halfstep

   Step 4: Quaternions at $t + {}^1\!/_2\, \delta t$ are obtained by iteration

   Step 5: Thermostatting

   Step 6: Quaternions are propagated full step

Step 7: COM positions at $t + \delta t$ (step 2), quaternions at $t + \delta t$, and $Q(t + \delta t)$ (step 6) are all used as input to calculate positions, forces and torques

Step 8: Translational momenta are propagated through the second halfstep

Step 9: Angular momenta are propagated through the second halfstep

All simulations in this work needed to be kept at a temperature of 4 °C, in order to reflect pipeline conditions. The Nosé-Hoover thermostat was successfully used for this purpose.

## 6.11 Pressure control in MD simulations

The pressure calculation in MD simulations is done using the virial theorem. The virial theorem can be written in the form of "generalized equipartition" for any generalized coordinate $q_k$ . This equation, found in Allen and Tildesley (1987), is shown below as eq. (6.36):

$$\langle q_k \, \partial \mathcal{H} / \partial q_k \rangle = k_b T \tag{6.36}$$

This equation is derived from the general form in canonical ensemble, and contains the Hamiltonian $\mathcal{H}$, and Boltzmann's constant $k_b$. By deriving equation (6.36), it is possible to obtain the instantaneous "pressure" function, where the average is *P*. This equation can be found in Allen and Tildesley (1987), and is included as eq. (6.37):

.

$$\mathcal{P} = \rho k_b \mathcal{T} + \mathcal{W}/V = \mathcal{P}^{id} + \mathcal{P}^{ex} \tag{6.37}$$

In this equation, the pressure contributions are the sum of the ideal and excess instantaneous pressure contributions, $\mathcal{P}^{id}$ and $\mathcal{P}^{ex}$, while $\mathcal{T}$ is the instantaneous kinetic temperature. For pairwise interactions, the expression for the "internal virial" $\mathcal{W}$ can be found in Allen and Tildesley (1987), and is labeled eq. (6.38) here.

$$\mathcal{W} = \frac{1}{3} \sum_{i=1} \sum_{j>1} \mathbf{r}_{ij} \cdot \boldsymbol{f}_{ij} = -\frac{1}{3} \sum_{i=1} \sum_{j>1} \mathbf{r}_{ij} \cdot (\nabla_{\mathbf{r}_{ji}} \mathcal{V})_{\boldsymbol{\Omega}_i \boldsymbol{\Omega}_j}$$

$$= -\frac{1}{3} \sum_{i=1} \sum_{j>1} w(\mathrm{r}_{ij}) \tag{6.38}$$

In this equation, $\mathbf{r}_{ij}$ is the vector between the molecular centers, while $\boldsymbol{f}_{ij}$ is the force acting between molecule $i$ and $j$. $\mathcal{V}$ is the total potential energy, while $w(\mathrm{r}_{ij})$ is the intermolecular pair virial function, which is equal to $r \frac{dv(r)}{dr}$. Solving eq. (6.38) gives the necessary value of $\mathcal{W}$, from which the pressure can be calculated with eq. (6.37) (Allen and Tildesley 1987).

These fluctuations can be used to indicate whether a simulation system is near an equilibrium state, as smaller fluctuations in pressure indicate less driving force for changes in the system. The pressure fluctuations are of no greater importance in this work. The values of $P_x$, $P_y$, and $P_z$ are more relevant, because these values can be used to find the interfacial tension $\sigma$ using simple mechanical reasoning. A very important point in this work is that because the hydrate crystal found in the system is fixed in regards to translational molecular movement, the numerical value of the pressure results cannot be trusted. This cannot be corrected either, due to the fixed hydrate crystal.

# 7 Potential models

In section 6.1, the molecular potential energy contribution *V* in the Hamiltonian was discussed. This section will consider the potential energy, examining the different pair potentials and other contributions to the potential energy. There are two types of potential energy contributions to consider; short-range and long-range contributions. These are outlines in the following sections.

## 7.1 Short-range pair-potentials

Consider a simple, small system containing *N* atoms. The potential energy may be divided into different terms, representing the contribution from the coordinates of individual atoms, pairs, triplets etc. This is shown as equation (7.1) from Allen and Tildesley (1987):

$$V = \sum_i v_1(r_i) + \sum_i \sum_{j>i} v_2(r_i, r_j) + \sum_i \sum_{j>i} \sum_{k>j>i} v_3(r_i, r_j, r_k) + \cdots \quad \textbf{(7.1)}$$

The sum $\sum_i \sum_{j>i}$ indicates a summation over all distinct pairs of i and j without counting any pair twice (for example ij and ji); the same must be done when considering triplets etc. The first term in equation (7.1) represents the effect of containment by an external field, such as a container wall. The remaining terms represent interaction between particles. The second term is the most important, and is known as the pair potential. The pair potential is the potential energy contribution from the pairwise interaction of atoms, and is only dependant on the magnitude of the pair separation $r_{ij}$, which comes from the radial difference ($r_i$ - $r_j$) between the atoms. The third term involves the contributions from three-body interactions between three atoms, and this term has a significant impact effect on the potential energy. The fourth term of interactions and higher have little influence on the energy. Unfortunately, it is very time-consuming for a computer simulation to include the triple interaction term. An effective pair potential is used to solve this. The effective pair potential partially includes the average

of the three-body effects, and thus the expression for the potential energy becomes equation (7.2).

$$V = \sum_i v_1(r_i) + \sum_i \sum_{j>i} v_2^{eff}(r_{ij}) \qquad \textbf{(7.2)}$$

The effective pair potential gives a good approximation of the three-body effects, saving valuable simulation time. The price to pay for this is that the effective pair potential may turn out to depend on density, temperature etc., while the pure two-body potential has no such dependency (Allen and Tildesley 1987).

The following sections describe two potential models for short-range interactions, the Lennard-Jones 12-6 potential, and the Buckingham potential.

### 7.1.1 Lennard-Jones potential

One of the simpler pair potentials commonly used in computer simulations is the Lennard-Jones 12-6 potential. The Lennard-Jones 12-6 potential equation is given by eq. (7.3) from Allen and Tildesley (1987):

$$v^{LJ}(r) = 4\varepsilon((\sigma/r)^{12} - (\sigma/r)^{6}) \qquad \textbf{(7.3)}$$

This equation will be discussed soon, but first it might be useful to study the plot of the equation. Figure 7.1 shows a plot of the Lennard-Jones 12-6 potential model. The figure was plotted using the mathematics program MATLAB (Mathworks 2011), and uses parameter values from the SPC-water model.

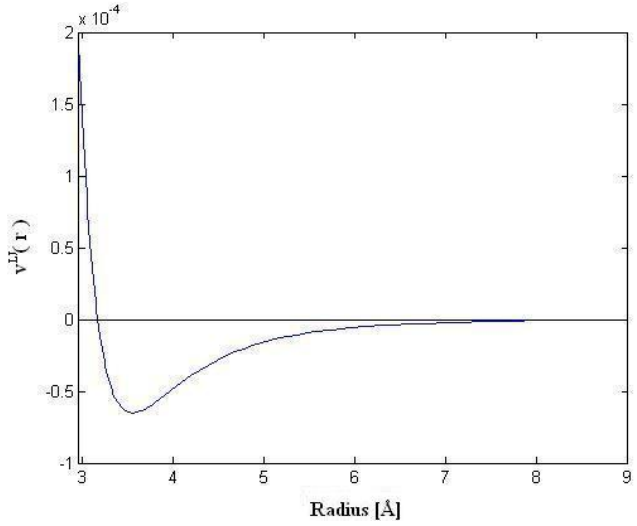


**Figure 7.1 - Lennard-Jones 12-6 potential for SPC water**

From Figure 7.1 it is possible to see the typical repulsive and attractive intermolecular forces for a pair potential. There is an attractive tail at large atomic distances, essentially due to the electron clouds surrounding the atoms. There is also a negative well there, due to cohesion in condensed phases. The final feature of this curve is a steep, rising wall towards infinite repulsion, which represents the repulsive force as atoms get too close. This is due to non-bonded overlap between electron clouds. Using Figure 7.1, it is possible to explain the terms in equation (7.3). The attractive tail is represented by the $-1/r^6$ term, while the curve is most negative at well depth $\varepsilon$. The steep rising wall starts at distances less than $r \sim \sigma$. The well depth is usually quoted in units of temperature by dividing it on the Boltzmann constant $k_B$, i.e. it is given as $\varepsilon/k_B$. From this it is clear that $\sigma$ marks the point where the curve switches between being repulsive and attractive, while the well depth $\varepsilon$ is the value where the strongest attractive energy acts (Allen and Tildesley 1987).

For the Lennard-Jones interactions between different atom types, the Lorentz-Berthelot mixture rules can be used. The Lorentz-Berthelot equations can be found in Allen and Tildesley (1987), and are listed below as equations (7.4) and (7.5) below.

$$\sigma_{CS} = \frac{1}{2}(\sigma_{CC}+\sigma_{SS}) \qquad \textbf{(7.4)}$$

$$\varepsilon_{CS} = \sqrt{\varepsilon_{CC}\varepsilon_{SS}} \quad \textbf{(7.5)}$$

Note that in these equations, the Lorentz-Berthelot mixture rules are stated by considering $CS_2$ as an example. It is possible to see that the cross-terms (C-S) are calculated from the pure (C-C and S-S) interactions.

Both the Lennard-Jones 12-6 potential and the Lorentz-Berthelot mixture rules are used for estimating the short-range forces in this work. The Lennard-Jones potential is a popular method for modeling short-range forces, as it is used in numerous works. Examples of works that use Lennard-Jones are (Berendsen et al. 1981; Jorgensen 1982; Levitt et al. 1997; Cygan et al. 2004).

### 7.1.2 Buckingham Potential

Another method of describing the pairwise interactions is the Buckingham potential. The potential can be expressed as a Buckingham potential, as shown in equation (7.6) from Shilnikov and Shnulin (1992):

$$U_{kj}^{B} = -A_{kj}/r_{kj}^{6} + B_{kj}\exp\{-C_{kj}r_{kj}\} \quad \textbf{(7.6)}$$

In this equation, the subscript indicates the nonbonded atoms k and j, while $r_{kj}$ is the distance between these atoms. A, B and C are adjustable potential parameters. The drawbacks by using Buckingham is that it does not work well with shorter-than-equilibrium distances, as well as the increased computation complexity (when compared with Lennard-Jones) (Shilnikov and Shnulin 1992).

For this work, the Buckingham potential was attempted implemented, but was abandoned because of the problems it caused in the system. When implemented, the hematite crystal fell apart, because the forces were unable to keep it together. The problem was related to the interactions between oxygen in hematite and oxygen in $CO_2$. A guest student researcher,

Brian Ellingwood, has previously attempted to use Buckingham potentials from two different sources (hematite from de Leeuw and Cooper (2007) and pure $CO_2$ from Tsuzuki et al. (1996)) to model interactions between Hematite and $CO_2$. He tried both arithmetic and "harmonic" mixing rules for the interaction parameters, but the resulting $O_{Hem}$-$O_{CO2}$ potential lacked a minimum (de Leeuw and Cooper 2007), (Tsuzuki et al. 1996).

## 7.2 Long-range pair potentials

The short range potentials are sufficient for dealing with most interactions, as most of them have short range. However, in addition to these short-range interactions, there are long-range interactions. The following definition can be used to categorize long-range forces: "A long-range force is often defined as one in which the spatial interaction falls off no faster than $r^{-d}$, where d is the dimensionality of the system" (Allen and Tildesley 1987). The charge-charge interactions between ions are considered long range forces, as are the dipole-dipole interactions between molecules. The long-range forces are a serious problem for the computer simulator, as their range exceeds half the box length of a typical simulation. Calculating the long-range interactions will greatly increase the simulation time required. Therefore, other methods are required to treat the long-range forces (Allen and Tildesley 1987).

The following sections describe the two methods that are used to treat these forces in this work.

### 7.2.1 Coulomb equation

The Coulomb charge-charge interaction equation from Allen and Tildesley (1987) can be added to the potential energy contribution to correct for the long-range forces. The Coulomb interaction equation is given below as eq. (7.7):

$$v^{zz}(r_{ij}) = \frac{z_i z_j}{4\pi\varepsilon_0 r_{ij}} \tag{7.7}$$

The parameters $z_i$ and $z_j$ are the charges of ions $i$ and $j$, while $\varepsilon_0$ is the permittivity of free space (this is not the same as the well depth $\varepsilon$). Note that the factor $4\pi\varepsilon_0$ is sometimes omitted

from the equation. This corresponds to adopting a non-SI unit of charge, as is the case with the equations (7.8) and (7.11) found in Allen and Tildesley (1987). These equations have been converted to SI unit of charge in this paper, and are therefore slightly different that the ones found in Allen and Tildesley (1987).

There is a problem with using equation (7.7). The electrostatic forces are not pairwise additive and are therefore difficult to include in the simulation. To properly determine the electrostatic contribution $v^{zz}(r_{ij})$, one can use the Ewald summation method.

### 7.2.2 Ewald summation

The Ewald summation method can be described as a technique for efficiently summing the interaction between an ion and all its periodic images. The potential energy equation for Ewald summation is found in Allen and Tildesley (1987) and is given as eq. (7.8) below:

$$V^{zz} = \frac{1}{8\pi\varepsilon_0} \sum_{\boldsymbol{n}}{}' \left( \sum_{i=1}^{N} \sum_{j=1}^{N} z_i z_j \left| \boldsymbol{r}_{ij} + \boldsymbol{n} \right|^{-1} \right) \qquad \textbf{(7.8)}$$

In this equation $z_i$ and $z_j$ still represent the charges, while **n** represents the sum over all the cubic lattice points. The vector **n** equals ($n_x L$, $n_y L$, $n_z L$), where $L$ is a distance from the original lattice cube, and $n_x$, $n_y$, and $n_z$ are integer multipliers for each dimension (for example **n** could be ($4L$, $3L$, $L$)). The prime ´ indicates that $i=j$ is omitted for **n** = 0 in the summation. For long-range potential, $V^{zz}$ is conditionally convergent, which means that the result depends on the order in which the terms are added up. The natural choice is to sum those closest to the original box first, and continue outward. The unit cells are therefore added in sequence, starting with **n** = (0, 0, 0), followed by the six boxes centered at **n** = ($\pm L$, 0, 0), (0, $\pm L$, 0), and (0, 0, $\pm L$); etc. The more boxes added in this fashion, the closer the system is to an infinite system in a spherical layer with radius $\infty L$. This concept is illustrated in Allen and Tildesley (1987), and is shown in Figure 7.2.

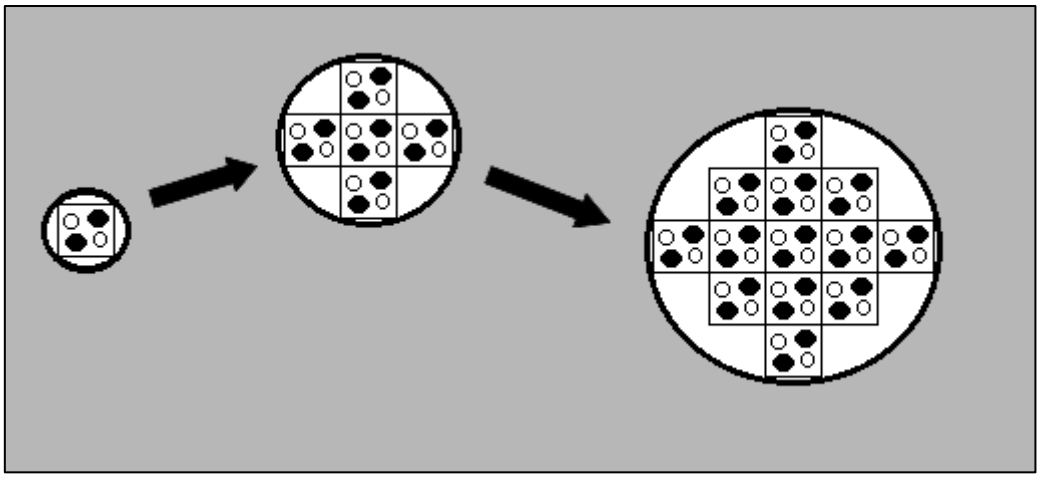

**Figure 7.2 – Building up a sphere of simulation boxes. The gray region represents the external dielectric continuum of relative permeability $\varepsilon_s$.**

When this approach is used, it is necessary to describe the properties of the medium surrounding the sphere, in particular the relative permeability $\varepsilon_s$. The results for a sphere surrounded by a good conductor, such as a metal ($\varepsilon_s = \infty$), are different from the results obtained from a sphere surrounded by vacuum ($\varepsilon_s = 1$). Equation (7.9) from Allen and Tildesley (1987) provides the necessary correction between a system surrounded by a metallic surface, and a vacuum.

$$V^{zz}(\varepsilon_s = \infty) = V^{zz}(\varepsilon_s = 1) - \frac{2\pi}{3L^3}\left|\sum_{i=1} z_i \boldsymbol{r}_i\right|^2 \qquad \textbf{(7.9)}$$

This equation applies in the limit of an infinitely large sphere of boxes. In the vacuum, the sphere has a dipolar layer on its surface, while a sphere surrounded by a metal has no such layer. The last term in eq. (7.9) is the correction for this. The Ewald summation is an efficient method for calculating $V^{zz}(\varepsilon_s = \infty)$, which is fortunate, as the simulations in this paper are based around a system in a pipe. Equation (7.11) is given in Allen and Tildesley (1987) as surrounded by vacuum, making it necessary to explain this correction. It can then be omitted from equation (7.11).

At any point during the simulation, the distribution of charges in the original cell constitutes the unit cell neutrality for all the cells throughout the simulation space. In the Ewald method,

each point charge is surrounded by a charge distribution of equal magnitude and opposite sign, which is centered on the point charge. This distribution is found in Allen and Tildesley (1987), and is given below in equation (7.10):

$$\rho_i^z(\boldsymbol{r}) = z_i\kappa^3\exp(-\kappa^2 r^2)/\pi^{3/2} \qquad \textbf{(7.10)}$$

Here κ is an arbitrary parameter that determines the width of the distribution, and **r** is the position relative to the centre of the distribution. This extra distribution works as an ionic atmosphere, screening the interaction between neighboring charges. The screened interactions are now short-ranged, and the total screened potential can be found by summing over all the molecules in the original cube and all their periodic images in the real space lattice of image boxes. This is illustrated in Allen and Tildesley (1987), and is shown in Figure 7.3(a) below:

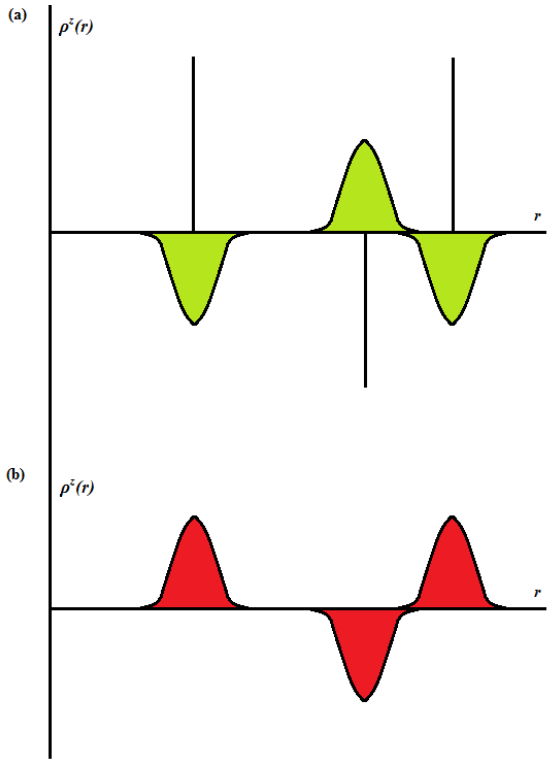


**Figure 7.3 – Charge distribution in the Ewald sum.**
**(a) Original point charges plus screening distribution**
**(b) Cancelling distribution**

A cancelling distribution is also added, with the same amplitude and shape, but with opposite signs. This distribution, shown in Figure 7.3(b), cancels out the screening distribution, reducing the potential to that of the original charges. The cancelling distribution is summed up in reciprocal space. This means that the Fourier transforms of the cancelling distributions are added, and then the total is transformed back into real space. This process requires an important correction, as the recipe includes the interaction of the cancelling distribution centered at $\mathbf{r}_i$ with itself. This self term must be subtracted from the total. Note that it is assumed that Fourier transforms is known to the reader in this work, otherwise knowledge can be obtained from Allen and Tildesley (1987).

After these adjustments, the expression for the final potential energy, found in Allen and Tildesley (1987), is given as equation (7.11) below:

$$V^{zz}(\varepsilon_s = \infty) = \frac{1}{8\pi\varepsilon_0}\sum_{i=1}^{N}\sum_{j=1}^{N}\left(\sum_{|n|=0}^{\infty} z_i z_j \frac{\operatorname{erfc}(\kappa|\boldsymbol{r}_{ij}+\boldsymbol{n}|}{|\boldsymbol{r}_{ij}+\boldsymbol{n}|} + (1/\pi L^3)\sum_{\boldsymbol{k}\neq 0} z_i z_j\,(4\pi^2/k^2)\exp(-k^2/4\kappa^2)\cos(\boldsymbol{k}\cdot\boldsymbol{r}_{ij})\right) - (\kappa/\pi^{1/2})\sum_{i=1}^{N} z_i^2 \qquad \textbf{(7.11)}$$

This equation contains a real space sum plus a reciprocal space sum, minus the self-term mentioned above. Note that eq. (7.11) is given for a system surrounded by a metal, thus eliminating the aforementioned dipolar surface layer in this equation. In this equation erfc ($x$) is the complementary error function which falls to zero with increasing $x$. Thus, if κ is chosen to be large enough, the only contribution to the real space sum is that with $n$ = 0, with the result that the first term reduces to the normal minimum image conversion. The second term is a sum over reciprocal vectors $\boldsymbol{k} = 2\pi\boldsymbol{n}/L^2$. A large κ-value corresponds to a sharp distribution of charge, and many terms must be included in the k-space summation to properly model it. The aim in a simulation is to choose a value of $\kappa$ and a sufficient number of $k$-vectors, so that eq. (7.11) (with the real space sum truncated at $\boldsymbol{n}$ = 0) and eq. (7.9) give the same energy for typical configurations (Allen and Tildesley 1987). For the simulations done in this paper, $\kappa$ was set to be $5/L$. The number of wave vectors used in the $k$-space sum was calculated at the start of each simulation, and kept at this number through the simulation. For

the three core systems, the number of wave vectors was calculated to 8642 in one of the simulation runs.

The Ewald summation method has been used successfully in other works. da Rocha et al. (2001) use Ewald in their simulation studies of the density structure of the water/$CO_2$ interface. They had chosen to use this method because it had previously given good results when used to determine the temperature dependence of surface tension of a free pure water interface for the SPC/E water model, which was used in da Rocha et al. (2001). They were also able to obtain good simulation results by using the Ewald summation method (da Rocha et al. 2001).

# 8 Molecular models

For molecular dynamic simulations, obtaining realistic results is only possible when the parameters of the simplified force fields we use are reflecting the true nature of the molecular interactions. These models are designed to properly describe the behavior of certain molecules, and have many different parameters such as bond length, bond angle, placement of electrostatic charges etc. Because of this, there is a large selection of models with differing parameters, all aiming to better replicate experimentally obtained properties of molecules in various systems. Comparisons between simulated results and their real-life counterparts are commonly performed both when the model in question is first introduced (Levitt et al. 1997), and subsequently when it is used in modeling (da Rocha et al. 2001). It is also common to compare different models, in order to determine their strengths and weaknesses (Jorgensen et al. 1983).

A good model must be able to describe the interaction forces between molecules. The first models developed consisted of identical monoatomic ideal gas molecules, and had therefore no problems with interactions between different atoms. Any realistic simulation will however contain a mixture of different molecules, with many of them being polyatomic molecules. Though it's theoretically possible to perform *ab initio* (quantum chemistry) simulations and try to determine and parameterize the interactions between all different atom-atom combinations, this approach is currently not feasible. This is discussed in the work of Cao et al. (2001), where the *ab initio* approach is used on methane-water interactions, without success (Cao et al. 2001). Because of this, the transferability of a potential becomes a very important alternative for calculating interactions between different molecular species. The transferability of a model determines whether a set of parameters for an atom or a group of atoms can be used to construct potential functions suitable for different systems. For example, this property determines if the Lorentz-Berthelot mixing rules can be used to describe the short-range interactions between oxygen in water and carbon in $CO_2$. Therefore, one should consider if the transferability of the model is good enough for the simulation (Jorgensen 1981). Examples of “universal” transferable potential sets are the CHARMM (Brooks et al. 2009) and AMBER (Weiner and Kollman 1981) force fields.

The rest of this section describes the force field models used in this work.

## 8.1 Water models

Choosing a suitable water model is essential for simulating the correct interactions between water and the other elements in the system. Many water models have been developed to properly describe the properties of water, as it is the most fundamental fluid on the planet. Early work done by Stillinger and Rahman in the 1970s had led to the development of the first water model ever to be used in simulations. This model was called the Ben Naim-Stillinger (BNS) model, and was later reworked into the ST2 model (Berendsen et al. 1987). These and many other water models shared the approach and can be characterized based on the number of charges used. The different types of models are 3-point models, 4-point models and 5-point models. The 3-point models are the fastest to simulate, but are not the most accurate when it comes to reproduction of experimental results. The 4-point models improve the accuracy at the cost of being more complex and computationally expensive. The most complex models are the 5-point models, and although they might be more true to the real water electronic structure, they take significantly longer to simulate than 3-point and 4-point models, as discussed in (Mahoney and Jorgensen 2000). Although these models have increased complexity, it is not guaranteed that they give better results than other model types, as it was concluded in (Jorgensen et al. 1983).

Mahoney and Jorgensen (2000) states that some of the most commonly used and verified water models are SPC, SPC/E, TIP3P, and TIP4P. We had however, many other choices to consider. Because of the many different choices available, three water models were chosen for this work. The chosen models were the TIP4P, SPC/E and F3C water models. All the other water models considered in this work have been listed in Appendix A (Mahoney and Jorgensen 2000).

### 8.1.1 SPC and SPC/E

The Simple Point Charge (SPC) model was developed by Berendsen et al. (1981). The model was developed as a three-point charge model, where the charges were placed in the oxygen and hydrogen atoms. The oxygen atom is the only atom in the model that has a short-range potential modeled by the Lennard-Jones 12-6 function (equation (7.3) in this work). This water model was developed for MD- and MC-simulations because of the need for a simple water model that can be used for costly protein computer simulations. Part of the model´s

simplicity lies in the fact that the charges are fixed at the positions of actual water atoms. Therefore, no costly calculations for finding the new charge locations are necessary. The SPC water molecule from Berendsen et al. (1981) is shown below in Figure 8.1:

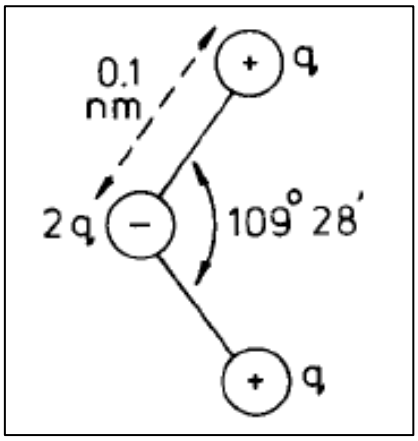


**Figure 8.1 – SPC water molecule found in (Berendsen et al. 1981)**

As seen in this figure, the OH-distance is 0.1 nm, while the bond angle is 109.47˚. The SPC charges for hydrogen and oxygen are $+0.410e$ and $-0.820e$ .

This model was improved in a later work by Berendsen et al. (1981), by including a self-energy correction, as well as a re-parameterization of the model. This model was named the extended simple point charge, or SPC/E. The self-energy term aims to include the average polarization effects from single atoms. This correction for an effective pair potential is found in Berendsen et al. (1981) and is given as equation (8.1) below:

$$E_{pol} = {}^{1}/_{2} \sum_{i} (\mu - \mu^{0})^{2} / \alpha_{i} \qquad \textbf{(8.1)}$$

Here, $\mu$ is the dipole moment of the effective pair potential model, and $\mu^{0}$ is the dipole moment of the isolated molecule. $\alpha_i$ is an isotropic scalar polarizability, assumed for simplicity. This polar correction should be applied to the effective pair potential. The new charges for SPC/E are -0.8476*e* for oxygen and +0.4238*e* for hydrogen (Berendsen et al. 1981).

The transferability of the SPC/E model has been proven by being successfully used in various water-containing systems to reproduce the experimental behavior of water mixed with other molecules. da Rocha et al. (2001) states that the SPC/E model can be used together with the EPM2 model for $CO_2$, a fact that was quite important for our work. da Rocha was able to produce realistic data for the $CO_2$/water interface using these models (da Rocha et al. 2001). The SPC/E has also been used to model hydrate in Svandal et al. (2006) and Tegze et al. (2006) Both of these works were able to successfully investigate hydrate growth, which means that SPC/E should be a suitable candidate for simulating a hydrate crystal (Svandal et al. 2006), (Tegze et al. 2006).

On the other hand, Jorgensen et al. (1983) has compared the SPC model and other three-point models to four-point models such as TIP4P. They concluded that although three-point models have a better overall agreement with experimental data for hydrogen interactions, the oxygen-oxygen interactions of four-point models were superior. Even though the SPC/E model is an improved version of the SPC model, it is still a simple model, and might therefore not provide as accurate results as a four point model such as TIP4P (Jorgensen et al. 1983).

In summary, the SPC/E model is a simple, widely used water model developed for simulation with large protein structures, and has been proven reliable in systems containing $CO_2$. It has also been used to model hydrate crystals, which it will be required to do in this work as well. The advantage of using the SPC/E model is its simplicity and its functionality with other molecules. The drawback of using SPC/E might be that its simplicity will limit its accuracy. This raises the following question: Is the SPC/E model a good choice because of its simplicity, or is it better to use a more accurate model?

### 8.1.2 TIP4P

The 4-point Transferable Intermolecular Potential (TIP4P) model is a rigid four-point charge model for simulating water. The TIP4P water molecule is shown as Figure 8.2 below:

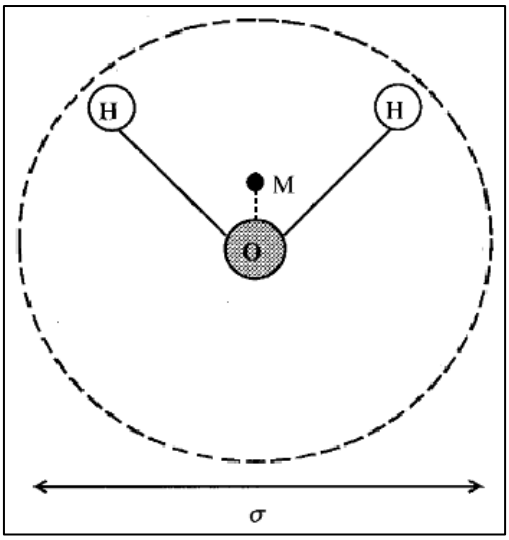


**Figure 8.2 – TIP4P water molecule, taken from (Vlot et al. 1998) and modified by Christian Bøe**

The model has a bond length $r_{OH}$ equal to 0.9572 Å, and a bond angle of 104.52˚. The model has charges placed on the hydrogen atoms equal to $+0.52e$. The remaining charge is put on a partial charge, located at a distance $r_{OM}$ 0.15 Å away from the oxygen, towards the hydrogen atoms in the middle of the water molecule. This charge is equal to $-1.04e$. In addition to this, the oxygen atom has a Lennard-Jones term to describe oxygen-oxygen interactions between the molecules (Gao et al. 2000).

The TIP4P model was created from the TIP3P model to better reproduce the density distribution inferred from the O-O RDF curve (Levitt et al. 1997). Jorgensen et al. (1983) compared the TIP4P water model to other water models and showed that the TIP4P model reproduced the O-O structuring better than TIP3P. The paper further concluded that the TIP4P is one of the best models tested, especially since its density at 25˚C and 1 atm matched the experimental water density (Jorgensen et al. 1983).

The TIP4P water model has been tested with the EPM2 model for $CO_2$ by Vorholz et al. (2000). They concluded that out of all the models considered, TIP4P was one of the best when it came to agreement with the experimental results. This was particularly true in case of the liquid density and further emphasized that the TIP4P model can be used in simulations with $CO_2$ (Vorholz et al. 2000).

The TIP4P model was one of the three models compared in this work because it is one of the most commonly used water models, proven to work successfully with $CO_2$, and able to produce more accurate results than a three-point model. The question investigated in this work, was whether the accuracy given by the extra point potential is worth the extra complexity and extra computer resources.

### 8.1.3 F3C

The Flexible Three-Centered (F3C) model was developed by Levitt et al. (1997). It was described by its developers as a very simple water model suitable for long MD simulations of macromolecules in a solution. Because the model tolerated rather severe truncation of the short-range interactions to increase the simulation speed, this resulted in a decreased number of calculations done each MD step, which drastically reduces the computational time (Levitt et al. 1997).

The average bond lengths and angles, as well as the charges of the F3C model, were identical to the those of the SPC model described in section 8.1.1 (Wu et al. 2006). F3C has its charges placed on the atom centers, and has no constraints for bond length or angle. The potentials are transferable with regards to macromolecules. The main difference between SPC and F3C lies in the fact that F3C includes short-range potentials centered on the hydrogen atoms as well as the oxygen atom, while SPC has only a potential centered on the oxygen (Levitt et al. 1997).

The F3C model is a flexible model with bond lengths and bond angles controlled by force field potentials. This distinguishes it from rigid water models like SPC and TIP3P. It has been debated in the literature whether the flexibility in water molecules improves the molecular structure. The effects from flexibility on the diffusive properties of water are also debated, as different testing has shown both increased and reduced diffusivity (Levitt et al. 1997).

The F3C model has been previously used in research at the University of Bergen, in works such as Vassdal (2010) and Kvamme et al. (2009). Through various testing in Kvamme et al. (2009), it was concluded that using the charges from SPC/E (see section 8.1.1) improved the RDF curves for F3C, as the original SPC structure gave a very flat RDF structure. We

believed that the flexibility of F3C will not have any impact on properties and behavior studied in this work, and thus used quaternion treatment to keep all the molecules rigid (Kvamme et al. 2009), (Vassdal 2010).

The F3C system was chosen for this because it is a good, well-tested model that has been used previously at the University of Bergen. More specifically, because it is a three-point charge model which allows short-range truncation to reduce the simulation time, it was highly relevant due to the large size of the systems investigated in this thesis. There is however reason to question whether the extra LJ potentials located on the hydrogen can have a noteworthy effect compared to the simpler SPC/E model. And even if the F3C model is superior to SPC/E, will it yield better results than the 4-point TIP4P model?

## 8.2 $CO_2$ – models

In order to properly simulate $CO_2$ in the system, a model must be chosen to describe the system characteristics of $CO_2$. For this purpose, the EPM2-model was considered as a suitable candidate. The following section describes the details regarding the original EPM-model, as well as the EPM2-model.

### 8.2.1 The EPM and EPM2 models

Harris and Yung (1995) aimed to develop an accurate but simple physical model for that would reproduce carbon dioxide's solubility and reaction rates in liquid and supercritical state, named the Elementary Physical Model (EPM). Since it was specifically developed for the simulation of multi-component systems, it claims to properly describe the intermolecular interactions that occur when $CO_2$ acts as a solvent. The EPM model uses three Lennard-Jones sites with charges centered at each atom in $CO_2$. The carbon charge is +0.6645, while the oxygen charges are each -0.33225. The carbon-oxygen bonds are modeled as rigid, and are 1.163 Å long. The long-range forces are treated by the Coulomb equation. The unique property of this model is that it has a quadropole moment of 4.3 Buckingham, which is slightly different than the experimental value of 4.1 Buckingham. This model was used to predict the liquid-vapor curve for $CO_2$, with the resulting curves being in good accordance with experimental results.

To improve the agreement with experimental results even further, Harris and Yung used the theorem of corresponding states. This resulted in a slightly corrected version of EPM, which was called EPM2. The EPM2 parameters give a more accurate description of the critical point for $CO_2$, at the cost of a slight deviation of the liquid coexistence densities at lower temperatures (Harris and Yung 1995). The EPM2 molecule can be found in Vorholz et al. (2000) and is depicted in Figure 8.3 below. The carbon charge for EPM2 is +0.6512, while the oxygen charges are each -0.3256. In addition to this, the new carbon-oxygen bonds are 1.149 Å long.

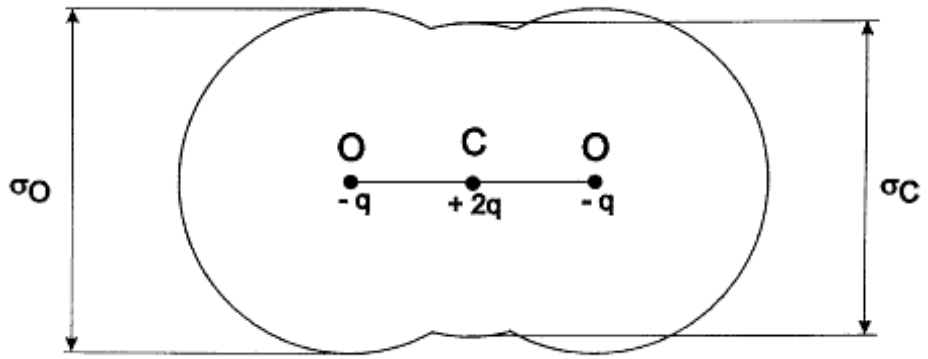


**Figure 8.3 – EPM2 $CO_2$-molecule, taken from (Vorholz et al. 2000)**

The authors of Vorholz et al. (2000) mention that the EMP2 model has been tested with the water models SPC and TIP4P, with the simulation results found to be in a good agreement with the experimental data. The SPC/E model was also investigated by Vorholz, but was not simulated together with EMP2, as the vapor pressures produced deviated more from experimental results than for the other two models (Vorholz et al. 2000),.

The combination of SPC/E with EPM2 was studied in da Rocha et al. (2000). This paper investigates the properties of a supercritical-$CO_2$/water mixture, focusing on the interfacial properties. RDF-curves and other structural data presented in the paper concurred rather well with the realistic picture of the structural quantities expected from such a system.

The results of da Rocha et al. (2000) also contain estimates of properties that are highly relevant for this work. For instance, they point out that just like the real-life water, their water

model exhibited negligible solubility in $CO_2$, which means that diffusion of water into $CO_2$ will be a slow and unfavorable process. On the other hand, the $CO_2$-into-water solubility agreed with the experimental predictions (24 CO2 molecules per 1000 water molecules at 318.15 K and 20 MPa) (da Rocha et al. 2001).

Both the research results outlined above and the previous work of this group made us confident that EMP2 $CO_2$ model will work well in simulations involving water. Therefore, it was the $CO_2$ model chosen for this work.

## 8.3 Hematite model

Force field model parameters from Cygan et al. (2004) were chosen for the Hematite crystal in the simulations. The ClayFF paper was considered relevant because the ClayFF model is strongly based upon the SPC water model. This means that all the model parameters are based upon SPC, which include iron and oxygen parameters suitable for simulating the hematite crystal. This model uses the Coulomb energy equation to handle the long range forces The following sections describe ClayFF, the relevant force field parameters, and the necessary changes made to accommodate the values to MD43 (Cygan et al. 2004).

### 8.3.1 About ClayFF

Cygan et al. (2004) uses the SPC water model as well as non-bonded metal-oxygen interactions to better simulate clay and other hydrated minerals. The special thing about ClayFF is that most interatomic interactions are treated as non-bonded. “This approach allows more flexibility in simulating complex and ill-defined crystal structures containing a large number of atoms and decreases the risk of over-parameterization by drastically reducing the number of analytical expressions and force field parameters necessary to describe the energy of the atomic interactions throughout molecular mechanics simulation” (Cygan et al. 2004). This means that complex systems will need fewer parameters for simulation, as well as fewer calculations during the simulation. This gives an increased chance of convergence and obtaining reliable results, as discussed in chapter 0.

ClayFF uses the Lennard-Jones 12-6 potential for calculating the short-range forces, combined with the Lorentz-Berthelot mixture rules. For the long-range forces, the Coulomb equation is used. This is good, as the same approach has been used in this work, except for

that the Coulomb equation, which in this work has been used to derive the Ewald equation. The differences are therefore the fact that Ewald summation is used instead, as well as the fact that the equations used are in a slightly different form. This makes it necessary to convert some of the parameters before they can be used to model hematite in this work. This conversion is done in section 8.3.3.

### 8.3.2 Force Field Parameters

The chosen force field parameters from Cygan et al. (2004) are listed in Table 8.1:

| Species | **Symbol** | **Charge [e]** | **$D_0$ [kcal/mol]** | **$R_0$ [Å]** |
|---|---|---|---|---|
| **bridging oxygen with double substitution** | obss | -1.2996 | 0.1554 | 3.5532 |
| **octahedral iron** | feo | 1.5750 | $9.0298 \times 10^{-6}$ | 5.5070 |

**Table 8.1 – Selected force field parameters from Cygan et al. (2004).**

These values were considered useful because of the following reasons:

- The octahedral iron parameters were considered for the iron in hematite. By studying the iron structure in the hematite crystal, it became clear that the iron was the center of octahedral groups within the crystal. Figure 8.4 was taken from the unit cell used to build the crystal, by using the program Crystalmaker to hide the rest of the molecule. The Crystalmaker program is a program that can be used to build and modify crystal structures (Palmer and Palmer 2011). Figure 8.4 demonstrates that iron in the crystal is octahedral, as proven by (McCormick 2011).

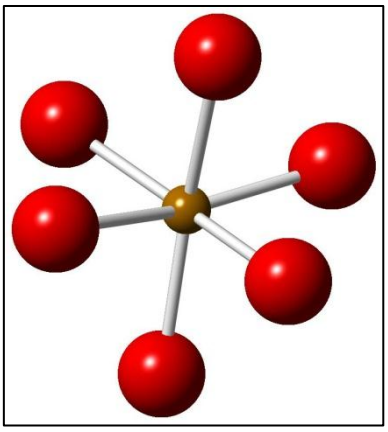

**Figure 8.4 – Hematite unit cell**

**iron structure**

When considering the relevance of this structure, it is useful to compare it to structures that the ClayFF iron parameters are based on. Consider the structure of lepidocrosite (γ-FeOOH) from (Christensen et al. 1982), depicted in Figure 8.5 below.

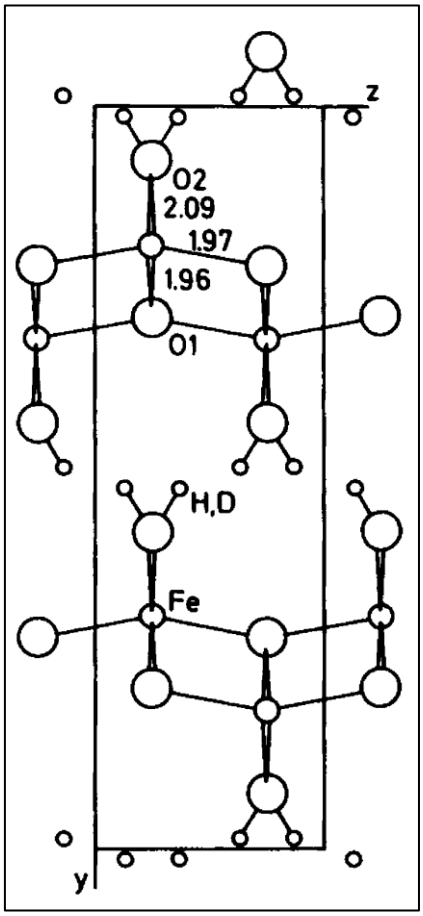


**Figure 8.5 – Octahedral iron structuring in lepidocrosite (γ-FeOOH).**

**Taken from (Christensen et al. 1982)**

From Figure 8.5 it is possible to point out several iron structures surrounded by oxygen atoms. This projection shows only the four oxygen atoms visible in the plane, but the chemical formula proves that it is octahedral. Based on the similarities of the structures, the iron parameters should be a good choice for the simulation.

- The bridging oxygen with double substitution was chosen to parameterize the oxygen in the hematite crystal. Consider the structure surrounding oxygen in the unit cell. The structure can be revealed from the unit cell by using the same approach as for Figure 8.4. The structure around oxygen is depicted in Figure 8.6 below:

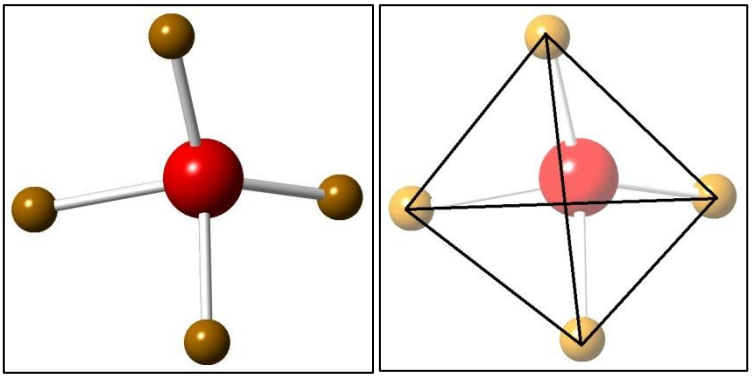

**Figure 8.6 – Left: Hematite unit cell oxygen structure**
**Right: Oxygen structure with pyramid shape drawn**

As seen from Figure 8.6, an oxygen atom in the bulk of hematite is surrounded by four iron atoms, forming a pyramid-like structure. All the surrounding bulk iron is in octahedral arrangement.

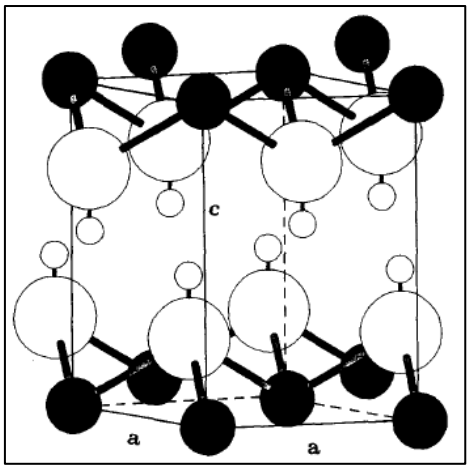


**Figure 8.7 – Structure of brucite ($Mg(OH)_2$).**
**Taken from Catti et al. (1995).**

To properly verify the validity of using these parameters, it is useful to compare Figure 8.6 with some of the structures used as reference for ClayFF. Consider the structure of brucite ($Mg(OH)_2$) in Catti et al. (1995), depicted as Figure 8.7 above. The black circles represent Mg atoms, while the large white circles denote O. The smaller white circles denote H. A similar pyramidal structuring around oxygen atoms can be seen here. The only difference is that instead of being surrounded by four metal atoms, the oxygen is here surrounded by three metal atoms and a hydrogen atom (Catti et al. 1995). Another structure worth comparing with is the structure of diaspore (α-AlO(OH)) in Hill (1979). This structure is depicted in Figure 8.8 below. The same pyramid shape can be seen around the oxygen atom labeled *O2* here. Again the oxygen is surrounded by three metal atoms and a hydrogen atom (Hill 1979).

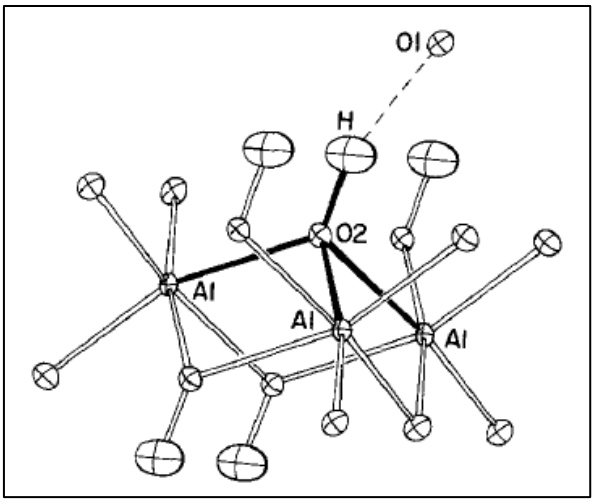


**Figure 8.8 – Structure of diaspore (α-AlO(OH)).**
**Taken from Hill (1979).**

These figures show a similar structure as the one found in the hematite crystal. These parameters should therefore be suitable for the simulation.

### 8.3.3 Force field parameter conversion

To properly use the parameters, they must be converted for use in MD43.

MD43 uses the version of the Lennard-Jones 12-6 potential listed as equation (7.3). The equation for Lennard-Jones in Cygan et al. (2004) differs slightly from this, as shown as equation (8.2) below:

$$E_{VDW} = \sum_{i \neq j} D_{0,ij} \left[ \left( \frac{R_{0,ij}}{r_{ij}} \right)^{12} - 2 \left( \frac{R_{0,ij}}{r_{ij}} \right)^{6} \right] \qquad \textbf{(8.2)}$$

The $R_0$-values must therefore be converted to σ-values, while the $D_0$-values must be converted to ε-values. Since both equation (7.3) and (8.2) must yield the same energy for the same distance, the following relation can be established:

$$V_{LJ}(r) = 4\varepsilon \left[ \left( \frac{\sigma}{r} \right)^{12} - \left( \frac{\sigma}{r} \right)^{6} \right] = D_0 \left[ \left( \frac{R_0}{r} \right)^{12} - 2 \left( \frac{R_0}{r} \right)^{6} \right]$$

By using simple mathematics, it is possible to deduct that:

$$\sigma = \frac{R_0}{\sqrt[6]{2}} \tag{8.3}$$

$$\varepsilon = D_0 \tag{8.4}$$

This conversion makes it possible to obtain the required sigma values, as well as the ε-values. Also, please note that the $D_0$-values must be converted to SI-units (Joule) before they can be used as ε-values.

Table 8.2 gives the MD43-values after conversion:

| Species | **Symbol** | **Charge [e]** | ***ε*** **[kJ/mol]** | ***σ*** **[Å]** |
|---|---|---|---|---|
| **bridging oxygen with double substitution** | obss | -1.2996 | 0.6502 | 3.1655 |
| **octahedral iron** | feo | 1.5750 | $3.7781 \times 10^{5}$ | 4.9062 |

**Table 8.2 – Converted force field parameters**

The data in Table 8.2 were used in MD43 for the simulations.

# 9 The simulation systems

In this work it is necessary to simulate the interactions of $CO_2$ and water, in the presence of both hematite and hydrate. In order to do this, a system containing these elements was planned and built. This section describes this process.

## 9.1 System overview

The hydrate cell was the defining feature of the system, which meant that the x- and y-dimensions of this cell gave the same x and y values to the rest of the system cells. The system was otherwise built along the z-axis, which meant that the different parts were combined to a system along this axis. The hematite in the system was included within a water cell. The final system is shown in Figure 9.1 below.

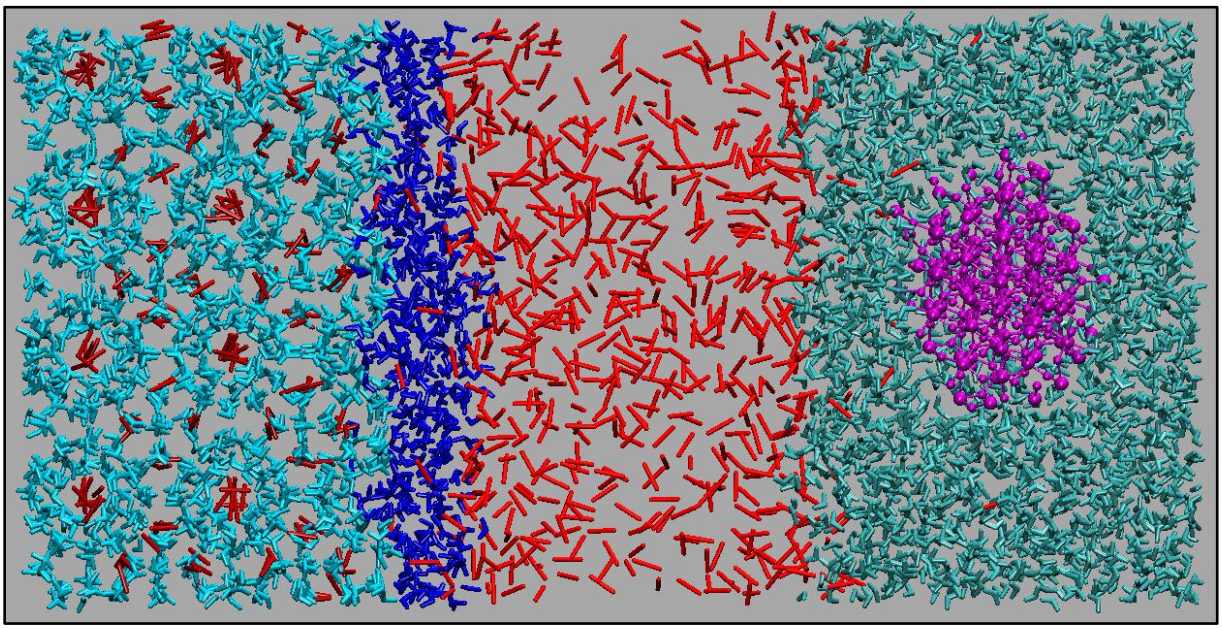

**Figure 9.1 – The combined simulation system. Blue molecules are water, red molecules are $CO_2$, and the hematite crystal is colored magenta**

In this figure, the different system cells have been colored differently, in order to separate them. The hydrate cell is seen on the left, with bright blue water molecules and red $CO_2$ guest molecules. A narrow cell filled with water is located next to the hydrate. It is called Water 2 and is colored a darker blue. In the center of the system, a cell filled with free $CO_2$ gas is located. These molecules are colored bright red. The two remaining system parts is a hematite

crystal and a water cell. The hematite is here colored magenta, and is surrounded by a large water cell called Water 1. This water cell is colored greenish blue.

Note that the system displayed in Figure 9.1 is taken from the TIP4P system after just 0.1595 nanoseconds of simulation. There are therefore some small changes from the initial configuration, such as the $CO_2$ molecules in other cells and the slightly tilted hematite crystal. In order to better display the different system cells, certain molecules were hidden from the figure. The water molecules which obscured the hematite crystal from view were hidden in order to better display the crystal. In addition to this, some of water molecules from Water 1 which were near the hydrate crystal on the left were hidden. This was done to better display the hydrate crystal structure.

The system was periodic in all directions, which meant that the right side of the Water 1 cell was in contact with the left side of the hydrate crystal.

## 9.2 Building the simulation systems

This section will discuss the details of how the different parts of the TIP4P system were built. Details such as the number of molecules in each cell and the tools used to construct the different cells, will be included in this section. The SPC/E and F3C systems were built by simply changing the water model in the original TIP4P system, and are therefore not discussed in this section.

### 9.2.1 Hydrate cell

The hydrate cell was built by Tatiana Kuznetsova. The cell was a $4\ x\ 4\ x\ 2.5$ hydrate block, which had the dimensions of $(48.12\ Å, 48.12\ Å, 30\ Å)$, and contained 1839 water and 192 guest molecules. It was dimensioned based on previous research by Kvamme et al. (2009) (mentioned in section 4.2.1), as each hydrate cavity has a diameter of 12.03 Å. The x- and y-dimension were therefore long enough to include four rows of fully formed hydrate cages $(12.03 \cdot 4 = 48.12)$ in each direction, while the structure in the Z-direction was incomplete on one side. This is illustrated in Figure 9.2 below.

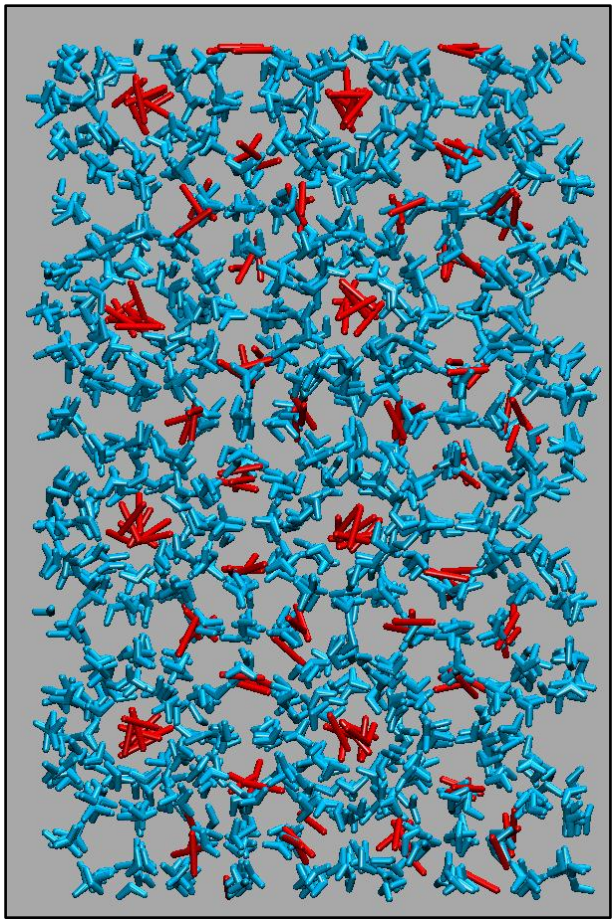

**Figure 9.2 – Hydrate crystal from the simulations**

The figure shows the structure of the hydrate crystal from the X-direction. It is possible to see the water molecules forming the cages around the guest molecules. In this work, the guest molecule is $CO_2$, which means that the hydrate is formed by water and $CO_2$ molecules. Note that in Figure 9.2 the water molecules are colored blue, while the $CO_2$ molecules are red. The special thing about the hydrate water molecules was that they were simulated without the ability to translate, which meant that they could only rotate. This was done to ensure that the hydrate crystal would not be dissolved during the simulation run. The $CO_2$ molecules in hydrate were however free to translate, but these were kept inside the hydrate by the "locked" water molecules.

Note that Figure 9.2 also displays the incomplete hydrate cavities on the right side of the hydrate crystal. This was done intentionally, as a half-formed cage would give free water- and $CO_2$-molecules a chance of completing the hydrate cell structure, which could provide some interesting behavior characteristics to study.

### 9.2.2 Water cells

The system used two different water building blocks of same initial density, one large and one small. They are labeled Water 1 and Water 2, as seen in Figure 9.1. The Water 1 cell had a width of 35 Å, while the Water 2 cell only had a width of 6 Å in the Z-direction. The Water 1 cell contained 2735 molecules, while the Water 2 cell contained 500 molecules.

These cells were created using the same method. First, the widths of both water cells were chosen to provide the necessary data for building them. The width of the Water 1 cell was based upon the fact that it was to contain a hematite crystal, which would rotate around its own mass center with a rotation radius of 12.89 Å. A width of 35 Å was chosen to provide a clearance of 5 Å on each side of the crystal, in order to separate it from the $CO_2$ and hydrate cells. The Water 2 cell was only dimensioned as a 5 Å layer between the $CO_2$ and hydrate cell, with an extra 1 Å as a precaution, as a small amount of the water molecules would enter the hydrate at startup.

From their cell volume, the number of molecules for each cell was calculated. Both of the water cells were then constructed using the MD43 program. The number of molecules was specified within MD43, along with other necessary input, such as the cell dimensions and the NVT ensemble properties. The molecules were then generated on a lattice. The cells now contained the correct number of water molecules, but the molecules were not aligned in a way that resembled a liquid. It was therefore necessary to equilibrate the system. The water cells were simulated further, and after simulating both water cells for a short time (e.g. 10000 steps á $0.5 \cdot 10^{-15}$seconds each), both water cells had liquid configurations. The final water cells can be seen in Figure 9.3. After this, they were ready to be included in the system.

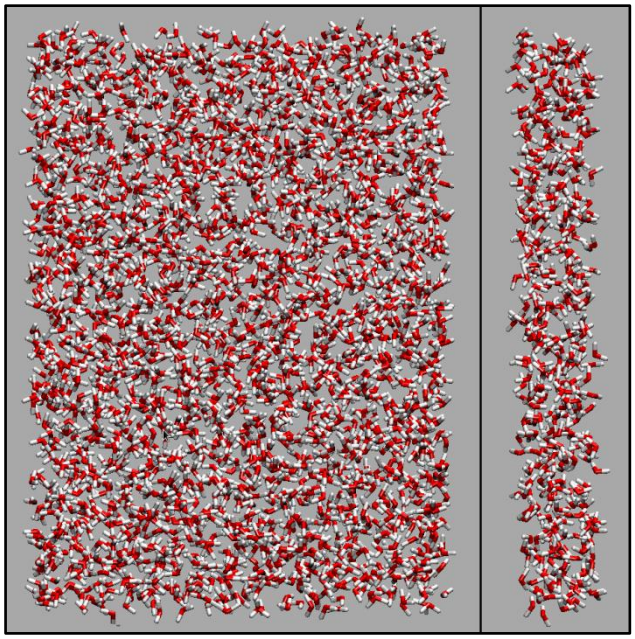

**Figure 9.3 – Water cells of the system, viewed from x.**
**Left: Water 1 cell block**
**Right: Water 2 cell block**

### 9.2.3 $CO_2$ cell

The $CO_2$ cell was built by using the same method as for the water cells. The cell had a width of 30 Å in the Z-direction, which was used to determine the number of molecules in the cell. The $CO_2$ cell contained 634 $CO_2$ molecules. The data was then put into MD43, and provided a data file with the CO2 positioned in a lattice. The molecules were then equilibrated to obtain a gas-like configuration. The final $CO_2$-cell is depicted in Figure 9.4 below:

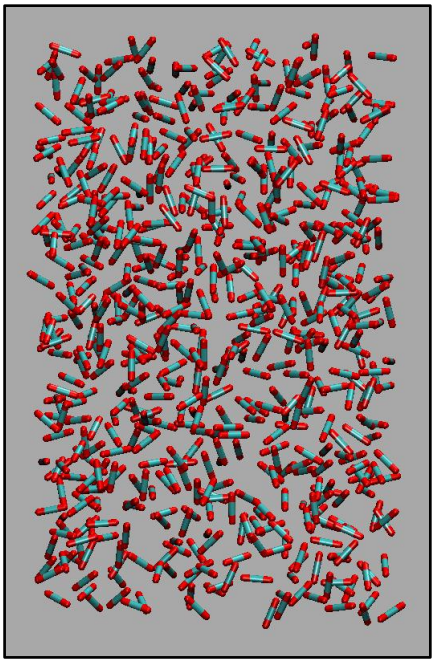

**Figure 9.4 – $CO_2$ cell used in simulation.**

### 9.2.4 Hematite crystal

The hematite crystal was built in the program Crystalmaker using a unit cell configuration for hematite. The unit cell file was found at American Mineralogist Database, and was based upon the work of Blake et al. (1966). The unit cell contained the correct balance of oxygen and iron atoms, in accordance with the chemical formula of hematite, namely $Fe_2O_3$ (Blake et al. 1966). From this unit cell, a larger crystal was built in Crystalmaker, by duplicating the unit cell up to a larger size. The large crystal was then imported into VMD, where it was trimmed down to an appropriate size for the simulation. As discussed in section 4.1, the {0001} surface was cut such as to expose the iron atoms. The iron-terminated surface was chosen as it was the most stable surface when considered on a stand-alone basis, as discussed in de Leeuw and Cooper (2007). The oxygen-terminated surface was described as more stable when hydrated, but this meant that it had to be simulated until an adsorbed water layer was formed on the surface to ensure stability. This was therefore considered too complex for this work (de Leeuw and Cooper 2007).

The hematite crystal also had to be periodic in all directions. Therefore it was vital that the amount of oxygen and iron atoms in the crystal corresponded to the iron/oxygen ratio of 3

oxygen atoms per 2 iron atoms. The trimming of the large hematite crystal was therefore done with the aid of Bjørnar Jensen, who had experience with VMD. By doing this, the hematite crystal used in the simulations was obtained. It is displayed in Figure 9.5 below. The final dimensions were $(10.3\ \text{Å}, 20.922\ \text{Å}, 13.166\ \text{Å})$, and it contained 96 iron and 144 oxygen atoms.

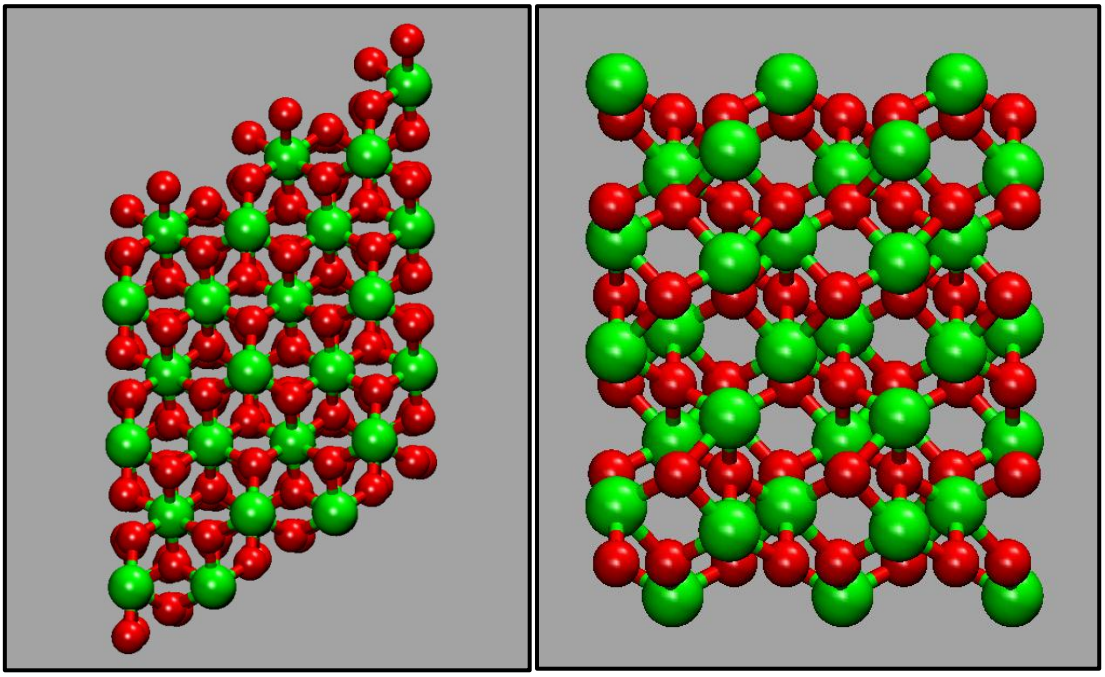

**Figure 9.5 – Hematite crystal from the simulations (Iron atoms are colored green, oxygen atoms are red).**
**On the left: Crystal structure seen from above (Z-direction)**
**On the right: Crystal structure seen from above (Y-direction)**

The purpose of this hematite crystal was to investigate the forces acting between the crystal and the rest of the system. It was to be included within the Water1 cell in order to see what molecules would adsorb on its surface, as well as to investigate whether this small hematite crystal would align itself towards the $CO_2$ cell or the hydrate phase.

The hematite crystal was simulated as a single crystal, with all molecules locked in place. Two test simulations were done in order to investigate the possibility of simulating the crystal with either the iron or oxygen atoms free of such constraints, but the resulting in both cases that in both cases was that the crystal was deformed due to the intermolecular forces both within and outside the crystal. The crystal was therefore simulated as one molecule, which was free to rotate and translate within the system.

### 9.2.5 Combining the system

The system was combined in two stages. First, the hematite crystal and Water 1 cell was combined using VMD and MD43. This was done by first combining the cells in VMD. As a result of this, there were now water molecules within the hematite crystal. The combined cell was therefore taken into VMD, where the water molecules within 2.5 Å of the hematite crystal were trimmed away. This removed the water molecules within the crystal, as well as those closest to the crystal. The resulting cell therefore had a lesser amount of water molecules in it. It also had a lesser volume for the water molecules to move within, as the crystal now occupied part of the volume.

The new system cell contained 2561 water molecules, and a hematite crystal in the center of the cell. The cell was simulated in VMD again to check for problems, and to distribute water molecules back around the hematite crystal. The resulting cell is shown in Figure 9.6.

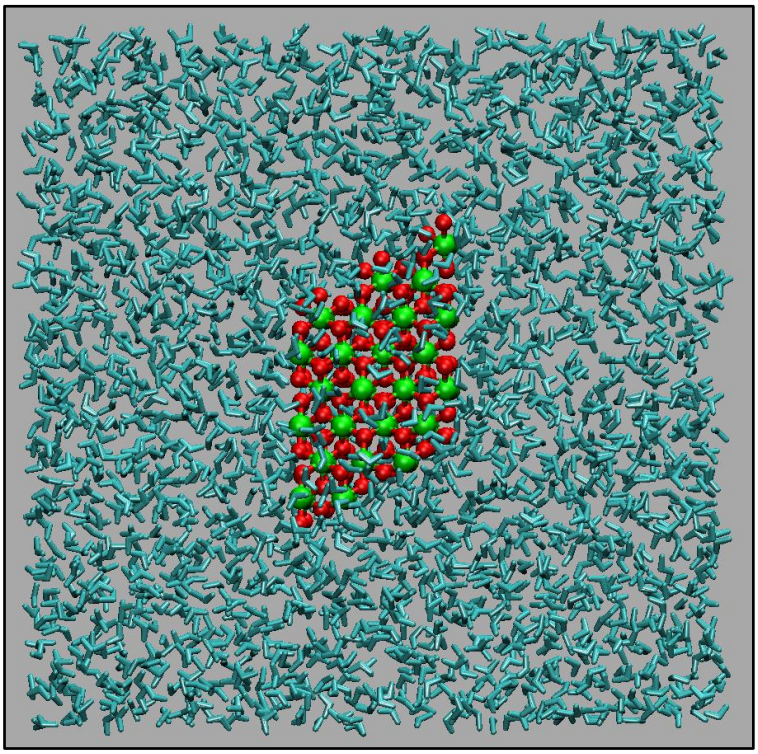

**Figure 9.6 – Hematite crystal combined with the Water 1 cell.**
**The resulting cell is viewed in the Z-direction.**

In this figure, the hematite crystal is visible at the center of the Water 1 cell, surrounded by water molecules, which have been colored blue for the sake of visibility.

The remaining work was to combine all the cells into one system. This was done by Tatiana Kuznetsova. She proceeded to investigate any startup problems with the combined system, before the system was returned to me. This system was the TIP4P system, which has been simulated in the work.

## 9.3 Simulation system startup

It is common for an MD simulation to use a time step of order $10^{-15}$ second, which results in quicker simulation and thus more available simulation data. However, the complexity and strong electrostatic forces in our system made it necessary to use shorter time steps. One reason for this was the concern for system's stability during the equilibration, where potential overlaps or near-overlaps caused by our stacking different building blocks could cause instabilities and crashes. The second reason was that due to high velocities possibly occurring in the system because of the presence of unshielded charges, accurate and reliable integrating of the equations of motion would require sampling by shorter time steps. Therefore, all three systems were started and equilibrated at *dt* of $1.0 \cdot 10^{-16}$ seconds, which was then increased to $5.0 \cdot 10^{-16}$ seconds after simulations reached stability. This time step was considered to be a good tradeoff between simulation length and simulation accuracy.

The first simulation that was initiated in this work used the TIP4P water model. At first the TIP4P system was simulated with a time step length of $1.0 \cdot 10^{-16}$ seconds, but after 170 picoseconds of simulation, the step length was increased to $5.0 \cdot 10^{-16}$ seconds.

As the TIP4P system was up and running, a system using the SPC/E water model was established. It was created using the positions and orientations of the water molecules in the TIP4P system after 125 picoseconds of simulation. After this system had been simulated for 300 picoseconds, the time step was increased to $5.0 \cdot 10^{-16}$ seconds.

Finally, a system using the F3C water model was simulated. The F3C system was created from the SPC/E system after it had been simulated for 300 picoseconds. This system was simulated for 670 picoseconds before it also had its time step increased to $5.0 \cdot 10^{-16}$ seconds.

# 10 Results and discussion

This section describes and discusses the results obtained in this work. Because all of the simulation systems consist of the same system cells, the results are presented by consideration of the different elements in the systems. Notable differences between the systems are included where these are present.

## 10.1 Verification of simulation protocol

In order to validate the results, some extra simulations were conducted. These simulations included two extra simulations of the TIP4P system with different time steps, as well as three simulations of a small system containing $CO_2$ and TIP4P water. The purpose of these simulations was to verify that the use of different time steps for a system did not cause differences in system properties. The results from these investigations will be discussed in the following sections. Another point to consider was whether the simulations of the F3C, SPC/E and TIP4P systems were conducted long enough to obtain reliable results. This will also be discussed in the following sections.

### 10.1.1 TIP4P water + $CO_2$ mixture systems

A system containing only TIP4P water and EPM2 $CO_2$ was set up as a tool for verification of the use of different time steps in the simulation. Although the more complex composite systems might have extra implications of the choice of time step, this system could at least give some indications about how sensitive the systems would be to time step changes. It was also included to produce RDF curves for the water-$CO_2$ structure of a less complex system, which could then be used in comparison with the RDF curves from the main systems. The system itself was built by scaling the Water 1 cell from the main system down to 73.5 % of the original cell. The rectangular primary cell contained 1000 water and 30 $CO_2$ molecules and had the dimensions (35.345 Å, 35.345 Å, 25.704 Å), with periodic boundary conditions in all directions. The number of $CO_2$ molecules in the water phase was chosen to reflect the diffusion ratio described in the work of (da Rocha et al. 2001) plus some more, as the temperature of the system in this work was lower. The system was then equilibrated for 2,500,000 steps, which was more than enough to ensure bulk conditions for both water and

dissolved $CO_2$ molecules. The equilibration was followed by several production runs with varying time steps to examine their possible impact.

The first purpose of the simulations was to verify that the time steps of $0.1 \cdot 10^{-15}$ and $1.0 \cdot 10^{-15}$ provided the same energy values for the interactions. The values of the Lennard-Jones and electrostatic energy were measured for the water-water, $CO_2$-$CO_2$ and water-$CO_2$ interactions. After 18,000,000 time steps of simulation for each system, all the Lennard-Jones and electrostatic values were more than 95 % similar, and it was therefore proven that it is possible to obtain similar results for a simulation at different time steps, even if one simulation is ten times quicker.

The TIP4P water and $CO_2$ gas system was also included for comparative purposes, as such a simple system would take less time to simulate. Because there was no other components than the water and $CO_2$ molecules, any effects from hematite or hydrate on the water/$CO_2$ curves in the main systems would be visible when compared to the RDFs from this system. The RDF curves from this system are included in comparisons with other RDF curves in the following sections.

### 10.1.2 TIP4P system with different time steps

The development of the TIP4P system was investigated by simulating the system at three different time steps. The quickest system had a time step of $5.0 \cdot 10^{-16}$ seconds, and because it was the quickest system, the results obtained at this time step was used in this work. Two other time steps were also simulated for comparison. These simulations used time steps of $0.5 \cdot 10^{-16}$ and $1.0 \cdot 10^{-16}$ seconds. All three time steps were then simulated for 9,000,000 time steps. The data collected from these simulations were then compared just like for the smaller reference system made of TIP4P water and $CO_2$. As these systems were far more complex than the reference system, it was never a goal to prove that these simulations provided the same energies for all the molecular interactions. Instead, this comparison was to illustrate that it was possible to obtain similar data results for some parts of the system that were unlikely to develop differently during the simulation. An example of this was the intermolecular energy values for the Water 1 self interactions. These energies were found to be remarkably similar, as both the electrostatic energy and the Lennard-Jones energy was more than 99 % equal for all the three time steps. The necessary simulation time would have been greatly increased greatly if the goal had been to get equal results for all system parts.

This would not have been possible for all of the system components. For the hematite crystal, for instance, this would have been impossible. This is because the crystal is oriented differently within the system at the system progresses. The equal water phase verifies the use of different time steps in MD simulations.

### 10.1.3 Simulation length

In order to ensure that the simulation results properly reflect the system, it is important to make sure that a simulation run is long enough to properly identify the system behavior. The researchers Mahoney and Jorgensen (2000) believe that a minimum of 3 nanoseconds of simulation is required in order to properly model the system when using the TIP5P model (Mahoney and Jorgensen 2000). Although this work does not use the TIP5P model, this goal was deemed suitable for the simulation of the water models in this work as well. This goal was achieved for all three systems. The SPC/E system was simulated for 9.9 nanoseconds, while the TIP4P system was simulated for 8.3 nanoseconds. The F3C system was simulated for 5.6 nanoseconds. Note that all three systems have been simulated much longer than the goal set for obtaining reliable results, and should therefore reflect the system properties accurately. Another point worth of notice is that the SPC/E system has been simulated longer because it was necessary to investigate a special phenomenon that occurred in this system. This phenomenon is discussed in section 10.3.3.

## 10.2 Density profile for the system

A density profile was created from the final simulations of the F3C system. This density profile was used to study the density distribution of the different molecules across the system. The profile was plotted in MATLAB by using a modified script built by Tatyana Kuznetsova. The script was slightly modified in order to better illustrate the density profile.

The density distribution is shown together with a simulation snapshot in Figure 10.1. The density profile and the simulation snapshot are arranged together to better illustrate the structure in the density profile. Note that although the density profile matches the structure in the snapshot, they are not taken from the same simulation system, as the snapshot is from the TIP4P system. The curves in the density profile represent different atoms and molecules. The yellow curve represents all the free $CO_2$ molecules in the system, while the green and blue

curves represent the free water molecules from Water 1 and Water 2 respectively. The magenta curves represent the hematite crystal. The lighter magenta curve with the large peaks represents the iron atoms, while the darker, smaller curve represents the oxygen atoms. The cyan curve represents the hydrate water, while the red curve represents the trapped $CO_2$ guests in hydrate. The final curve is the black curve, which represents hydrogen in both free water and in hydrate.

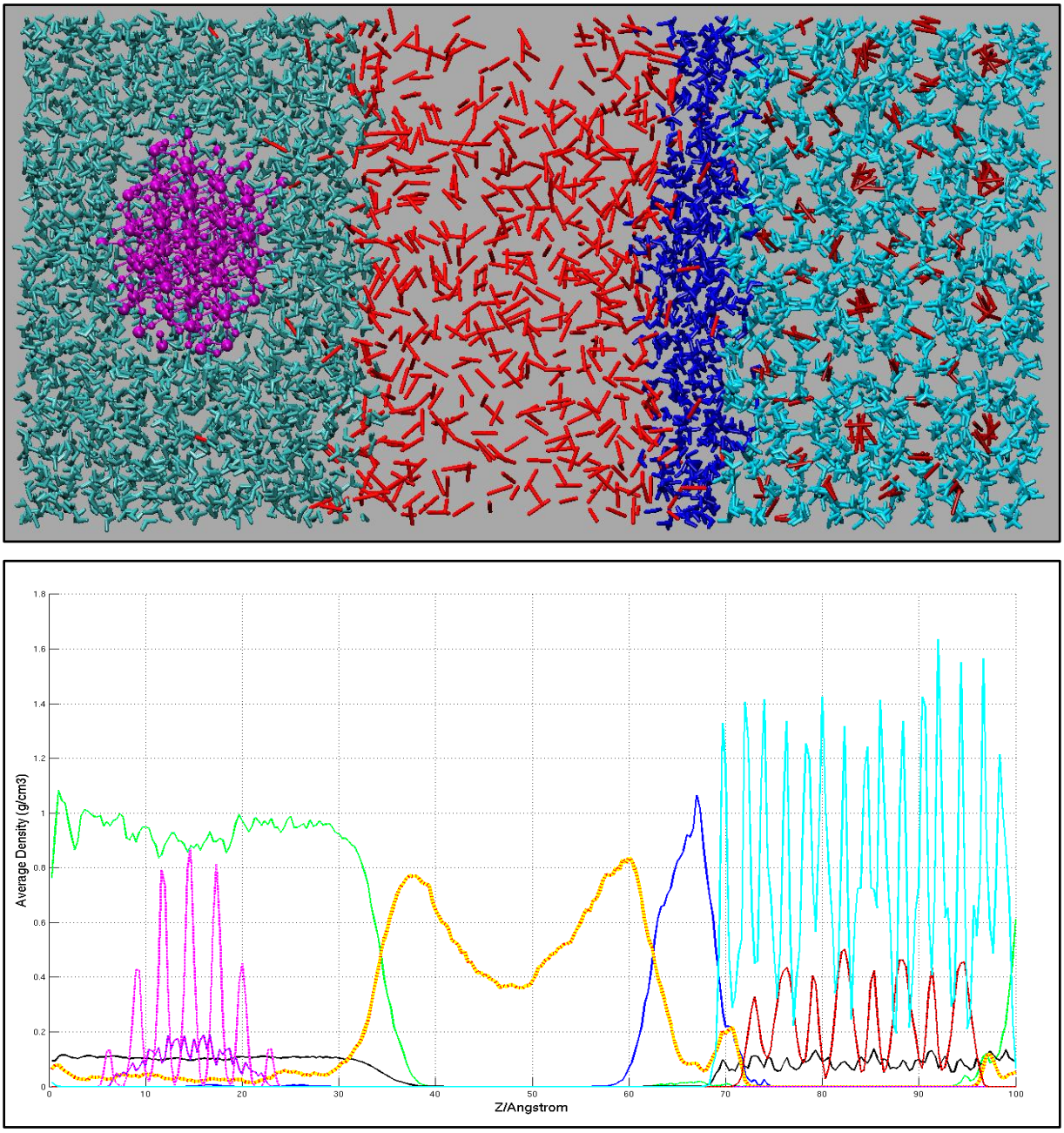


**Figure 10.1 – The density profile of the system shown together with the system.**

The density profile is in good agreement with the structure shown in the snapshot. Both the hematite crystal and the hydrate crystal have a strongly arranged structure. The interfaces between Water 1/$CO_2$/Water 2 are clearly visible. The free $CO_2$ phase in the center clearly dominates the center of the simulation system. A visible trait is that there are two peaks in the $CO_2$ curve. These concentrations of $CO_2$ near the interfaces of water match those observed in da Rocha et al. (2000), and indicate that the $CO_2$ phase acts as it should near a water phase. No such peaks are formed on the water curves near the interface, which suggests that the inclusion of hematite and hydrate in the system has some effect on the water phases.

The blue Water 2 curve is of special interest, as this water phase has a strong peak value and no apparent bulk structure, like the one that can be seen from the Water 1 curve. This indicates that the Water 2 phase is strongly affected by the hydrate crystal, forming a crystal-like structure. The yellow and black curves have also been affected by hydrate. In order to better study these curves, consider Figure 10.2 below.

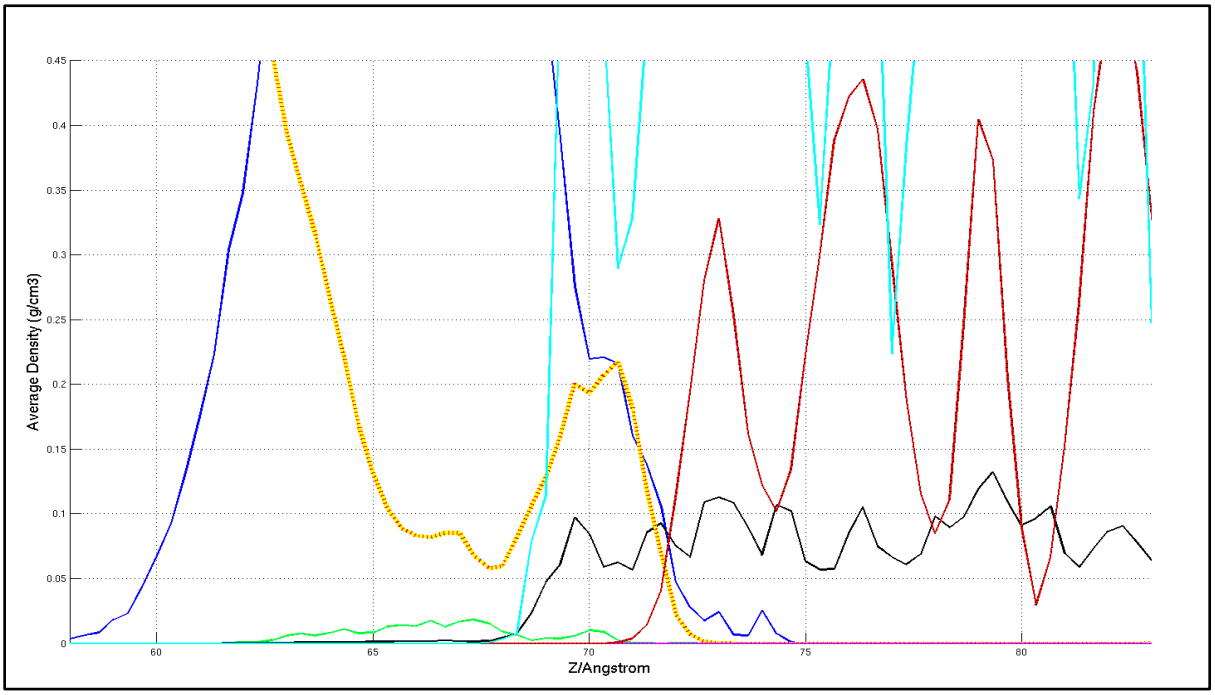


**Figure 10.2 – Close up of density profile near hydrate.**

This figure shows a close up of Figure 10.1. The hydrogen structure, shown by the black curve, is clearly more structured in hydrate than in the rest of the system. A clear pattern of peaks is observable in the curve, while the curve is much flatter in the Water 1 bulk phase.

The free $CO_2$ molecules are also affected in the presence of the hydrate cell. This can be seen very clearly from the yellow curve in Figure 10.2. The yellow peak in the center of the figure indicates the nearest free $CO_2$ molecules have become a part of the hydrate structure. This crystal-like structure indicates that these $CO_2$ molecules act as guest molecules trapped in hydrate. This will be verified in the next section.

## 10.3 Hydrate structure

The hydrate crystal was the defining cell of the system, due to its size. It was also, as discussed in earlier sections, one of the most important parts of the system. The interactions between this crystal and the rest of the system provided some interesting results, which are described in this section.

### 10.3.1 Guest molecules in the "open" hydrate cavities

The half open hydrate cavities were, as mentioned earlier in section 9.2.1, built half open in order to observe how other molecules would interact with an incomplete hydrate structure. At the start of the simulations, the first noticeable fact was that the water molecules from the Water 2 cell completed the hydrate lattice structures, both by entering the cavities, and by forming the remaining lattice half. These halves were not as stable as the locked hydrate lattice, but were kept in place by hydrogen bonds. The structure was strengthened further by the presence of the water molecules inside the cavities, which acted as guest molecules. As the simulations progressed, the water molecules inside the cavities were gradually replaced by $CO_2$ molecules from the free $CO_2$ cell. The picture on the left in Figure 10.3 is a snapshot from the F3C simulation system that illustrates how the hydrate cavities can be filled with both $CO_2$ and water molecules. The picture on the right shows the hydrogen bonds in the Water 1 cell, and is included to illustrate the hydrogen bonding differences between hydrate and bulk water. Both snapshots are viewed from the X-direction.

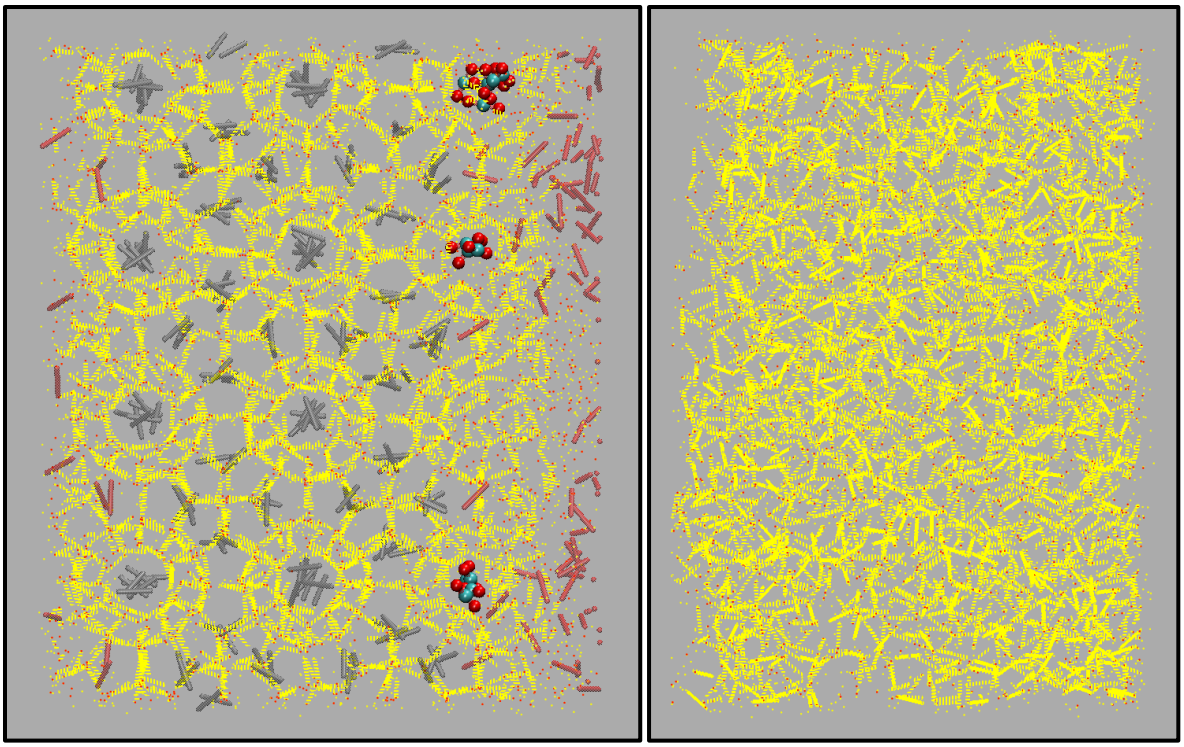

**Figure 10.3 - Structure differences between the hydrate cell and the Water 1 cell.**
**Left: $CO_2$ molecules entering hydrate as guests.**
**Right: Hydrogen bond structure in Water 1 cell.**

In the figure to the left, three of the cavities on the right are filled up with $CO_2$ molecules, while the last one is filled with water molecules. The red molecules on the right and left are other $CO_2$ molecules from the free gas phase. The gray molecules are $CO_2$ originally trapped within the hydrate crystal (shown by the yellow hydrogen bonds). The red and yellow dots illustrate the water atoms both in and around the hydrate. The figure to the right shows the hydrogen bonding in a bulk water phase (Water 1). The same red and yellow dots are used to indicate water molecules. Note that all $CO_2$ molecules and the hematite crystal in the Water 1 cell were hidden from view.

The number of $CO_2$ within these cavities slowly increased, although a few $CO_2$ left the cavities and returned to the free gas phase at times. This behavior continued right until the end of the simulations. In order to compare the different systems, eight samples were taken from each of the simulation systems. The resulting averages show that the cavities in the F3C system contained an average of 11 $CO_2$ molecules, while the TIP4P system contained an

average of 10 $CO_2$. The SPC/E system had the lowest average of 8 $CO_2$ in the cavities. These results seem to indicate that the exchange of $CO_2$ molecules between the open hydrate cavities and the free $CO_2$ phase had reached a stable state for the F3C and TIP4P systems. The SPC/E had a series of low sample values, with a minimum value of 4 $CO_2$ in the cavities. This indicates that a fluctuation in the SPC/E system occurred during these simulations, and makes it harder to prove stability here.

The structuring effects between hydrate and the surroundings were investigated by calculating various pair correlation functions for hydrate and free water, as well as for hydrate and free $CO_2$. Figure 10.4 shows the RDF curves estimated for the hydrate water oxygen structure in the TIP4P system.

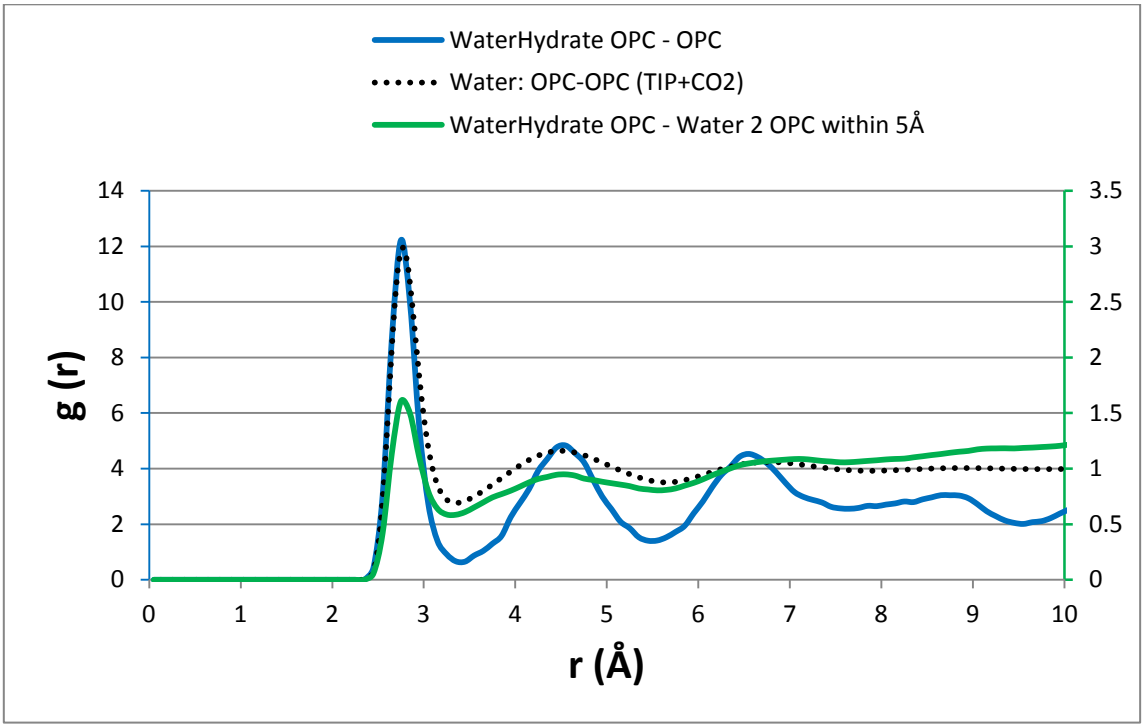


**Figure 10.4 - RDF curves for comparison with hydrate. The blue curve shows the oxygen - oxygen interactions for hydrate, while the green curve shows the hydrate oxygen interactions with Water 2 oxygen atoms. The dotted black line is the water O-O interactions taken from the TIP4P + $CO_2$ reference system.**

Figure 10.4 contains three RDF curves. The blue curve illustrates the hydrates own oxygen – oxygen structure, while the green curve shows the interactions between oxygen in hydrate and all oxygen in the Water 2 phase that are within 5 Å of the hydrate crystal. The dotted black

curve is the oxygen - oxygen for pure water, which is taken from the TIP4P + $CO_2$ reference system. Note that the hydrate curve uses the **g(r)**-axis on the left, while the two other curves use the **g(r)**-axis on the right. The blue hydrate curve has a perfect structure because the molecules cannot translate in the simulations. This was also the case in the SPC/E and F3C system. These curves are therefore not included.

From the figure it is possible to see that the first peak is in the exact same location for all three curves. The next peak is also located on the same distance for the hydrate and Water 2 curves, while the peak in the reference curve is only shifted by about ~0.05 Å. The third peak is hard to compare, as the Water 2 curve is tilted and flat. It does appear to be shifted ~0.3 Å when compared to the reference curve. Note that the peaks of the Water 2 and reference curve are flatter after the first peak, which is to be expected, as the water molecules are still liquids, while the hydrate molecules are locked in a crystal configuration.

All in all, the hydrate oxygen – oxygen interactions seem to have a good structure when compared to the water-hydrate and pure water structure, especially for the two first peaks. The third peak seems to be shifted when compared with the reference system. The hydrate oxygen – hydrogen structure was also investigated. This structure is illustrated in Figure B.1, and is discussed in Appendix B.

It was also interesting to investigate the structure formed by hydrate and $CO_2$. The RDF curves for the TIP4P system structure between hydrate oxygen and carbon $CO_2$ are shown in Figure 10.5 below:

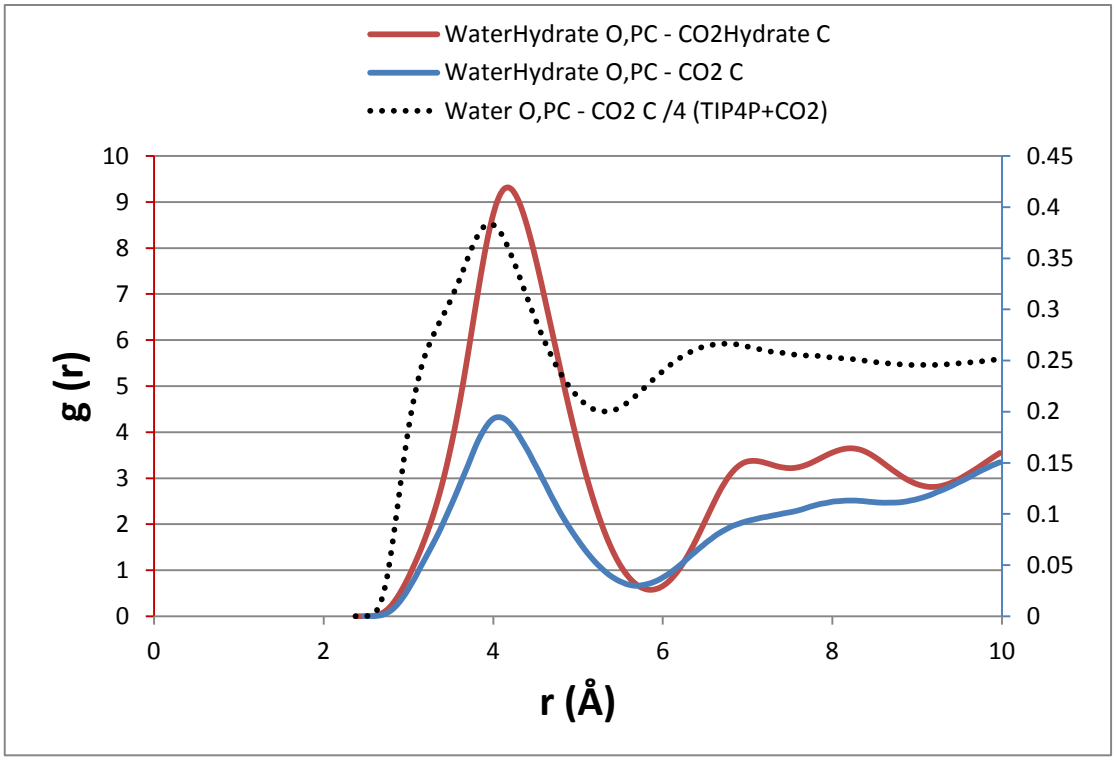


**Figure 10.5 – RDF curve comparison in case of hydrate oxygen and adsorbed (blue) and encaged guest carbon atoms (red). The water oxygen – CO2 carbon curve (dotted black) is from the reference system. The red curve uses the axis on the left, while the two other curves us the axis on the right.**

The figure displays two different RDF curves for the hydrate oxygen – carbon $CO_2$ interactions from the TIP4P system, as well as a curve from the reference system containing TIP4P water and $CO_2$. The red curve shows the strong correlation between hydrate $CO_2$ guest molecules encaged in hydrate and hydrate oxygens, while the blue curve displays the structuring of free $CO_2$ molecules adsorbed by the partial cages on the Water 2 side of the hydrate. All the free $CO_2$ was included in the calculations, thus resulting in the drastically lower RDF values due to a higher normalization factor. The red curve structure is practically identical for the SPC/E and F3C system, and these have therefore not been included.

The structural similarities between the red and blue curves are obvious, with the peaks on the free $CO_2$ curve shifted to the left by less than 0.1 Å. This indicates that the adsorbed $CO_2$ molecules adsorbed in the hydrate act as guests within the cavities, replicating the structure of hydrate. When these curves are compared to the oxygen – carbon structure of water and $CO_2$ in the reference system, the structure appears to be shifted by ~1-1.5 Å. The first peak structure has two peaks, while there is only one on the hydrate structures. This shows that the structure in pure water and $CO_2$ is closer than the structure in hydrate water and $CO_2$. The structure is also different for the next two peaks, as the amplitude is higher for the second

peak in the reference system. All in all this shows that $CO_2$ has a different structure near hydrate water than it has with pure water. Note that in order to properly compare the structure, the black curve was scaled down four times.

### 10.3.2 $CO_2$ guest structure on the opposite side of hydrate

Another interesting structuring effect occurred further into the simulation, as $CO_2$ was diffused into the Water 1 cell. After being diffused into the water cell for a significant part of the simulation, the $CO_2$ reached the other side of the water cell, and were pulled towards the hydrate crystal. The $CO_2$ molecules seemed to align themselves in different depths of the hydrate. After investigating this further, it was revealed that the $CO_2$ positioned themselves as guests for different cavities, which could be observed by orientating the system in the Y- and Z-direction. This is illustrated in Figure 10.6. The figure shows the hydrate crystal from two angles. In each view, a group of $CO_2$ molecules can be observed to have taken up positions as to fill new hydrate cavities. The image on the left displays a group of green $CO_2$ molecules, which can be seen within the open cavities when the crystal is viewed from the Y-direction. The image on the right displays a group of blue $CO_2$ molecules. Their placement within cavities can be seen when looking at the crystal from the Z-direction. The hydrate crystal itself is shown by the yellow hydrogen bonds between water molecules, which are indicated by the small red and yellow dots in the figure. Note that the $CO_2$ molecules trapped inside the other cavities have been hidden from the figure in order to better display the observations.

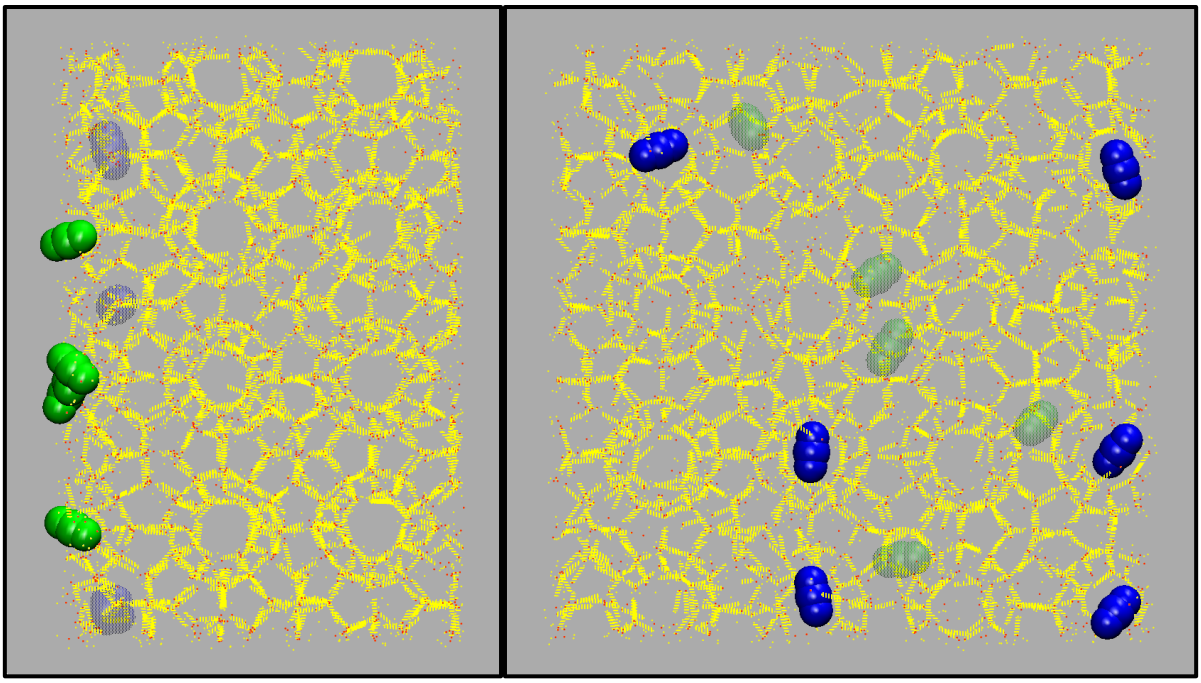

**Figure 10.6 – CO2 structuring on the opposite side of the hydrate crystal.**
**Left: CO2 molecules (green) with visible structure from the Y-direction.**
**Right: CO2 molecules (blue) with visible structure from the Z-direction.**

The number of $CO_2$ molecules was measured in each system. At the end of the simulations, the F3C system had 11 $CO_2$ molecules structured on the opposite side of hydrate, while the TIP4P system had 11 $CO_2$ molecules. The SPC/E system had only 9 $CO_2$ molecules at the end. There was however, another notable property to investigate. As done in section 10.3.1, a number of samples were taken from each of the simulations. This revealed that although SPC/E had the lowest number of $CO_2$ molecules at the end of the simulation, the number of $CO_2$ molecules had steadily grown during the simulation. The TIP4P system also displayed a stable growth, while the F3C system gained and lost $CO_2$ rapidly, showing the strongest fluctuations in sample results of all three systems. This could mean that although both TIP4P and F3C had the best structuring of $CO_2$ on this hydrate cell surface, the F3C system might not have a very good hold on the $CO_2$ molecules. In summary, it is possible to indicate that the TIP4P system had both a stable structure and a high number of $CO_2$ molecules in the cavities. The F3C system had many $CO_2$ molecules in the cavities, but did not seem to have a good hold on them, which could suggest poor structure. The SPC/E system had a stable structure, but had fewer $CO_2$ within the cavities.

### 10.3.3 A rare event

After ~6.5 nanoseconds of simulation, a rare event occurred within the SPC/E system. A single $CO_2$ guest molecule from the original $CO_2$ guest phase was able to break through the locked hydrate water molecules, and escape over to the free $CO_2$ phase.

This phenomenon was very unlikely to occur, as the hydrate water molecules could not translate in this work. They did however rotate, which would mean that there were brief moments where a suitable gap could have been formed between the water molecules, making it possible for the $CO_2$ molecule to escape through. This did however require a very precise timing and orientation for the $CO_2$ molecule. This event can be investigated by studying Figure 10.7 on page 92, which shows the system behavior during the phenomenon.

The figure shows six snapshots from the SPC/E system. As seen from the figure, the $CO_2$ guest molecule (enlarged and colored blue with VMD) initially struggles to break through the hydrate lattice (yellow). It makes several attempts to break through, aligning itself horizontally. Suddenly, the $CO_2$ molecule slips through the lattice and enters the water layer on the surface of hydrate. It crosses this layer and becomes a part of the free $CO_2$ gas phase.

There appears to be a strong pull on the $CO_2$ molecule. This is reflected by the orientation of the free $CO_2$ molecules near the cavity. These molecules seem to have rotated into a vertical orientation in order to pull the $CO_2$ free from the hydrate. By doing so, their oxygen center molecules can favorably attract the carbon of the imprisoned $CO_2$ molecule.

After this event, the $CO_2$ molecule joined the free $CO_2$ gas phase, and has been observed to behave just as any other free $CO_2$ molecule. The system was simulated for another 2.7 nanoseconds after this event, but no $CO_2$ molecules were able to enter the hydrate cavity. None of the other $CO_2$ guest molecules were able to escape the hydrate. This suggests that the hydrate cavity is rarely open for guest molecules to escape, which makes this phenomenon a rare event in MD simulations.

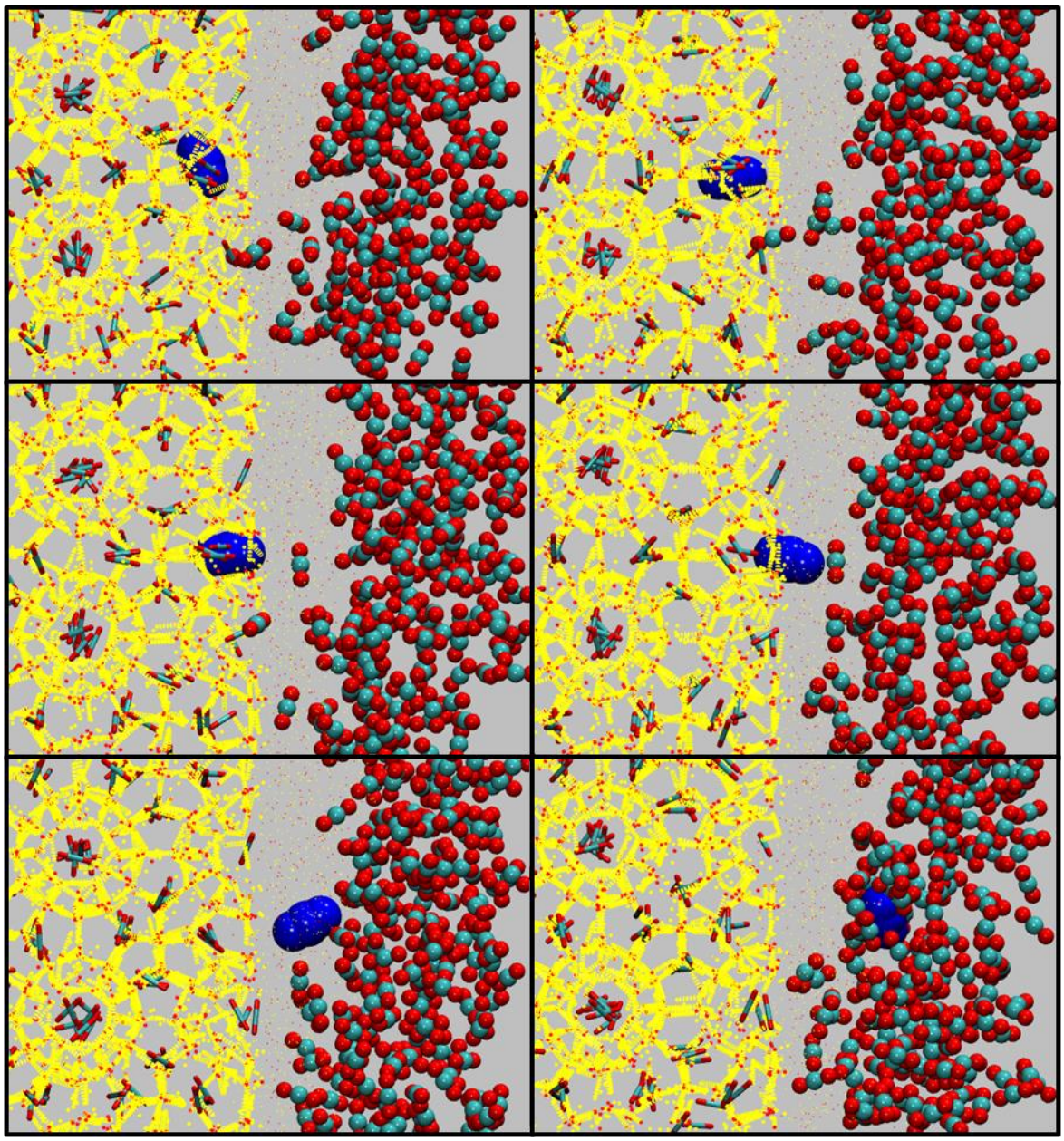

**Figure 10.7 – The escape of a $CO_2$ molecule (blue) from the hydrate cell (yellow).**

This event can be considered from a thermodynamic viewpoint as well. The chemical potential for the escaping guest molecule in hydrate is at equilibrium the same as that of a free $CO_2$ in the gas phase. This does however only apply when the guest is surrounded by the lattice structure of bulk hydrate. The escaping guest is not found in the bulk of hydrate, but in the outer layers of hydrate. The molecule is therefore surrounded by very different structures on either side. On the left, the hydrate cell is very organized, forming a strong, stable barrier. On the right however, this strong structure is not present. Instead, there is a water phase and a $CO_2$ gas phase. These phases are not in equilibrium with the escaping $CO_2$ guest, and act like a

vacuum on it. The opportunity presents itself when the surface layer of hydrate forms a temporary opening, allowing the $CO_2$ molecule to escape through.

## 10.4 Hematite structure

The hematite crystal was another important system feature of this work. Much information could be obtained by examining the interactions between hematite and the rest of the system. This section describes some of these results.

### 10.4.1 Water adsorption on hematite:

One of the first phenomena that occurred in the simulations was that the surrounding water molecules adsorbed on the surface of the hematite crystal. This structure is illustrated in Figure 10.8, which was taken from the SPC/E system.

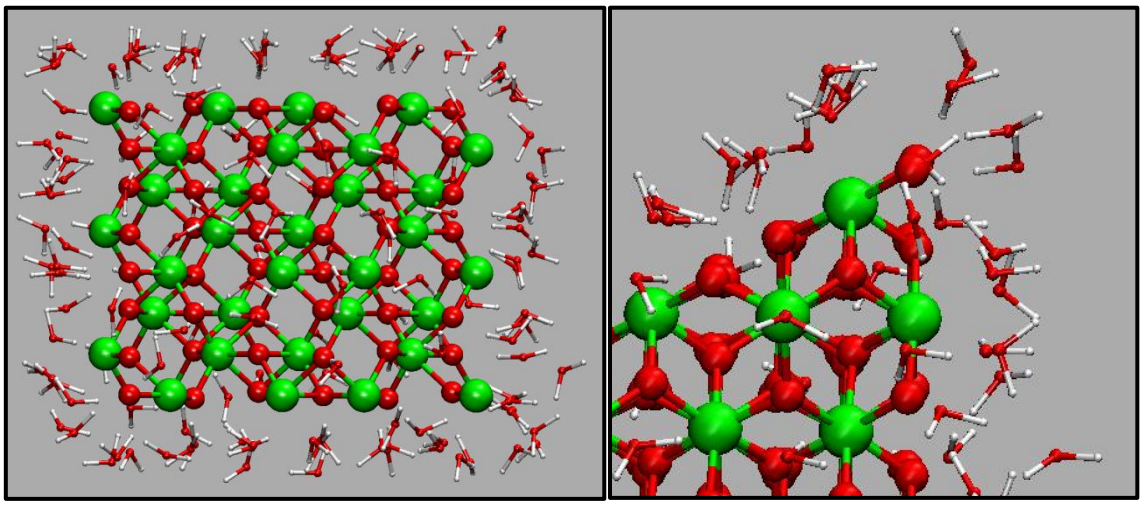

**Figure 10.8 – Water molecules surrounding the hematite crystal.**
**Left: The closest water layer surrounding hematite. Note the water molecule orientation.**
**Right: Part of the crystal and the surround water orientation, viewed from the Z-direction.**

The figure on the left side of Figure 10.8 shows the closest water layer absorbed around the hematite crystal. The water molecules have a clear structure around the crystal. The most notable feature of this layer is the close proximity of the hydrogen atoms. Consider the picture on the left. Most of the water molecules align themselves with their hydrogen atoms pointing towards the hematite crystal oxygen. This is especially visible on the left side of the crystal,

where the water atoms point their hydrogen atoms directly at the oxygen atoms in hematite. Another notable feature is displayed by the picture on the right in Figure 10.8. Many of the water molecules also have their oxygen atoms pointing towards the iron atoms in hematite. With two water atoms pointing towards fixed and periodically positions, the other hydrogen atom appears to be aligned as well. Based on these observations, it should be safe to assume that these water atoms have formed an adsorbed layer on the hematite surface. A secondary adsorbed layer was also seen in VMD, albeit this layer was not as visibly structured as the first.

The adsorption effects were investigated in more detail by calculating various pair correlation functions for hematite – Water 1 interactions. Figure 10.9 illustrates the hematite oxygen - Water 1 hydrogen structure effects for all three systems.

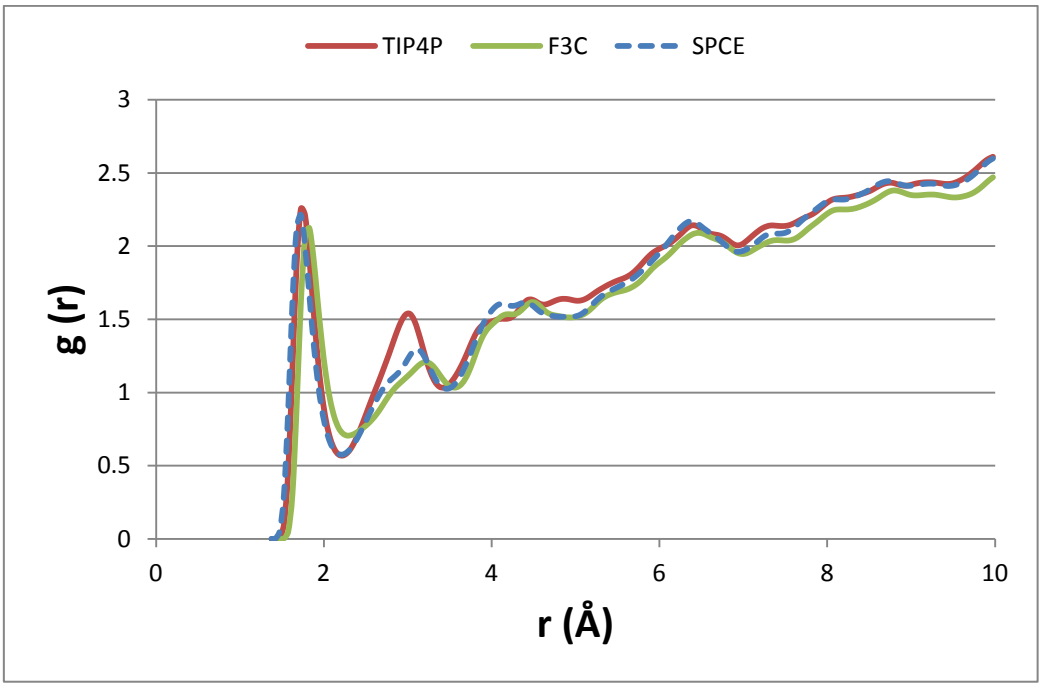


**Figure 10.9 – System comparison of the hematite oxygen - Water 1 hydrogen RDF curves.**

The RDF curves for all systems indicate that the first adsorbed water layer starts at the distance of 1.7 Å and corresponds to hydrogen atoms obvious in Figure 10.8. The relative height of the second peak differs somewhat from system to system. The highest peak was found in the TIP4P system, with the two other systems exhibiting lower peaks. The second peak lay at 3 Å in all the systems; our measurements showed that this distance matched the

position of the other hydrogen atom in first adsorbed layer. The second adsorbed layer could not be identified from these RDF curves due to the strong influence of the hematite crystalline structure. Further investigations of the adsorbed structure were therefore conducted in the SPC/E system, and the results are shown in Figure 10.10.

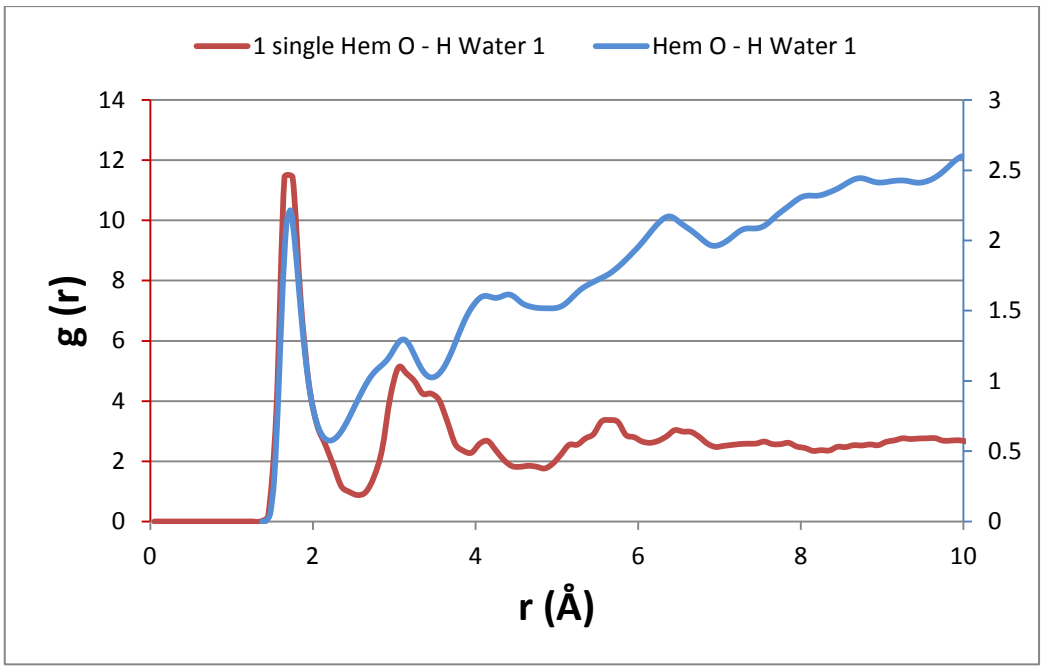


**Figure 10.10 – Closer inspection of the Hem O - H Water 1 structure. The blue curve shows the structure of SPC/E from Figure 10.9. The red curve shows the structure of hydrogen near a single oxygen atom in hematite, making it easier to observe the true structure**

Figure 10.10 shows the hematite oxygen - Water 1 hydrogen structure for the SPC/E system. The blue curve is the SPC/E curve from Figure 10.9, while the red curve is the structure of Water 1 hydrogen found around a single oxygen atom in hematite. Note that the blue curve uses the axis on the right, while the red curve uses the axis on the left.

As expected, both curves are in perfect alignment for the first peak, since it shows the preferred closest position of water hydrogen with respect to hematite oxygen. The structure of the second peak clearly differs depending on whether one includes *all* oxygen atoms or just a single one. As noted previously, the second layer did not show a strong structure, so it was investigated further by means of VMD. For the single oxygen molecule in hematite, the secondary layer was estimated to be located between 4.1 to 5.2 Å. Two small peaks can be seen in Figure 10.10 at these positions, but they are much less pronounced, indicating that this layer is less structured than the tightly ordered first layer. However, as the behavior of $CO_2$

discussed in the next section suggests, this layer must be strong enough to repel $CO_2$ within ~6 Å of hematite.

After considering the structural properties of Water 1 hydrogen and hematite oxygen, the pair correlation functions for Water 1 oxygen and hematite iron was estimated. These curves are illustrated in Figure B.2, which is included in Appendix B.

The number of water molecules surrounding the hematite crystal was also investigated for each system. From the last 1500 simulation frames for each system an average value was calculated. The averages are based upon 11 values that were taken from all water molecules which had at least one atom within 2 Å of the hematite crystal. The results show that the SPC/E system had the largest average, with 86 water molecules near the hematite surface, while the second largest number was that of the TIP4P system, with 83 molecules near hydrate. The F3C system had the lowest number of water molecules near hydrate, with only 76 water molecules near hydrate.

Finally, the hydrogen bonds between water and hematite were studied. The hydrogen bonds were found to be formed between the hydrogen atoms in water and oxygen in hematite. To determine the number of hydrogen bonds in each system, 11 average values were taken for each system. All water molecules with hydrogen bonds within 3 Å were measured. The SPC/E system had the most hydrogen bonds, with an average of 45 hydrogen bonds between water and hematite. The F3C system had an average of 43 bonds, while the TIP4P had the lowest average of 38 bonds.

### 10.4.2 $CO_2$ interactions with hematite

The behavior of $CO_2$ near the hematite crystal was also investigated. After observing the simulations for some time, it became apparent that there was a competition between water and $CO_2$ near the hematite crystal surface. Because of the adsorbed water layer on the hematite surface, the $CO_2$ molecules are prevented from approaching the crystal. The nearest $CO_2$ molecules diffused in the Water 1 cell have been repeatedly observed to move closer to the hematite surface, only to be pushed back into the water bulk phase by the adsorbed layer. Because of this, the $CO_2$ molecules are rarely closer to the hematite than 7.5 Å, although they

have been observed to get as close as ~5 Å when attempting to move towards the hematite. Because of this repulsive water layer, there is no visible $CO_2$ – hematite structure. This is verified in the RDF curves for hematite – $CO_2$, which display no visible structure. The RDF for iron in hematite and oxygen in $CO_2$ is included in Appendix B and can be seen in Figure B.3.

### 10.4.3 Crystal orientation within the Water 1 cell

The orientation of the hematite crystal within the Water 1 cell was monitored in all three simulation runs, in order to detect whether a final, preferred orientation of a hematite crystal surface towards either hydrate or the $CO_2$ cell could be detected. A permanent orientation of any surfaces was however not possible to prove in any of the systems, as the hematite crystal translated and rotated too much to prove any permanent orientation. Some interesting instructive tendencies were observed, as both of the 3-point models had the hematite crystal translate and rotate nearer to the hematite cell than the $CO_2$ cell, while the 4-point TIP4P model had the hematite crystal moving near the $CO_2$ cell. For both of the 3-point models, hematite was observed to orient itself with a corner of the crystal pointing towards hematite. The distance between the hematite crystal and hydrate in this orientation was observed to be ~7 Å for the SPC/E system, while the F3C system could be observed to be within ~6 Å. The TIP4P system has been observed within ~9 Å of the $CO_2$ phase. Still, these orientations are not maintained throughout the simulations, and can therefore not be considered permanent.

### 10.4.4 Crystal influence on the diffusion of CO2 into Water 1

The attraction of $CO_2$ towards hematite seems to be an additional driving force for the diffusion of $CO_2$ into the bulk of the Water 1 cell. Because $CO_2$ molecules from the free $CO_2$ phase struggle to move closer to the hematite crystal, it appears that some get stuck within the water phase, thus accelerating the diffusion process.

Another interesting result was revealed in the simulation of TIP4P with the smallest time step. A single $CO_2$-molecule was observed to get all the way across the Water 1 cell in a single simulation run, aided by the combined push/pull from hematite and the adsorbed water layer. This result gave this system a single $CO_2$ molecule on the Water 1/hydrate interface, long

before any mentionable diffusion had occurred in the Water 1 cell. This also indicates that hematite can accelerate the diffusion of $CO_2$ into a water bulk phase.

## 10.5 Other properties of the free molecules

The properties of both the free water molecules and the free $CO_2$ molecules have been investigated in relation to the two crystal structures. There are however a few noteworthy properties for these molecules left to discuss.

### 10.5.1 Water 1 pair correlation for all three systems

The pair correlation functions of the Water 1 cell were investigated for all three systems. Since this was the largest block of free molecules, which both contained a hematite crystal and many dissolved $CO_2$ molecules. The resulting RDF curves revealed some deviations in the structure for two of the water models. These results are presented in Figure 10.11 and Figure 10.12.

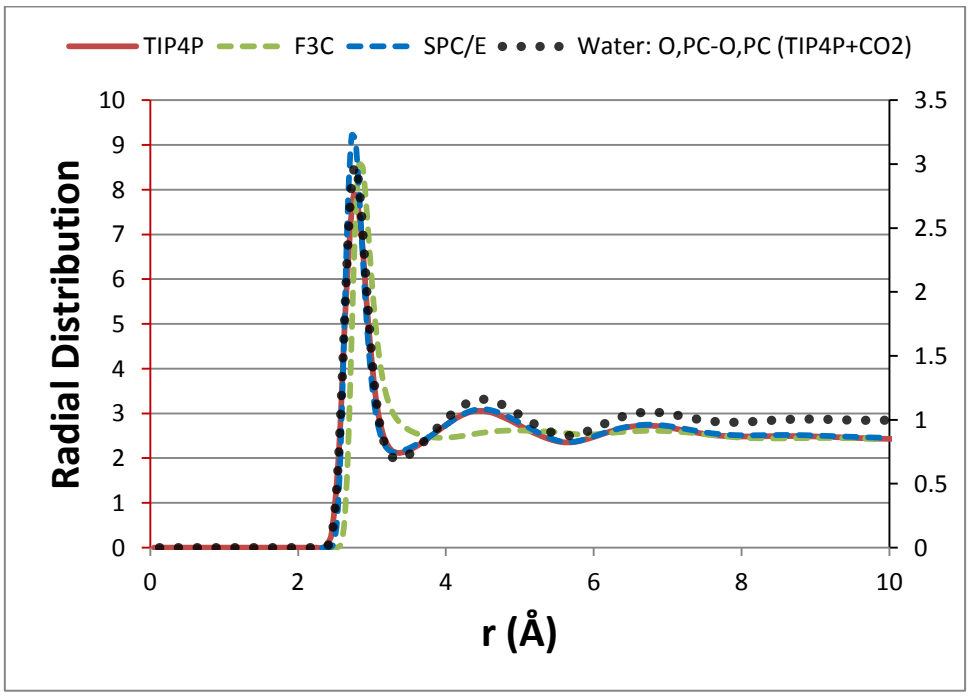


**Figure 10.11 – Water 1 oxygen – oxygen structure for the three main systems and the reference system (TIP4P+$CO_2$)**

Figure 10.11 shows the Water 1 oxygen – oxygen structure for the TIP4P, F3C and SPC/E system, as well as the oxygen – oxygen structure from the reference system. Note that the reference system curve uses the axis on the right. The most notable feature of these RDF curves is that TIP4P, SPC/E and the reference system have a nearly identical structure, while the F3C system curve is shifted by about 0.1 Å. The biggest difference is the weak second and third peak structure of F3C. This could indicate that the F3C water model does not yield good oxygen – oxygen structure when kept rigid in simulations, or it could mean that F3C water structure was affected by other molecules in or near the Water 1 phase.

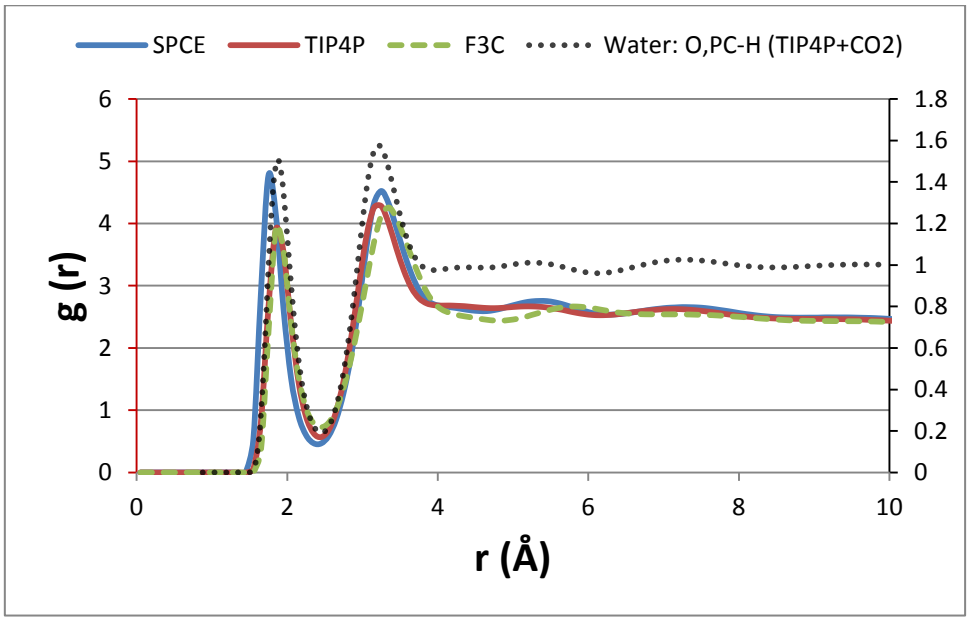


**Figure 10.12 - Water 1 oxygen – hydrogen structure for SPC/E, TIP4P, F3C and the reference system (TIP4P+$CO_2$)**

Figure 10.12 shows the Water 1 oxygen – hydrogen structure for the three main systems, as well as the reference system´s structure. The reference system uses the axis on the right. The TIP4P and F3C system structure is in good agreement with that found in the reference system for both the first and second peak. The SPC/E curve is shifted both in distance and amplitude. The first peak is shifted 0.2 Å, while the second peak is at the correct distance. However, since the amplitude of the first peak relative to the second peak is the opposite of all the other systems, this means that the oxygen – hydrogen structure for SPC/E deviates from structure in the reference system. As the SPC/E model is a simple and well documented model, this indicates that the SPC/E structure has been affected by other molecules.

### 10.5.2 CO2/Water 1 interface

The $CO_2$/Water 1 interface was studied during the simulations. The interface thickness appears to be ~6 Å for all systems. A snapshot of the $CO_2$/Water 1 interface from the SPC/E simulation is shown in Figure 10.13 below.

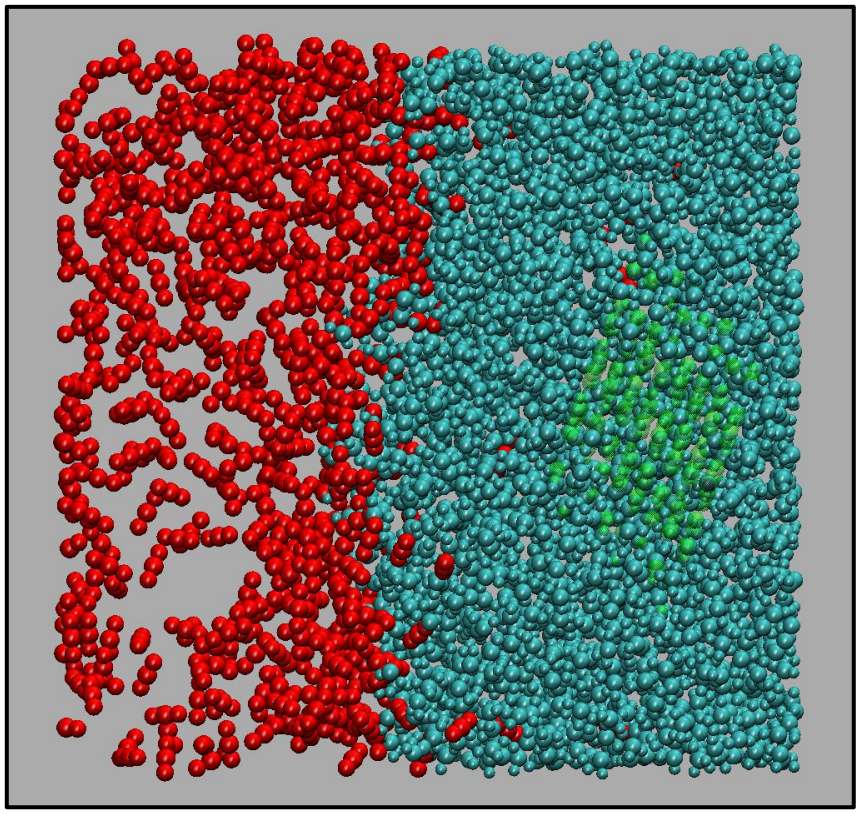

**Figure 10.13 – The $CO_2$ / Water 1 interface. The red molecules are $CO_2$, the blue molecules are water, and the translucent green molecules are the hematite crystal.**

From the figure it is possible to see that the interface has a rough wave-like structure. In this snapshot, the $CO_2$ molecules (red) dominate the top half of the interface in Figure 10.13, while the center of the interface is dominated by water (blue). This behavior was typical for all systems, with continuous fluctuations in the interface, as $CO_2$ molecules attempted to enter the Water 1 cell. Another effect that was visible during the simulations was the repulsive push of the adsorbed water on the hematite surface. This effect could be observed on the interface,

as the $CO_2$ molecules were repelled near hematite, but were able to push further into the Water 1 cell by moving around hematite.

### 10.5.3 Solubility of water

During the simulations, water molecules were observed to enter the $CO_2$ cell. These molecules did rarely stay within the $CO_2$ for very long, as they most often returned to the water cell they had originated from. This is in good accordance with the real behavior of water, as the diffusion of water into $CO_2$ is poor. There were a few exceptions to this behavior, as a small number of water molecules were observed to cross the $CO_2$ cell and enter the other water cell. These water molecules were observed to cross the $CO_2$ in both directions, resulting in a small amount of Water 1 molecules in the Water 2 cell and vice versa. The number of these "foreign" water molecules in each phase was about the same, and because the mass transport was minimal, these phases were in equilibrium. This was true for all the different systems.

### 10.5.4 Diffusion of $CO_2$ into the Water 1 cell:

The diffusion of $CO_2$ into Water 1 has previously been discussed in both section 10.3.2 and section 10.4.4. The number of $CO_2$ molecules in the water bulk phase was counted in each system. The conditions chosen for counting the number of $CO_2$ in bulk were set to be 5 Å from both the Water/$CO_2$ interface and the hydrate crystal. These conditions were included to minimize the influence by both temporary interface fluctuations and pull from the hematite crystal. Five samples were taken for each system, from different times in the simulation run. The results revealed that the F3C system had the highest average, with 22 $CO_2$ molecules in the Water 1 cell, while both TIP4P and SPC/E had an average of 13 $CO_2$ molecules each. As the F3C system was the system that had been simulated for the shortest time, these numbers indicate that the F3C model has the fastest rate of diffusion of $CO_2$ into water. The numbers also indicate that the diffusion ratio was lower for this simulation study than in the studies conducted by (da Rocha et al. 2001). This was not the case in the small reference system, which would indicate that the inclusion of the hematite crystal leads to a lower amount of $CO_2$ diffused within the Water 1 phase. This might be true, as $CO_2$ is kept away from the hematite crystal by the adsorbed water on the crystal surface.

### 10.5.5 Mobility properties of water and $CO_2$

Both the free $CO_2$ and the free water molecules were observed to have a high mobility during the simulations. For example, a single $CO_2$ molecule could start a simulation run within one of the half open hydrate cavities, and end up at the Water 1/free $CO_2$ interface at the end of the simulation run. It is however important to point out that the $CO_2$ within the cavities were quite stable during the simulations. Only occasionally did a $CO_2$ molecule leave the cavities, and could then move rapidly to another part of the system. The other exception for this mobility was the $CO_2$ molecules diffused deep into (more than 5 Å) the Water 1 cell. These molecules moved slowly within the cell, until they came close to the hematite crystal or the Water 1/hydrate interface.

Similar mobility properties could be seen within the water cells. As mentioned in section 10.5.3, a small number of water molecules were capable of moving between the different water cells by crossing the $CO_2$ gas phase. The adsorbed water molecules on the surface of the hematite crystal were also observed to be mobile. Although an adsorbed water layer was kept around the hematite crystal through the simulations, not all of the water molecules remained in this layer. Some of them were observed to leave the layer and entered the bulk phase. These molecules were naturally replaced by other water molecules, which meant that the adsorbed layer was formed by different water molecules through the simulations.

## 10.6 Discussion of the water model effects on the system

The different simulations of the system gave very similar results in spite of using three different water models. The greatest differences from using three water models did not lie in the behavior of the system, but more in the numbers behind this behavior. The F3C model appeared to yield the best results for $CO_2$ structure, as it had the best diffusion rate of $CO_2$ into Water 1, as well as many $CO_2$ molecules structured on both sides of the hematite crystal. Its structure with other water molecules were less satisfactory, something that was shown by the low number of water molecules near hematite and the loss of $CO_2$ molecules from the hydrate cavities. The RDF curves for water might indicate that this was because of poor O-O structure in water. This was perhaps because the F3C model is less suited for simulation when kept

rigid, as it is normally flexible. The TIP4P model yielded good overall results for the structuring of $CO_2$. It also gave some good results on the behavior of water, but had a poor number of hydrogen bonds to the hematite crystal. The SPC/E model was not the best model for including $CO_2$ as guests in hydrate, but had good results elsewhere, especially for water near hematite. Investigations of the pair correlation functions revealed that SPC/E has a deviating curve in the oxygen – hydrogen structure when compared to the other RDF curves. This did not seem to visually affect the water molecules in the system, as the behavior of free water was good.

From this it is possible to deduct that each of these models had their weaknesses and strengths in our MD simulation, but were all able to simulate the system's behavior.

## 10.7 Discussion of system results and limitations

The simulations of this system have provided much valuable information. The most valuable observations have been the adsorption of water on the hematite crystal, as well as the structuring of $CO_2$ molecules within the half-open cavities of hydrate. The results also indicate that free $CO_2$ will attempt to form new cavities on a completed hydrate surface structure as well, as it was observed in the simulations. This is something that has to be explored further in order to be completely verified. The water surrounding hydrate does also appear to become a part of hydrate, as both the visual investigations of the hydrogen bond structure in VMD and the density profile indicate that most of the Water 2 phase was oriented as to extend the hydrate crystal.

This system did have some limitations when it came to reproducing the true long time behavior of the real-life system. The original system setup with hematite crystal position positioned inside the water bulk emulated a situation that would be commonly encountered during the transport of carbon dioxide mixture in water-wet rusty pipes. We found that in this case, a tight water layer immediately formed around the hematite crystal, with the adsorbed water keeping the $CO_2$ molecules away from the hematite surface and making any structural correlations between hematite and $CO_2$ improbable. One might hypothesize that this water layer will remain impervious to effects of individual $CO_2$ molecules. On the other hand, experimental time scale may give rise to rare but possible collective effects when two, three

or even four $CO_2$ molecules will attempt to reach the hematite surface **at the same time**. Those collective phenomena may have a much higher degree of success than single molecules. A possible way to get around the long simulation time needed for such events to occur would be to originally position the hematite crystal inside the $CO_2$ phase. This particular setup might also be relevant in cases when the sheer forces in the pipeline succeed in tearing the water layer away from the walls and exposing rust directly to carbon dioxide.

Another system limitation was the thick layer of $CO_2$ in the center of the system. Combined with the very low solubility of water in carbon dioxide, this thickness made it impossible to determine whether additional water from the Water 1 phase could cross over to aid further hydrate growth. In order to identify such hydrate growth in this system, we have to run the system for a very long time (upwards of 100 nanosecond simulation). A suggestion for further work could therefore be to create a different system for investigating these properties further.

# 11 Conclusions

Simulation and analysis results discussed in chapter 10 have enabled us to draw some conclusions, with the most important one being that our simulations managed to reproduce a number of the system properties with great success.

The water-wettening nature of hematite was observed early in the simulation, as water adsorbed on the hematite surface in two highly structured layers. The structure was achieved by means of water hydrogens orienting towards the hematite oxygens. If this phenomenon holds true in the case of the real-life carbon dioxide pipe transport, this would indicate that the use of dew point curves to determine water-drop out is an outdated method, as the water would condense on the hematite surface before it condenses within the $CO_2$ gas phase. In order to prove this, the chemical potential of water adsorbed on hematite must be calculated. As this is important knowledge for the industry, investigating the chemical potential could be an excellent suggestion for further work.

The adsorbed layer prevented the $CO_2$ molecules from approaching the hematite surface. Within the simulation time it was not possible to observe any structural correlation between hematite and $CO_2$ within the simulated time in this work. This indicates that individual $CO_2$ molecules may not be able to approach a wet hematite surface and adsorb. With the limitations of simulation length of this work, it was not possible to determine the possible collective effects and long term impacts for CO2 adsorption and/or large CO2 concentrations near hematite. It might therefore be useful in further work to investigate this possibility further by making a system where the hematite crystal starts in the $CO_2$ cell. If the crystal starts dry in contact with $CO_2$ from the beginning, the chances of structure correlation should be higher.

Another interesting effect of including the hematite crystal was the accelerated diffusion of $CO_2$ into the Water 1 cell. Even though the adsorbed layer around hematite repelled the $CO_2$ molecules that came close to hematite, it seems that the diffusion rate of $CO_2$ into Water 1 was increased by the presence of hematite. On the other hand, it appears that including the hematite crystal in the Water 1 phase also results in a lower diffusion ratio, as the total number of $CO_2$ diffused within water is lower than expected. The reference system containing only water and $CO_2$ did not have this problem, so it might suggest that the repulsive forces from the adsorbed water surrounding hematite has some part to play here.

The orientation of the hematite crystal surface towards the hydrate or $CO_2$ phase gave no clear result, as the crystal continued to translate and rotate through the simulations. Although observations showed that the crystal approached both of the phases in the simulations, no permanent orientation could be identified.

The results obtained for the hydrate crystal were also promising. The surrounding water around the partially open hydrate cavities quickly acted to complete the cavity structure. The free $CO_2$ molecules entered the cavities as the simulation progressed, and behaved as guest molecules for the rest of the simulation, even though a few of them escaped back into the free $CO_2$ phase. A surprising effect was that $CO_2$ molecules approached hydrate from the opposite side as well, and assumed positions on the surface that indicated an expansion of the hydrate structure. These results indicate a possibility of real-life hydrate growth in a pipeline and show that the faraway presence of hematite would not substantially hinder hydrate growth.

The behavior of the system through the simulations indicates that the force field models chosen were suitable. The three water models used all yielded the same system behavior, with minor differences. As none of the models proved to be superior on a whole-system basis, it becomes hard to nominate a clear candidate for further simulations of similar systems. Further testing of water models in relevant systems could therefore be interesting to investigate.

# 12 Suggestions for further work

This section contains some suggestions for further research based on this work. These suggestions have been sorted in groups based on whether they include research on the existing system, or if they involve creating new systems.

## 12.1 Research based upon the existing simulation system

### 12.1.1 Estimation of the excess chemical potential

A suggestion for further research on the existing system could be to use the already generated trajectory files to estimate the excess chemical potential of water adsorbed on the hematite crystal and the hydrate crystal. It can be estimated by methods described in this work. The estimates could then be used to answer a number of questions, such as:

- What do these values say about the water's affinity to drop out on hematite and the hydrate growth?
- How do they compare to the results of Haynes (2009) and Vassdal (2010)?
- Are there large differences in the chemical potential calculated for three different water models?
- What do the values say about system equilibrium or preference for phase transition?

Answering these questions could give further insight in how these processes work in MD simulation.

### 12.1.2 Non-transferable water models in the system

Another suggestion for further research would be to use other water models in order to find the water model deemed most suitable for the system. A valid choice could be to test non-transferable models that combine, for example, Lennard-Jones and Buckingham interactions with the hematite parameters found in de Leeuw and Cooper (2007). Polarizable models could be interesting to investigate in this case, as well as flexible models that successfully replicate the freezing point of water. Once the properties of the models have been found satisfactory, the existing trajectory files can be used in order to start the simulation of these models from a stable system configuration.

## 12.2 Research based on creating new simulation systems

### 12.2.1 System with hydrate, $CO_2$ and water

A new, large system focusing on $CO_2$ adsorption on hydrate surfaces could be interesting to investigate. The system would be similar to the system used in this work, but with no hematite crystal present, as well as two large cells for free water and free $CO_2$, to ensure good bulk phase structure in the system. Another change interesting to include would be to build the hydrate with closed cavities, and observe the $CO_2$ and water structure on the outside. What does this structure say about hydrate growth?

### 12.2.2 System with O-termined hematite crystal

Because no structure could be observed between hematite and $CO_2$, it could be interesting to build a similar system with water, $CO_2$ and hydrate, but with a different hematite crystal. A suggestion for this could be to create a hematite crystal with a hydrated oxygen-terminated surface, as discussed in (de Leeuw and Cooper 2007) and (Trainor et al. 2004). Run an MD-simulation of the new system and investigate the behavior of the hematite crystal after its hydration. Will there be a permanent crystal orientation towards either the $CO_2$ phase or hydrate? How are the structural effects between hematite and hydrate in this system?

### 12.2.3 Monte Carlo simulations to investigate hydrate stability

Another suggestion focuses on determining the stability of hydrate. Create a system containing SPC/E water, $CO_2$ and hydrate. The hydrate should have a fully formed lattice structure and should also be lacking a few $CO_2$ guest molecules near the surface of the hydrate crystal. The water molecules that form the hydrate should only be allowed to rotate, not translate, to ensure stability of the hydrate crystal through the simulations. Run an MD simulation to observe if any of the $CO_2$ molecules are capable of entering the empty crystal, or if the presence of the free $CO_2$ gas phase is able to pull more $CO_2$ out of the hydrate crystal. How do the empty hydrate cavities affect the structure between hydrate and water, as well as hydrate and $CO_2$?

A possible additional study of the system could be to simulate it using the Monte Carlo method. (Kvamme et al. 1993) has developed an MC code that should be suitable for these simulations. What differences do these simulations yield for the structure, and what does this imply for the free energy?

### 12.2.4 Two simple systems containing hematite, $CO_2$ and water

In order to investigate the structure effects near hematite over longer simulation times, two simple systems containing a hematite crystal, $CO_2$ phase and water phase could be created. One of the systems has the hematite initially placed within the water phase, while the other has it placed in the $CO_2$ phase. Investigate how the crystal moves in either phase. What are the structural differences in these systems? Can a hematite - $CO_2$ structure be identified?

### 12.2.5 Two longer simulations with two simple systems

Another suggestion is to investigate the long run effects of hematite adsorption structure on a longer time scale. Two simple systems must be built for this, one with only water and hematite, and another with only $CO_2$ and hematite. Simulate these systems for about 100 nanoseconds. How does hematite want to orient itself in the $CO_2$ system without the competition from water? What is the difference in excess chemical potential for the adsorbed structure in these two systems? Note that the systems must be kept simple in order to simulate them for such a long time scale.

# References


Allen, M. P. and Tildesley, D. J. (1987). Computer Simulation of Liquids. New York, Oxford University Press Inc.: 1-180.

Astarita, G. (1989). Thermodynamics - An Advanced Textbook for Chemical Engineers. New York, Plenum Press: 108-109.

Berendsen, H. J. C., Grigera, J. R. and Straatsma, T. P. (1987). "The Missing Term in Effective Pair Potentials." Journal of Physical Chemistry **91**(24): 6269-6271.

Berendsen, H. J. C., Postma, J. P. M., van Gunsteren, W. F. and Hermans, J. (1981). Interaction models for water in relation to protein hydration. Intermolecular forces. Pullman, B. Dordrecht, The Netherlands, D. Riedel Publishing Company**:** 331-342.

Blake, R. L., Hessevick, R. E., Zoltai, T. and Finger, L. W. (1966). "Refinement of the hematite structure." The American Mineralogist **51**: 123-129.

Bolstad, S. (2009). "Kalkulatoren som varsler sommerværet." Retrieved 13.04.11, from <http://www.forskning.no/artikler/2009/august/226418>.

Brooks, B. R., Brooks, C. L., Mackerell, A. D., Nilsson, L., Petrella, R. J., Roux, B., Won, Y., Archontis, G., Bartels, C., Boresch, S., Caflisch, A., Caves, L., Cui, Q., Dinner, A. R., Feig, M., Fischer, S., Gao, J., Hodoscek, M., Im, W., Kuczera, K., Lazaridis, T., Ma, J., Ovchinnikov, V., Paci, E., Pastor, R. W., Post, C. B., Pu, J. Z., Schaefer, M., Tidor, B., Venable, R. M., Woodcock, H. L., Wu, X., Yang, W., York, D. M. and Karplus, M. (2009). "CHARMM: The Biomolecular Simulation Program." Journal of Computational Chemistry **30**(10): 1545-1614.

Cao, Z. T., Tester, J. W. and Trout, B. L. (2001). "Computation of the methane-water potential energy hypersurface via ab initio methods." Journal of Chemical Physics **115**(6): 2550-2559.

Catti, M., Ferraris, G., Hull, S. and Pavese, A. (1995). "Static Compression and H-Disorder in Brucite, Mg(Oh)(2), to 11 Gpa - a Powder Neutron-Diffraction Study." Physics and Chemistry of Minerals **22**(3): 200-206.

Çengel, Y. A. and Boles, M. A. (2007). Thermodynamics - An engineering approach. New York, McGraw-Hill: 741-742.

Christensen, A. N., Lehmann, M. S. and Convert, P. (1982). "Deuteration of Crystalline Hydroxides - Hydrogen-Bonds of Gamma-Aloo(H,D) and Gamma-Feoo(H,D)." Acta Chemica Scandinavica Series a-Physical and Inorganic Chemistry **36**(4): 303-308.

Cygan, R. T., Liang, J. J. and Kalinichev, A. G. (2004). "Molecular models of hydroxide, oxyhydroxide, and clay phases and the development of a general force field." Journal of Physical Chemistry B **108**(4): 1255-1266.

da Rocha, S. R. P., Johnston, K. P., Westacott, R. E. and Rossky, P. J. (2001). "Molecular structure of the water-supercritical CO2 interface." Journal of Physical Chemistry B **105**(48): 12092-12104.

de Leeuw, N. H. and Cooper, T. G. (2007). "Surface simulation studies of the hydration of white rust Fe(OH)(2), goethite alpha-FeO(OH) and hematite alpha-Fe2O3." Geochimica Et Cosmochimica Acta **71**(7): 1655-1673.

DNV (Det Norske Veritas) (2010). "Recommended Practice DNV-RP-J202." Retrieved 31.05.11, from http://exchange.dnv.com/publishing/Codes/download.asp?url=2010-04/rp-j202.pdf.

Drexler, K. E. (1992). Nanosystems: Molecular Machinery, Manufacturing, and Computation. New York, John Wiley & Sons. Retrieved 16.03.11, from http://e-drexler.com/d/06/00/Nanosystems/glossary/glossary_s.html.

Frenkel, D. and Smit, B. (2002). Understanding Molecular Simulation - From Algorithms to Applications. San Diego, Academic Press: 9-17, 23, 63-105, 167-199, 525-529.

Gao, G. T., Zeng, X. C. and Tanaka, H. (2000). "The melting temperature of proton-disordered hexagonal ice: A computer simulation of 4-site transferable intermolecular potential model of water." Journal of Chemical Physics **112**(19): 8534-8538.

Gundersen, A. (2005). "Targeting Pipeline Management." Retrieved 08.03.11, from http://www.dnv.in/services/software/publications/2005/no_3/TargetingPipelineManagement.asp.

Harris, J. G. and Yung, K. H. (1995). "CARBON DIOXIDES LIQUID-VAPOR COEXISTENCE CURVE AND CRITICAL PROPERTIES AS PREDICTED BY A SIMPLE MOLECULAR-MODEL." Journal of Physical Chemistry **99**(31): 12021-12024.

Haynes, M. (2009). "Vannutfelling på rustoverflater i rør." Institutt for fysikk og teknologi. Master thesis, Universitetet i Bergen.

Hellan, Ø. (2007). "Strømmen gjennom dypet." Retrieved 08.03.11, from http://www.ntnu.no/gemini/2007-02/20-23.htm.

Hill, R. J. (1979). "Crystal-Structure Refinement and Electron-Density Distribution in Diaspore." Physics and Chemistry of Minerals **5**(2): 179-200.

Hoover, W. G. (1985). "Canonical dynamics: Equilibrium phase-space distributions." Physical Review A **31**(3): 1695.

Humphrey, W., Dalke, A. and Schulten, K. (1996). "VMD: Visual molecular dynamics." Journal of Molecular Graphics **14**(1): 33-38.

Jedlovszky, P. and Mezei, M. (2000). "Calculation of the free energy profile of H2O, O-2, CO, CO2, NO, and CHCl3 in a lipid bilayer with a cavity insertion variant of the Widom method." Journal of the American Chemical Society **122**(21): 5125-5131.

Jones, F., Rohl, A. L., Farrow, J. B. and van Bronswijk, W. (2000). "Molecular modeling of water adsorption on hematite." Physical Chemistry Chemical Physics **2**(14): 3209-3216.

Jorgensen, W. L. (1981). "Quantum and Statistical Mechanical Studies of Liquids .10. Transferable Intermolecular Potential Functions for Water, Alcohols, and Ethers - Application to Liquid Water." Journal of the American Chemical Society **103**(2): 335-340.

Jorgensen, W. L. (1982). "Revised TIPS for simulations of liquid water and aqueous solutions." Journal of Chemical Physics **77**(7): 4156-4163.

Jorgensen, W. L., Chandrasekhar, J., Madura, J. D., Impey, R. W. and Klein, M. L. (1983). "Comparison of Simple Potential Functions for Simulating Liquid Water." Journal of Chemical Physics **79**(2): 926-935.

Kuznetsova, T. (2001). Molecular modeling for thermodynamic properties of bulk and interfacial systems. Bergen, University of Bergen - Department of Physics: 7-9.

Kvamme, B. (2011). Hydrate phase transitions kinetics and kinetic inhibition. Total. Paris, France.

Kvamme, B. (2011). Multiscale challenges in hydrate exploitations. PETRAD-CCOP-PETROVIETNAM-VASI Workshop on gas hydrates. Halong Bay, Vietnam.

Kvamme, B., Kuznetsova, T. and Morrissey, K. (2009). An alternative for carbon dioxide emission mitigation: *in situ* methane hydrate conversion. ICCMSE (International Conference of Computational Methods in Sciences and Engineering), Rhodes, Greece, University of Bergen, Department of Physics and Technology.

Kvamme, B., Kuznetsova, T. and Uppstad, D. (2009). "Modeling excess surface energy in dry and wetted calcite systems." Journal of Mathematical Chemistry **46**: 756-762.

Kvamme, B., Lund, A. and Hertzberg, T. (1993). "The Influence of Gas Gas Interactions on the Langmuir Constants for Some Natural-Gas Hydrates." Fluid Phase Equilibria **90**(1): 15-44.

Kårstad, O. (2006). "CO2 Capture and Storage Project Details." Retrieved 08.03.11, from http://www.co2captureandstorage.info/project_specific.php?project_id=163.

Lado-Tourino, I. and Tsobnang, F. (2000). "Using computational approaches to model hematite surfaces." Computational Materials Science **17**(2-4): 243-248.

Laider, K. J., Meiser, J. H. and Sanctuary, B. C. (2003). Physical Chemistry. Boston, Houghton Mifflin Company: 931-933.

Lervik, J. K. and Kulbotten, H. (2011). "Verdifull kur mot kalde plugger - SINTEF." Retrieved 11.03.11, from http://www.sintef.no/SINTEF-Energi-AS/Xergi/Xergi-2010/Nr-1---juni/Verdifull-kur-mot-kalde-plugger/.

Levitt, M., Hirshberg, M., Sharon, R., Laidig, K. and Daggett, V. (1997). "Calibration and Testing of a Water Model for Simulation of the Molecular Dynamics of Proteins and Nucleic Acids in Solution." Journal of Physical Chemistry B **101**(25): 5051-5061.

Lyubartsev, A. P. and Laaksonen, A. (2000). "MDynamix - A scalable portable parallel MD simulation package for arbitrary molecular mixtures." Computer Physics Communications **128**: 565-589.

Mahoney, M. W. and Jorgensen, W. L. (2000). "A five-site model for liquid water and the reproduction of the density anomaly by rigid, nonpolarizable potential functions." Journal of Chemical Physics **112**(20): 8910-8922.

Mathworks (2011). "MATLAB, The Language Of Technical Computing." Retrieved 26.05.11, from http://www.mathworks.com/products/matlab/.

McCabe, W. L., Smith, J. C. and Harriott, P. (2005). Unit operations of chemical engineering. New York, McGraw-Hill: 524-525.

McCormick, J. M. (2011). "Molecular Modeling 1: Classical Molecular Modeling." Retrieved 09.03.11, from http://chemlab.truman.edu/CHEM131Labs/MolecularModeling1.asp.

McQuarrie, D. A. (2000). Statistical Mechanics. Sausalito (California), University Science Books: 257-260.

Metropolis, N., Rosenbluth, A. W., Rosenbluth, M. N., Teller, A. H. and Teller, E. (1953). "Equation of State Calculations by Fast Computing Machines." Journal of Chemical Physics **21**(6): 1087-1092.

Moshfeghian, M. (2011). "What is the Impact of Water Content on the Dew Point and Hydrate Phase Behavior." Retrieved 09.03.11, from http://www.jmcampbell.com/january-2011.php.

Natarajan, V., Bishnoi, P. R. and Kalogerakis, N. (1994). "Induction Phenomena in Gas Hydrate Nucleation." Chemical Engineering Science **49**(13): 2075-2087.

Oosterkamp, A. (2008). "CO2 PIPELINE TRANSMISSION -a broad state of the art-." Retrieved 08.03.11, from http://www.climit.no/frontend/files/CONTENT/CLIMIT/porsgrunn_polytec.pdf.

Palmer, D. C. and Palmer, S. E. (2011). "What is CrystalMaker®?" Retrieved 14.04.11, from http://www.crystalmaker.com/crystalmaker/whatis.html.

Prausnitz, J. M., Lichtenthaler, R. N. and de Azevedo, E. G. (1999). Molecular Thermodynamics of Fluid-Phase Equilibria. Upper Saddle River, New Jersey, Prentice Hall Inc.: 847.

Rustad, J. R., Wasserman, E. and Felmy, A. R. (1999). "Molecular modeling of the surface charging of hematite - II. Optimal proton distribution and simulation of surface charge versus pH relationships." Surface Science **424**(1): 28-35.

Shilnikov, V. I. and Shnulin, A. N. (1992). "Some Formal Aspects of Using the Atom-Atom Potential Model in Energy Calculations." Journal of Structural Chemistry **33**(2): 242-247.

Shpakov, V. P., Tse, J. S., Tulk, C. A., Kvamme, B. and Belosludov, V. R. (1998). "Elastic moduli calculation and instability in structure I methane clathrate hydrate." Chemical Physics Letters **282**(2): 107-114.

Sloan, E. D. (1990). Clathrate hydrates of natural gases. New York, Marcel Dekker, Inc.: 24-66.

Stillinger, F. H. and Rahman, A. (1974). "Improved simulation of liquid water by molecular dynamics." Journal of Chemical Physics **60**(4): 1545-1557.

Svandal, A., Kuznetsova, T. and Kvamme, B. (2006). "Thermodynamic properties and phase transtions in the H2O/CO2/CH4 system." Physical Chemistry Chemical Physics **8**(14): 1707-1713.

Tegze, G., Pusztai, T., Toth, G., Granasy, L., Svandal, A., Buanes, T., Kuznetsova, T. and Kvamme, B. (2006). "Multiscale approach to $CO_2$ hydrate formation in aqueous solution: Phase field theory and molecular dynamics. Nucleation and growth." The Journal of chemical physics **124**(234710): 1-12.

Tohidi, B. (Heriot Watt University - Institute of Petroleum Engineering) (2011). "What are gas hydrates?" Retrieved 19.04.11, from http://www.pet.hw.ac.uk/research/hydrate/hydrates_what.cfm?hy=what.

Trainor, T. P., Chaka, A. M., Eng, P. J., Newville, M., Waychunas, G. A., Catalano, J. G. and Brown, G. E. (2004). "Structure and reactivity of the hydrated hematite (0001) surface." Surface Science **573**(2): 204-224.

Tsuzuki, S., Uchimaru, T., Tanabe, K., Kuwajima, S., Tajima, N. and Hirano, T. (1996). "Refinement of nonbonding interaction parameters for carbon dioxide on the basis of the pair potentials obtained by MP2/6-311+G(2df)-level ab initio molecular orbital calculations." Journal of Physical Chemistry **100**(11): 4400-4407.

Vassdal, J. T. (2010). "Molekylærdynamiske studier av vannadsorpsjon på hematitt." Institutt for fysikk og teknologi. Master thesis, University of Bergen, June 2010.

Vlot, M. J., Huinink, J. and Eerden, J. P. v. d. (1998). "Free energy calculations on systems of rigid molecules: An application to the TIP4P model of H2O." Journal of Chemical Physics **110**(1): 55-61.

Vorholz, J., Harismiadis, V. I., Rumpf, B., Panagiotopoulos, A. Z. and Maurer, G. (2000). "Vapor + liquid equilibrium of water, carbon dioxide, and the binary system, water + carbon dioxide, from molecular simulation." Fluid Phase Equilibria **170**: 203-234.

Wasserman, E., Rustad, J. R. and Felmy, A. R. (1999). "Molecular modeling of the surface charging of hematite - I. The calculation of proton affinities and acidities on a surface." Surface Science **424**(1): 19-27.

Weiner, P. K. and Kollman, P. A. (1981). "Amber - Assisted Model-Building with Energy Refinement - a General Program for Modeling Molecules and Their Interactions." Journal of Computational Chemistry **2**(3): 287-303.

Wu, Y., Tepper, H. L. and Voth, G. A. (2006). "Flexible simple point-charge water model with improved liquid-state properties." Journal of Chemical Physics **124**(024503): 1-12.

# Appendix A: Additional water models

This section lists the other water models that were considered for this work. These water models were considered to be less suitable for the simulations, and were therefore included in the appendix for comparative reasons.

## BF

The Bernal-Fowler is a four point charge model developed by Bernal and Fowler. This water model has a bond length $r_{OH}$ equal to 0.96 Å, while the HOH angle is 105.7°. The charges in hydrogen are $+0.49e$ each. The model does not include any charges centered on the oxygen atom. Instead, this charge is moved to a partial charge M, which is found at a distance $r_{OM}$ of 0.15 Å, closer to the hydrogen atoms. The charge on M is equal to $-0.98e$ (Jorgensen et al. 1983).

Jorgensen et al. (1983) compared the BF water model to other water models, and concluded that BF was the only water model that was unreasonable when compared with experimental results, as it significantly overestimated the density by 18% and had poor structural qualities. Furthermore, Jorgensen considered the BF model to be outdated, which is justifiable, considering that it was published in 1933 (Jorgensen et al. 1983).

## ST2

The ST2 potential model was proposed by Stillinger and Rahman (1974). This model is a 5-site potential model, with charges on the hydrogens and on two lone pair positions oriented tetrahedrally around the oxygen. See Figure A.1 from Stillinger below:

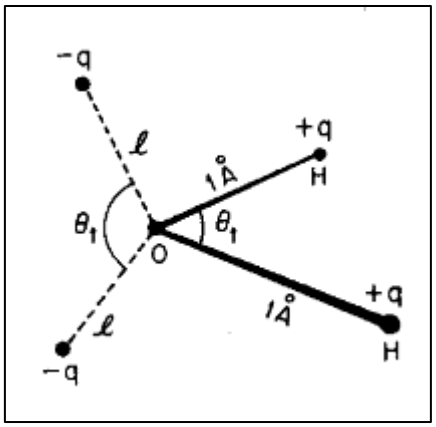


**Figure A.1 – ST2 water molecule from**
**(Stillinger and Rahman 1974)**

In this figure, *l* is equal to 0.8 Å, while the HOH angle is equal to 109.47˚. The charges on the hydrogen are $+0.2357e$, while the charges oriented tetrahedrally around the oxygen are $-0.2357e$. The tetrahedral angle is the same as the HOH angle, namely 109.47˚ (Stillinger and Rahman 1974).

Jorgensen et al. (1983) describes this model as an accurate model for the simulation of liquid water. Unfortunately it is also very complex, because it requires 17 distances to evaluate the potential function. As a result of this, the total computer time used is about 35% more than a model with 3 or 4 sites (Jorgensen et al. 1983).

## TIPS2

The Transferable Intermolecular Potential functionS (TIPS) are a set of models developed for simulating organic liquids and water. The TIPS2 model is an improved version of the original water model from the TIPS. The TIPS2 model is described as a simple four-site model with a Lennard-Jones term acting between the oxygen atoms. The model also employs Coulomb to represent the intermolecular forces between charged sites. The charge values located on the hydrogen atoms $q_H$ are +0.535*e* each, while the $r_{OH}$ distance is equal to +0.9572 Å. The Hydrogen-Oxygen-Hydrogen angle is equal to 104.52˚. Since it is a four-site model, there is a partial charge included at $r_{OM}$ 0.15 Å from the oxygen atom, located closer to the hydrogen atoms. This charge $q_M$ is equal to -1,07*e*.

The TIPS2 water model has been compared with models such as SPC, ST2 and TIPS, as well as experimental data. Based on this, Jorgensen states that the TIPS2 water model is one of the more accurate models, rivaled only by TIP4P. This is because the RDF curve for O-O interactions is very accurate for TIPS2, which is not the case with the three-point models. Although the three-point models tested had a better description of the hydrogen structure, the experimental results for the O-H and H-H structure are more uncertain. In addition to this, the poor structure of O-O for these models makes them less suitable than models such as TIPS2 and TIP4P (Jorgensen 1982).

## TIP3P

The 3-Point Transferable Intermolecular Potential (TIP3P) model is a three-point charge water model. The TIP3P model has the charges centered on the atoms. The hydrogen charges are $+0.417e$, while the oxygen charge is $-0.834e$. The bond length $r_{\mathrm{OH}}$ is equal to 0.9527 Å, while the bond angle HOH is $104.52^{\circ}$. In addition to this, the oxygen atom has a Lennard-Jones term, which describes the intermolecular forces acting between the oxygen atoms (Wu et al. 2006).

Jorgensen et al. (1983) has compared the TIP3P model with other models. The benefit of using TIP3P was that the model gave good results for the hydrogen-oxygen and hydrogen-hydrogen RDFs, especially when compared to the 4-point models. Unfortunately, the oxygen-oxygen RDF is not as good. The first peak was reproduced, but the second peak is not visible in TIP3P, or in the other 3-point models tested here. Levitt et al. (1997) informs that the unsatisfactory structure for the O-O interactions lead to the development of the TIP4P model, which was created from the TIP3P model with a partial charge, in order to improve the O-O structure (Jorgensen et al. 1983), (Levitt et al. 1997).

## TIP5P

The 5-point Transferable Intermolecular Potential (TIP5P) model is a rigid 5-point charge model proposed by Mahoney and Jorgensen (2000). The model is similar to the ST2 model, as it has charges placed on both of the hydrogen, as well as two partial charges oriented around the oxygen. The model can best be described by considering Figure A.2 from Mahoney below:

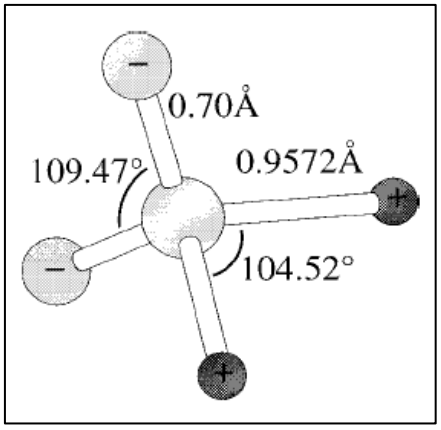


**Figure A.2 - TIP5P water molecule from (Mahoney and Jorgensen 2000)**

The figure depicts the structure of the TIP5P water molecule. The figure shows that the bond length $r_{OH}$ is equal to 0.9572 Å, while the partial charge bond length $r_{OL}$ is equal to 0.70 Å. The HOH angle is 104.52˚, while the partial charge angle is the tetrahedral angle, namely 109.47˚. As for the charges, the charge on the hydrogen atoms is equal to $+0.241e$, while the partial charges are equal to $-0.241e$ each. As with the other TIP-models, the TIP5P uses Lennard-Jones to describe short-range interactions, while Coulomb is used to manage the long-range interactions. The Lennard-Jones term is placed on the oxygen atom.

The TIP5P model is described as a very accurate model for obtaining the correct system density *ρ(T)* for a simulation. However, as a 5-point model, it requires more simulation time to do so. As stated by Mahoney, it is unlikely that simulations of a length less than ~1 nanoseconds are capable of producing accurate results (Mahoney and Jorgensen 2000).

# Appendix B: A selection of RDF curves from the simulation

A great number of RDF curves were obtained from all systems during this work. Unfortunately, it was impossible to include them all, as this work would be impractically long. This section includes some of the more interesting RDF curves with a short description.

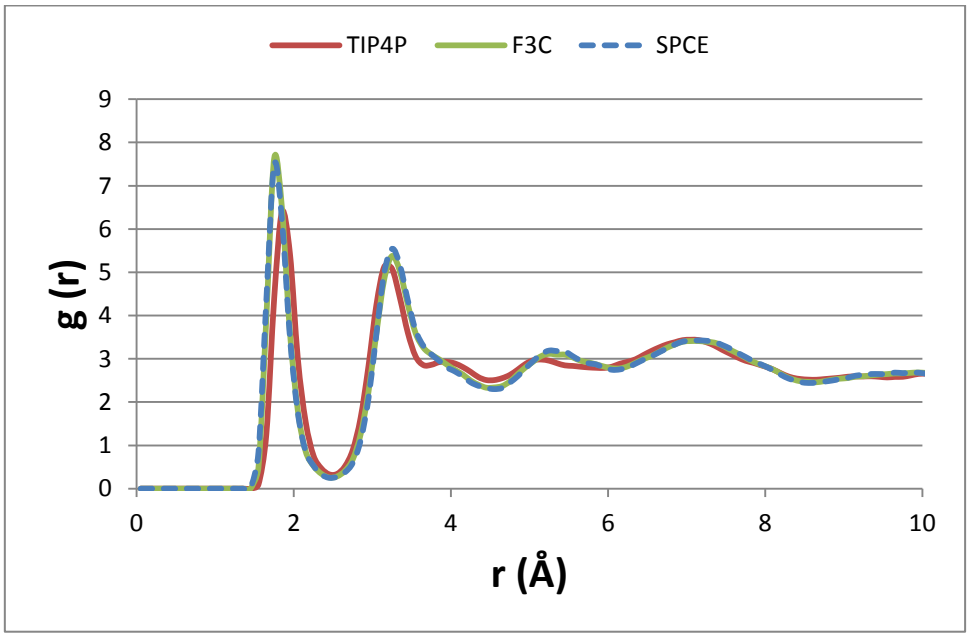


**Figure B.1 - System comparison of the hydratewater oxygen – hydrogen RDF curves**

Figure B.1 shows the hydrate oxygen – hydrogen structure for all three simulation systems. Although the hydrate molecules were prevented from translated in the simulations, they were allowed to rotate. The figure illustrates that the SPC/E and F3C systems are identical, while the TIP4P system structure is different. There is a very simple explanation for this; as the TIP4P model is a 4-point model with a partial charge, the rotation of this system will be different from the two 3-point models. Again, the identical structure of SPC/E and F3C comes from the fact that the hydrate water molecules were prevented from translating.

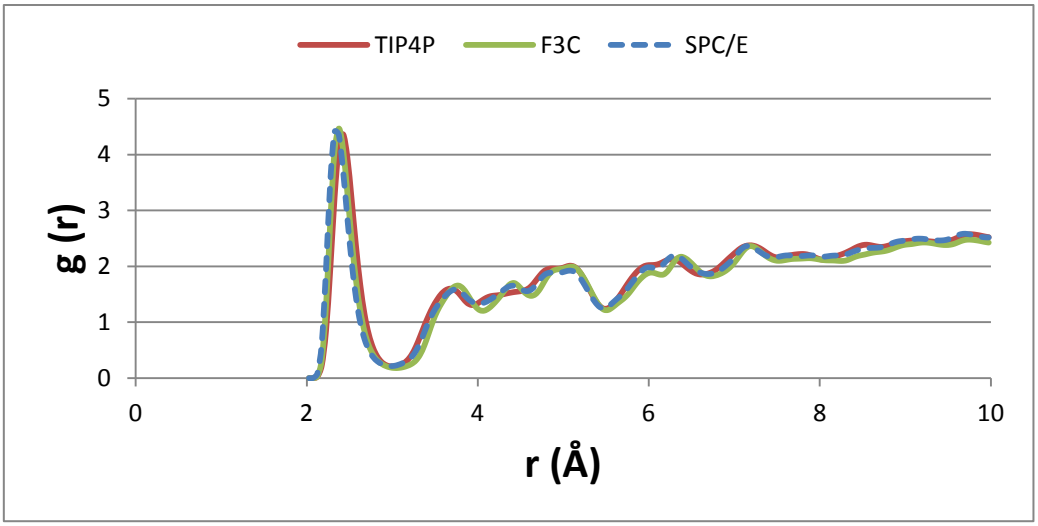


**Figure B.2 – System comparison of the hematite iron - Water 1 oxygen RDF curves.**

Figure B.2 shows the hematite iron - Water 1 oxygen structure for all systems. The most noteworthy property of this figure is that all systems have a remarkably similar structure. The largest concentration of oxygen is found around (2.325 ($\pm$0.5) Å from the iron atoms. This was to be expected, as these are oxygen found in the first adsorbed layer. The secondary adsorbed layer structure cannot be visibly identified from the figure.

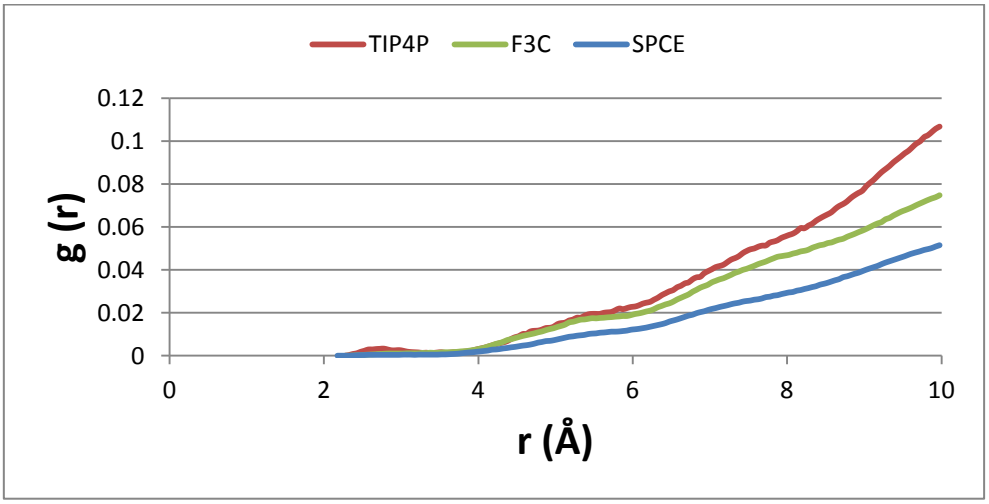


**Figure B.3 – System comparison of the hematite iron - $CO_2$ oxygen RDF curves**

Figure B.3 shows the hematite iron – $CO_2$ oxygen RDF curves for all three systems. The curves show that there is no structure that is visible from the curves. This was true for all the other curves obtained from hematite – $CO_2$, which meant that no hematite – $CO_2$ structure was visible for any of the three systems.